UNIVERSITÀ DEGLI STUDI DI NAPOLI "FEDERICO II"

Dipartimento di Ingegneria Chimica, dei Materiali

e della Produzione Industriale

Dottorato di ricerca in Ingegneria Chimica

XXVI CICLO

Drying of Porous Media.

The Case of Cotton Fabrics.

Scientific Committee

Prof. Stefano Guido

Ing. Sergio Caserta

Ing. Giovanna Tomaiuolo

Ing. Yonas Gizaw

Ing. Sergio Barbarino

Candidate

Dario Donnarumma

Anno Accademico 2013/2014

a Silvia.

Abstract

The focus of this PhD thesis is on clothes drying in home laundry, an energy-intensive operation of high societal impact due the high associated costs and carbon footprint. The main goal of this work is to improve the basic understanding of drying of cotton fabrics by combining classical thermal analysis with microscopy techniques. In particular, the proposed approach is to regard cotton fabrics as a porous medium where water can penetrate at different spatial scales. The well-known constant rate (CRP) and falling rate (FRP) phases of the drying process were related to cotton fabric porosity and our results show that drying is faster in a cotton fabric as compared to a dish filled with water with the same area of the fabric, during the CRP. Drying rate in fabrics can be enhanced by surfactants in diluted regime, in a concentration-dependent way. These effects were correlated with an increase of the interfacial area due to a decrease of the contact angle induced by the surfactant, by a single capillary model. All the drying curves overlap in the FRP, showing negligible effects of surfactants on drying rate. Both CRP and FRP can be qualitatively explained by considering the fiber as the base element of a multi-scale porous medium. Moreover, a single capillary model is proposed to study the evaporation process.

Sommario

L’ambito di questa tesi di dottorato riguarda l’essiccamento dei tessuti nell’ambito della lavanderia, un'operazione ad alto dispendio energetico ed ampio impatto sociale, a causa degli alti costi e delle emissioni di anidride carbonica. Il seguente lavoro si promette di migliorare la comprensione del processo di essiccamento dei tessuti combinando analisi termica classica con varie tecniche di microscopia. In particolare l'approccio proposto consiste nel considerare il tessuto di cotone come un mezzo poroso in cui l'acqua può penetrare a diverse scale spaziali. La fase con velocità di essiccamento costante (Constant Rate Phase, CRP) e quella con velocità di essiccamento decrescente (Falling Rate Phase, FRP) sono legate alla struttura porosa del tessuto di cotone ed i risultati ottenuti hanno mostrato che l’essiccamento, durante la CRP, è più rapido in un tessuto di cotone rispetto ad una piastra Petri piena d’acqua avente la stessa superficie del tessuto. La velocità di essiccamento nel tessuto può essere incrementata, in base alla concentrazione, utilizzando tensioattivi in regime diluito. Tali effetti sono stati correlati, effettuando esperimenti su micro-capillari, con l’aumento dell'area interfacciale dovuta ad una diminuzione dell'angolo di contatto indotta dal tensioattivo. Tutte le curve di essiccamento si sovrappongono nella FRP, mostrando che l’effetto dei tensioattivi sulla velocità di essiccamento è trascurabile. Inoltre, un modello a singolo capillare si propone di studiare il processo di evaporazione.

Résumé

L'objectif de cette PhD thèse est le séchage des vêtements dans la lessive, une opération à forte intensité énergétique et large impact social, en raison des coûts associés élevés et des émissions de dioxyde de carbone. Les travaux suivants promet d'améliorer la compréhension de base de séchage des tissus de coton en combinant l'analyse thermique classique avec des techniques de microscopie. En particulier, l'approche proposée consiste à considérer le tissu de coton comme un milieu poreux dans lequel l'eau peut pénétrer à différentes échelles spatiales. La phase ayant vitesse de séchage constante (Constant Rate Phase, CRP) et cela ayant vitesse de séchage décroissante (Falling Rate Phase, FRP) sont liées à la structure poreuse du tissu de coton, et les résultats obtenus ont montré que le séchage, au cours de la CRP, est plus rapide dans un tissu de coton par rapport à une boîte de Pétri remplie avec de l'eau ayant la même surface du tissu. La vitesse de séchage dans le tissu peut être augmentée, en fonction de la concentration, en utilisant des agents tensio-actifs dans le régime dilué. Ces effets ont été corrélés, en effectuant des expériences sur des micro-capillaires, avec l'augmentation de l'aire interfaciale en raison d'une diminution de l' angle de contact induite par l'agent tensio-actif. Toutes les courbes de séchage se chevauchent dans le FRP, montrant que l'effet d' agents tensio-actifs sur la vitesse de séchage est négligeable. En outre, un modèle seul capillaire est proposé d' étudier le processus d'évaporation.

Resumen

El alcance de esta tesis es el secado de los tejidos dentro de lavandería, una operación con un alto gasto energético y amplio impacto social, debido a los altos costos y las emisiones de dióxido de carbono. El objetivo principal de este trabajo es mejorar la comprensión básica del proceso de secado de los tejidos mediante la combinación de análisis térmico clásica con diversas técnicas de microscopía. En particular, el enfoque propuesto consiste en considerar el tejido de algodón como un medio poroso en el que el agua puede penetrar a diferentes escalas espaciales. La fase con velocidad de secado constante (Constant Rate Phase, CRP) y que con la velocidad descendente (Falling Rate Phase, FRP) están relacionados con la estructura porosa de la tela de algodón y los resultados obtenidos han demostrado que el secado, durante el CRP, es más rápido en un tejido de algodón con respecto a una placa de Petri llena de agua que tiene la misma superficie de la tela. La velocidad de secado en el tejido puede ser mejorada, dependiendo de la concentración, el uso de agentes tensioactivos en el régimen diluido. Estos efectos se correlacionaron, mediante la realización de experimentos en los micro-capilares, con el incremento en el área interfacial debido a una disminución en el ángulo de contacto inducida por el agente tensioactivo. Todas las curvas de secado se solapan en el FRP, mostrando que el efecto de los tensioactivos en la velocidad de secado es insignificante. Además, se propone un modelo único-capilar para estudiar el proceso de evaporación.

摘要

这份哲学博士学位论文焦点在衣裳烘干在洗衣店的，交付高的社会影响的能源消耗量大的操作高伴生的费用和碳脚印。

这工作的主要目标是改进对棉织物干燥基本的理解经过结合古典热分析与显微学技术。

特别是，提出的方法假设，水可能击穿棉织物个多孔媒介象一的用不同的空间标度。

众所周知恒定的率阶段(Constant Rate Phase, CRP) 和下降的率阶(Falling Rate Phase, FRP) 被连接到棉织物的孔隙率，并且我们的结果表示，烘干是快速在棉织物与盘比较充满与织品的同一表面的水，在 CRP 期间。

表面活性劑在稀釋的制度可以提高幹燥速率在織物中的濃度依賴的方式。

在一個單一的毛細管模型中觀察到同樣的效果, 和由於表面活性劑誘導介面面積增加。

ACKNOWLEDGEMENTS

"Be like the fountain that overflows, not like the cistern that merely contains."
Paulo Coelho

I'm very proud to say that my Master's Thesis and this PhD work had opened a new research line in the ChemEMS Lab that I hope will continue to carry out other results and ideas; as graphically explained by Matt Might[1], I've done my best to make a dent on the circle of human knowledge. The present work would be not possible without the help of a number of people.

First of all I feel to thank my PhD advisor, Prof. Stefano Guido, that believe in my abilities and give me the possibility to demonstrate them, together with my co-advisors Ing. Sergio Barbarino and Ing. Yonas Gizaw; each one in different way contribute to this works and guided me through all these years. A special thanks goes to Gene Pancheri that follows the first year of this PhD work, for his critical point of view and his unconventional approach to problems (sections 5.1 and 5.2 were inspired by his ideas). I would thank the rest of my PhD committee that support me trough this journey. Thanks to Ing. Giovanna Tomaiuolo for hers scientific contributes and for the human value she gave me being an example as a scientist and as a person. I like to thank also Ing. Sergio Caserta for his suggestions about science and life.

I feel gratitude for the welcome and help I've received in the Thermal Lab, in P&G Italy (Pomezia, Rome) from Ing. Vincenzo Guida, Ing. Fabio Zonfrilli, Ing. Enza Ceccobelli, Ing. Antonino Russello and Ing. Mariarosa Brundu.

I would like to thank also a greater number of people that, in different way, contribute to this four years trip and to my personal growth.

I would not be here if not for the love and support provided by my parents Carmine and Patrizia.

My gratitude goes to my friends that support me in this adventure. First of all, Ing. Valentina Preziosi, for her precious suggestions, Ing. Angelo Pommella and Ing. Luca Lanotte, for teaching me quite everything about how to survive in a lab and thanks all of them for being such good friends. Thanks to Doc. Antonio Perazzo, with which I share lots of the time spent on instruments, and Doc. Flora Ascione, with which I share instruments many times. Thanks also to Valeria, Speranza, Rosa, Roberta and Antonio, that make me feel part of the big family of the ChemEMS Lab. I need also to thank the students I've followed as co-advisor, for let me experience the big difference between to understand a concept and to explain a concept.

Finally, a big thanks goes to the person I dedicate this thesis, because besides every successful man there stands a successful woman. Almost five years ago we start to grow side by side like two trees, trough storms and sunny days. I hope we will keep growing together, one day at a time.

At the very end I would express gratitude to my highest power that always help me and guide me in every trouble, as a light that shine every day in my heart.

TABLE OF CONTENTS

1 INTRODUCTION 1

1.1 SUSTAINABILITY AND INNOVATION IN LAUNDRY 1

1.1.1 Carbon Friendly Dryers 3

1.1.2 Low-Carbon Detergents 5

1.1.3 Energy Efficient Laundry Process 6

1.2 RESEARCH OBJECTIVES 7

1.3 TEXTILE AS POROUS MEDIA 7

2 THEORETICAL BACKGROUND 11

2.1 FLOW IN POROUS MEDIA 12

2.1.1 Porous Media Structure 12

2.1.2 Wettability and Contact Angle 14

2.1.3 Capillarity Effect Inside Pores 18

2.1.3.1 Capillary Rise 19

2.1.3.2 Surface Tension vs. Contact Angle 21

2.2 DRYING PROCESS IN POROUS MEDIA 22

2.2.1 Transport Phenomena 23

2.2.1.1 Heat Transfer 27

2.3 MODELLING DRYING PROCESS IN FABRICS 29

2.3.1 Air/water transport phenomena in porous media 29

2.3.1.1 Linear Heat Transfer Modeling for CDR Period 31

2.3.1.2 Non-linear Modelling for FRD Period 35

2.3.2 Modeling Evaporation in Capillary tubes 36

2.3.2.1 Marangoni Effect 39

3 EXPERIMENTAL SECTION 42

3.1 MATERIALS 42

3.1.1 Aqueous Solution 42

3.1.1.1 Hard Water 42

3.1.1.2 Surfactants 43

3.1.2 Cotton Fabrics 47

3.1.3 Capillary tubes 48

3.2 METHODS 51

3.2.1 Gravimetric Analysis 51

3.2.1.1 Analytic Balance 51

3.2.1.2 Dynamic Vapour Sorption 53

3.2.2 Thermal Activity Monitor 53

3.2.3 Microscopy Techniques 54

3.2.3.1 Confocal Microscopy 54

3.2.3.2 Time-Lapse Microscopy 55

3.2.4 Image analysis 57

3.2.4.1 Meniscus Displacement 58

3.2.4.2 Contact Angle Evaluation 61

***4* RESULTS 70**

4.1 DRYING IN COTTON FABRICS 70
4.1.1 Gravimetric results *70*
4.1.1.1 Water Hardness 70
4.1.1.2 Surfactants 73
4.1.1.3 Surfactant and Hard Water 76
4.2 DRYING IN A CAPILLARY TUBE 77
4.2.1 Meniscus Displacement *77*
4.2.2 Contact Angles *79*
4.3 TOPOGRAPHY OF COTTON TEXTILE 80
4.3.1 Imaging by CLSM *81*
4.3.1.1 Visualization of fabric microtomic slices 86
4.3.1.2 Water Layer Visualization on Cotton Surface 87
4.3.2 Reflected Light Macro Imaging *92*

***5* DISCUSSION 94**

5.1 COTTON FIBER STRUCTURE AND POROSITY 95
5.1.1 Fibers and Lumens *95*
5.1.2 Macrofibrils and Macropores *97*
5.1.3 Microfibrils and Micropores *97*
5.1.4 Elemental Fibrils and Elemental Pores *97*
5.1.5 Crystal Fibrils and Crystal Pores *98*
5.1.6 Cellulose Polymers and Polymers "Pores" *98*
5.2 DISTRIBUTION OF WATER IN COTTON FABRICS 98
5.2.1 Source of Type 1 Water *100*
5.2.2 Source of Type 2 and 3 Water *101*
5.2.3 Source of "Hard to Remove" Water *102*
5.2.4 Water Carried Over from Washer to Dryer *102*
5.3 SURFACTANT RETENTION IN FABRICS AFTER RINSING 103
5.3.1 Corrective parameters for Temperature and RH *104*
5.4 DETERMINATION OF THE CRITICAL MOISTURE CONTENT 106
5.5 CORRELATION BETWEEN CAPILLARY DRYING AND COTTON FABRICS DRYING 110
5.6 THE ROLE OF SURFACE IN DRYING PROCESS 112
5.6.1 Meniscus Surface Evaluation in a Capillary Tube *112*
5.6.2 Surfactant effect on Meniscus Surface *113*
5.7 MARANGONI EFFECT 116

6 CONCLUSIONS 118

6.1 SUMMARY 118
6.2 FUTURE WORK 119

7 BIBLIOGRAPHY 120

8 APPENDIX 138

8.1 CONFERENCES 138
8.2 EXPERIENCE IN OTHER LABORATORIES 138
8.3 WORKSHOPS AND TRAINING SCHOOLS 138

LIST OF FIGURES

Figure 1.1 Electricity use in laundry according to Golden et al.[2] 2
Figure 1.2 A computer-generated montage of cotton fabric on several scales, constructed from SEM images. 8
Figure 2.1 Water drop (denser fluid) on silica glass (solid) in air (lighter fluid) at room pressure and temperature on the left; contact angle schematic on the right. 15
Figure 2.2 Adapted from Drummond et al., 2004[42]. Equilibrium wetting configurations for decreasing water contact angles (irrespective of the initial conditions, A). Effective displacement of oil by water starts to occur for $\theta<90°$. 16
Figure 2.3 Spreading of liquid on PMMA surface: in a) the liquid is a water drop, in b) the water contains a small amount (20000 ppm) of surfactant (Na-LAS). 17
Figure 2.4 Adapted from Kowalski[166].A typical drying curve for porous type materials. ... 30
Figure 2.5 Principles of heat transfer under a boundary layer 32
Figure 2.6 a) Lubrication film near the meniscus, inside a capillary tube; b) comparison between "apparent" contact angle and thin film near wall. 38
Figure 2.7 Areas of low and high surface tension are illustrated by small and large arrows, respectively. They induce a net tangential stress, the Marangoni effect. 39
Figure 3.1 Na-LAS chemical structure. 45
Figure 3.2 Phase diagram of the Na-LAS/water system, adapted from Richards et al.[43] A micellar solution is observed at low concentrations (L_1). Next is a multi-phase region where two or more lamellar phases (L_α) co-exist with a micellar solution. In this region L'_α is used to denote the appearance of two or more L_α phases. $L_\alpha*$ indicates a situation whereby multiple L_α phases coexist with L_1. In the concentrated region, solid and multiple liquid crystalline phases co-exist.[44] 46
Figure 3.3 The complex structure of a cotton fabric, in the upper part, were compared with a lattice model, in the lower part. 49
Figure 3.4 Typical schematics of a capillary tube. 50
Figure 3.5 Scheme of the two petri dishes compared. 51
Figure 3.6 Schematics of the experimental apparatus for thermo-gravimetric analysis. 52
Figure 3.7 Schematics of the Time Lapse microscopy apparatus. 56
Figure 3.8 Water evaporates over time in a 100 μm capillary tube. 58
Figure 3.9 Analysis of meniscus shifting. 59
Figure 3.10 Example of a drying curve of DEMI water solution in a 100 μm capillary tube. 60
Figure 3.11 Two capillary tubes (100 μm) containing DEMI water. 61
Figure 3.12 Picture of meniscus in a capillary tube taken in time lapse and analyzed in image pro plus. 62
Figure 3.13 Meniscus discretization. 62
Figure 3.14 Discretized meniscus imported in Excel. 63
Figure 3.15 Trend line representation for lower and upper contact angle. 63
Figure 3.16 More accurate discretization of the meniscous. 64
Figure 4.1 Comparison of drying rate in a cotton swatch and a dish filled with water. 70
Figure 4.2 Comparison between different water drying curves in absence of cotton fabric. 71
Figure 4.3 Comparison between different drying curves in a cotton fabric soaked in water having different hardness. 71
Figure 4.4 Comparison between the drying rate in a cotton fabric and in absence of fabric for water solutions at different hardness, the two samples having the same apparent surface area. 72

Figure 4.5 Comparison between the drying rate of DEMI water and Hard water solution in absence of fabric. 73
Figure 4.6 Water content vs time in a cotton fabric (area 5 mm^2; dry weight 0,35 g) by DVS. 74
Figure 4.7 Increase percentage in drying rate due to surfactants. 75
Figure 4.8 Comparison of drying rates in a cotton swatch and in a Petri dish filled with Solution 1. 75
Figure 4.9 Increase percentage in drying rate due to water hardness. 77
Figure 4.10 Drying rate changes due to surfactant and water hardness. 77
Figure 4.11 DEMI water evaporation in a capillary tube of 100 µm. 78
Figure 4.12 Water drying in a 100 µm capillary tube as in Figure 4.11. Drying curves on the left, drying rate vs. time on the right. 79
Figure 4.13 Contact angle changes due to surfactants concentration. 80
Figure 4.14 3D reconstrustion of a single cotton fiber from a z-stack acquired in confocal microscopy. In a) arrangement in space underline the fiber section, in b) the helix structure were shown. 81
Figure 4.15 Cotton fibers visualized in confocal microscopy at high magnification (40x); in a-c) fibers thickness evaluation; in d) space between fibers measurement. 82
Figure 4.16 Single yarn 3D reconstruction by confocal microscopy. 83
Figure 4.17 Cotton fabric microstructure at high magnification (10x) by confocal microscopy 84
Figure 4.18 3D reconstruction of the z-stack showed in Figure 4.14. 85
Figure 4.19 3D Mold reconstruction from a negative z-stack of cotton fabric in silicon oil. 86
Figure 4.20 a) schematic of cotton fabric slice, warp and weft yarns are highlighted; b) image of a cotton fabric slice in bright field. 86
Figure 4.21 Expanded particular from Figure 4.20. 87
Figure 4.22 a) image of a cotton fabric slice in confocal microscopy, b) same view in polarized light. 87
Figure 4.20 Scheme of the water (gray) on the textile substrate (white). 88
Figure 4.21 Water film laying on cotton fabric visualized by confocal microscopy. 88
Figure 4.22 Section of the 3D reconstruction of the water surface (in white) on cotton fabrics (below, in black) showed in figure 4.16. 89
Figure 4.23 3D reconstruction of a z-stack acquisition in confocal microscopy. Water surface on cotton fabrics. 89
Figure 4.24 Water surface drying on cotton fabrics.3D reconstruction of a z-stack acquisition in confocal microscopy. 90
Figure 4.25 Surface area increase in time, as can be seen in Figure 4.22. 91
Figure 4.26 Water surface in a Petri dish. 92
Figure 4.27 Image sequence showing a cotton swatch before (a) and after pouring water on top (b-d). 94
Figure 4.28 Thermo-gravimetric experiment coupled whit reflected light optical imaging. 95
Figure 5.1 A computer-generated montage of a fiber segment constructed from individual transmission, adapted from *Cotton fiber chemistry and technology*[234]. 94
Figure 5.2 Essential schematics of cotton structure from mesoscopic to molecular dimension: (a) SEM image of Cotton Fabrics. (b) section of a single cotton fiber. Macrofibrils compose each fiber. (c) Each macrofibril is composed of bundles of

microfibrils. One microfibril (d), in turn, is composed by bundles of cellulose chains (c).....96
Figure 5.3 In a) a schematic of a section of cotton fabric is proposed to highlight yarns arrangement in space. In b) a microtome slice of a single cotton yarn in confocal microscopy show the fibers constituting it. In the inset single cotton fiber section as shown in fig. 5.2.b. In c) and d) a scheme represent how water evaporates from fibers. 100
Figure 5.6 Relative humidity and temperature changes during the day. §Courtesy of the American Meteorological Society 105
Figure 5.7 Drying curves of water in cotton fabrics. Raw data on the left (T and RH range for all the experiments) were compared with data scaled by using corrective parameters, on the right (T and RH of the experiment used as reference). 106
Figure 5.6 Mean drying curves of water in cotton fabrics (red) and in a Petri dish (black), on the left; same mean drying curves for NaLAS 5% in water (T and RH range for all the experiments), on the right. 106
Figure 5.7 Drying curve, on the left, compared with the Relative Humidity changes in time, on the right. 107
Figure 5.8 On the left: typical drying curve. On the right: plotting of punctual drying rate versus time and RMC double axis for cotton fabric. 108
Figure 5.8 On the left: mean drying curves in cotton fabrics as reported in Figure 5.6. On the right: punctual drying rate versus time for the curves on the left. 108
Figure 5.10 On the left: water drying curves in a cotton fabric at different boundary conditions in a RMC range from θ_k to 0. On the right: same drying curves for different surfactant solutions. 109
Figure 5.11 On the left: mean drying curves in Petri dishes as reported in Figure 5.6. On the right: punctual drying rate versus time for the curves on the left. 109
Figure 5.12 Na LAS concentration increases in time during drying. 110
Figure 5.12 On the left: water density changes with temperature; on the right: cylinder geometrical parameters and volume formula. 111
Figure 5.14 In A) a Petri dish filled with water is imagined as it will be composed by a defined number of micro-capillary tubes, each one having a meniscus with a contact angle equal to 90° to reproduce the flat surface; in the same way, in B) a wet cotton fabric is imagined to be composed by a number of micro-capillary tubes with a contact angle of 33°. 112
Figure 5.15 3D meniscous shape and surface changes with contact angle variations. 113
Figure 5.16 Drying rate changes in 100 μm capillary tubes depending on NaLAS surfactant concentration. 114
Figure 5.17 Time lapse microscopy observation: Drying rate changes in 100 μm capillary tubes depending on NaLAS surfactant concentrations. Red bars underline the final difference in drying rates. 115
Figure 5.18 NaLAS concentration, contact angle, meniscus surface and drying rate correlation. 115
Figure 5.19 Drying rates for different NaLAS concentrations in the same conditions of Figure 5.18. 116
Figure 5.20 Rhodamine-B chemical structure. 117
Figure 5.21 Concentration gradient visualization in a capillary tube. 117

LIST OF TABLES

Table 3.1: Summary of the saline concentration solutions.....43
Table 3.2: PH characterization of water solutions.....43
Table 3.3: Na-LAS concentration and PH characterization of diluted surfactant solutions .48
Table 3.4: Characteristics of Capillary Tubes.....53
Table 3.4: Cotton fabrics main characteristics 49
Table 3.5: Conversion factor for the optical magnification used 63
Table 4.1: DEMI water and surfactants solutions compositions and rate values. 74
Table 4.2: Surfactant and hard water solution effect on the drying rate in a cotton fabric...76
Table 5.1: Mass and volume values in laundry. 94

1 INTRODUCTION

"I feel more confident than ever that the power to save the planet rests with the individual consumer."
Denis Hayes

Drying of porous media is a fundamental operation in a number of applications, including material processing (such as in the production of food, wood, paper, textiles, pharmaceuticals and washing powders), agriculture, soil technology, recovery of volatile hydrocarbons from oil reservoirs, cosmetics and building restoration. Although much work has been done in these application areas within the context of different disciplines, the current understanding of drying of porous media is still limited and the prediction of drying rates remains a challenging problem.

The main objective of this PhD thesis is to investigate the driving forces of the process to identify the key parameters and the rate limiting steps. This problem was tackled by using a multi-scale approach combining the study of the governing mechanisms at the pore scale through advanced microscopy techniques with evaluation of physicochemical properties through thermal analysis. In fact, handling the different spatial and time scales relevant in the drying process of a porous medium is one of the most challenging problems in investigating fabrics drying. This work is relevant for the identification of rate enhancing additives of possible industrial application.

1.1 Sustainability and innovation in laundry

Golden et al.[2] examined energy, carbon and water impacts from residential laundry in the United States in 2010. The report found washing and drying clothes in the average American household was responsible for consuming 9718 gallons of water, 1991 kWh of electricity and 1 metric ton of CO_2 emissions (see Figure 1.1).

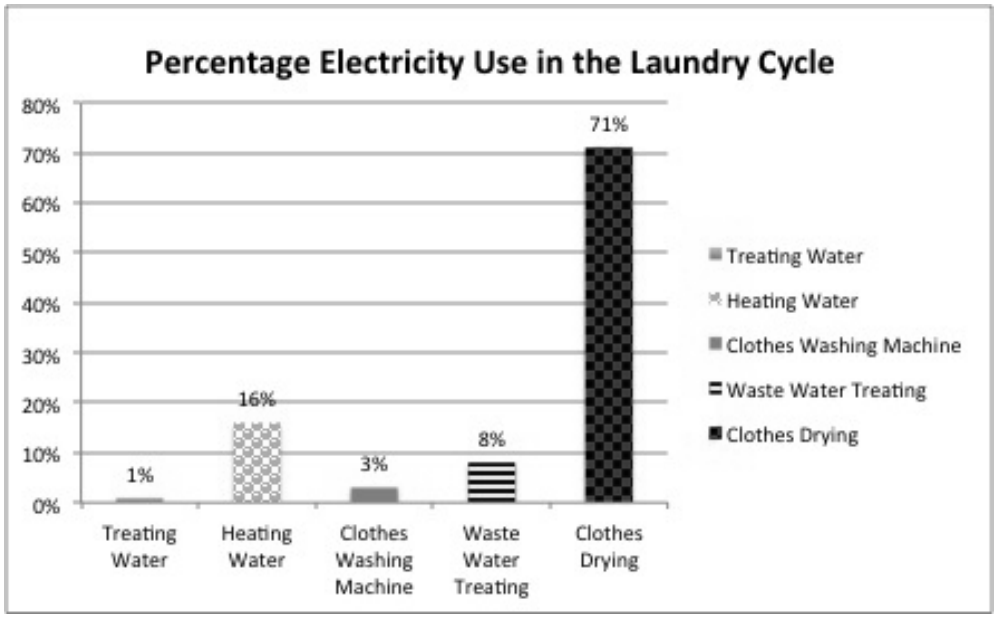

Figure 1.1 Electricity use in laundry according to Golden et al.[2]

The large amount of energy used in household dryers has been estimated as 66 billion kWh per year (or 5.8% of all residential electricity consumption) in US[3] and as 25.2 billion kWh per year in Europe[4], where the dryer market is undergoing a fast growth (the estimated number of dryers in 2020 is 70 million units). These numbers show that even small improvements of drying efficiency can lead to major energy savings. The average home clothes dryer has a carbon footprint of approximately 2 kilograms (4.4 pounds) of CO_2 per load of laundry dried[5]. Energy Star, a United States government program concerned with energy efficiency in consumer products, does not rate clothes dryers.

In the European Union, the EU energy labeling system is applied to dryers; dryers are classified with a label from A (best) to G (worst) according to the amount of energy used per kilogram of clothes (kWh/kg). Sensor dryers can automatically sense that clothes are dry and switch off. This means over-drying is not as frequent. Most of the European market sells sensor dryers now and are normally available in condenser and vented dryers.

On this side, Europe is in a leading position as compared to US thanks to several initiatives, such as the introduction of an energy label for tumble

driers (Commission Directive 95/13/EC; [6]), mostly targeted at increasing the efficiency of the drying machines. The latter is generally defined as the ratio of the heat required to remove water from a standard laundry load (containing 80% of initial moisture on a dry basis) and the energy actually consumed. It should be pointed out that in this definition of dryer efficiency the evaluation of heat requirement is only based on the latent heat of evaporation of water, without taking into account that textiles are porous media with a significant spatial confinement of moisture.

In this respect, a review on thermodynamic calculation of heat requirement in fabrics drying will be made in chapter 2 as a basis for a rigorous expression of dryer efficiency and of its theoretical upper limit. This will help both manufacturers in setting meaningful standards and R&D benchmarks and consumers in better product selection.

1.1.1 Carbon Friendly Dryers

Recently, several progress have been done in improving dryers efficiency. Only in the UK more than 40% of households use a tumble dryer and almost 4 million dryers are sold every year. Tumble dryers account for a massive 4.3% of the UK's entire domestic energy consumption. This percentage could be significantly reduced if the UK was to convert to gas tumble-drying. British manufacturers Crosslee launch in 2008 a 7kg capacity gas tumble dryer range. This product is of interest because it claims to have a very low carbon footprint and running costs. However, it must be remembered that it needs a gas supply to run as well as electric.

The expansion of this new gas dryer range offers functions to cater for the technical needs of the energy conscious consumer. The range includes a reverse action model, working to reduce the possibility of tangled clothes leading to easy ironing. White Knight have released the 7kg sensing version, automatically switching off when the selected level of dryness is reached, avoiding further unnecessary CO^2 emissions. Gas dryers can be faster and 2/3 cheaper to run, saving time, money and of course the

environment. According to White Knight there are several benefits of using a gas tumble dryer as opposed to an electric model: lowest running costs, shortest drying times (the fastest drying domestic tumble dryer dries a full load in 60 minutes) and lowest carbon emissions.

There are A rated electric dryers with heat pumps that are not too far off the efficiency and carbon figures for this gas dryer; however, they are still "higher", are more complex and take much longer to dry clothes so a gas tumble dryer is a viable option to consider[7].

On the same year AEG-Electrolux release the Lavatherm T59800, the first A rated condenser dryer which takes as little as 85 minutes to dry cottons (Cotton cupboard dry program takes 110 minutes at 1400 spin. Cotton iron dry takes 85 minutes at 1400 spin), consumes half the energy of a similar sized C rated dryer (2.4 kWh) and dries clothes so gently that even wool and silks can be can be tumble dried it. The T59800 uses a specially developed 'Heat pump' technology that works like a refrigerator in reverse to achieve this unprecedented energy efficiency. The Energy consumption is so low it exceeds the requirements for A Energy rating by 30%.

The lower temperature drying (5°C less than conventional models) means even delicate fabrics like wool and silk can be dried safely. For consumers who plan to install a dryer in the kitchen, the heat pump technology is also far quieter than the traditional technology (65 decibel instead of 70 decibel)[8].

1.1.2 Low-Carbon Detergents

Until now the recipe for a low-carbon load of laundry was to use liquid detergent instead of powder and to wash clothes in cool water and hang them out to dry[5].

That's the message shoppers get when they walk down the detergent aisles at Tesco PLC stores in the U.K. Starting this spring, the retailer began slapping footprint-shaped carbon labels on Tesco-brand laundry detergent. Along with the carbon-footprint number, the label offers tips about lowering the score.

The carbon footprint of a load of laundry done with actual detergent varies from 0.6 kg to 0.9 kg, depending on what form of detergent is used. According to Procter & Gamble Co., the average American family does about 300 loads of laundry per year, or about six loads per week. That suggests a per-family carbon footprint from doing laundry of about 218 kg per year, or about 4.5 kg per week. And that doesn't include running the dryer.

According to Tesco, as reported by the Wall Street Journal in 2009, solid capsules of detergent have the highest carbon footprint, followed by powder; liquid detergent has a significantly lower carbon footprint but the lowest footprint comes from concentrated liquid. That's because making solid detergent uses more energy than making the liquid variety.

Most US household currently own and use the top-loading vertical axis (v-axis) agitator type washers, which use large amounts of water as well as additional energy to heat the water. More sustainable laundry practices include the use of energy- and water-efficient front-loading horizontal-axis (h-axis) washers[9]. These washers have been demonstrated to use 38% less water and 58% less energy than the standard top-loading v-axis models[10].

Doing the wash in cooler water, 30°C instead of 40°C, will shave the carbon footprint of each load by 0.14 kg. That's as much of a reduction as you get from switching to liquid from powder.

The biggest way to cut the environmental impact of cleaning clothes, however, is to stop using a clothes dryer. Drying laundry outside on a line will cut the carbon footprint of every load by a whopping 2 kg CO_2.

1.1.3 Energy Efficient Laundry Process

With the rising cost of energy and increased concerns for pollution and greenhouse gas emissions from power generation, increased focus is being put on energy efficiency. Between 2001 and 2004 a study developed by the Department of Energy of the United States looks at several approaches to reducing energy consumption in clothes care appliances by considering the appliances and laundry chemistry as a system, rather than individually[12]. The resulting solution to reducing the moisture at the end of the wash cycle was by improving the ribbed basket design. The ribs had a 20% improvement as compared to the baseline smooth plastic basket.

The dryer system investigated several process techniques in addition to sensing and control. The process techniques, such as reversible drum, variable speed drum & fan, proved to be insignificant in effecting energy savings. Basic control techniques provided no energy savings and the effort focused on advanced control algorithms and sensor implementations. The final energy savings averaged 8% with one case as high as 17%. This gain was achieved by improving the end-of-cycle determination.

Procter & Gamble (P&G) also contributed to the findings of this report. P&G explored chemistry additives that would enable faster evaporation rates in the dryer and increase moisture extraction in the washer. In the dryer, evaporation could be improved, but the concentrations and delivery methods required were incompatible with consumer requirements. Silicone surfactants were found to reduce moisture content by over 20%, however, compared to existing market products, this improvement was not sufficient to initiate new product development.

1.2 Research objectives

The motivation of this PhD work lies in the high-costs associated with drying of porous media, which is one of the most energy-intensive operations not only at the industrial level, but also in housekeeping. In fact, a large fraction of home energy expenditure is due to clothes drying, which is as expensive as laundry (if not more) in countries where dryers are typically used (e.g., because of adverse weather conditions). The current industrial strategy to reduce drying costs is focussed on improving mechanical and thermal dryer engineering design, which basically neglects the fact that textiles are inhomogeneous materials. On the contrary, the idea behind this PhD project is to enhance clothes drying rate by turning the attention from the dryer machine to the drying process itself. The latter can be achieved by using appropriate additives in the washing machine. Such additives would also improve the rate of line drying indoors, with the advantages of lower energy withdrawal from house heating and less time of clothes hanging inside. In fact, people often switch from line-drying to machine drying because line-drying is too slow and they want to have their items dried faster. From the industrial side, high gains are also expected in the detergent industry, which would receive a technology boost in terms of product formulation. Elucidating the moisture-transport process in clothing, which is one of the most important factors influencing the dynamic comfort in practical wear situations and to be accounted for in clothing thermal engineering design6, is also relevant for the textile industry.

1.3 Textile as Porous Media

A textile is a flexible woven tissue made of a network of yarns or threads, which in turn consist of interlocked fibers of synthetic (e.g., polyester) or natural (e.g., cotton) origin. Laundry water is retained within the pores of the clothes microstructure, which are formed either between the yarns (100 μm) or between the fibers inside a yarn (10 μm) or within a single fiber (0.5

μm). These different spatial scales are schematically shown in the following Figure 1.2.

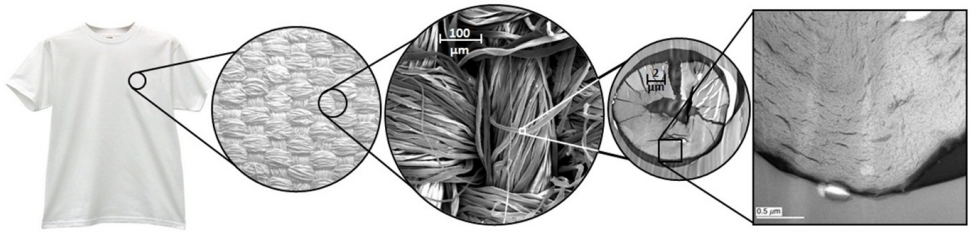

Figure 1.2 A computer-generated montage of cotton fabric on several scales, constructed from SEM images.

One of the main challenges of this work was to take into account such water retaining fabric microstructure, which can be regarded as a porous medium with a complex hierarchical texture. Several mechanisms have been speculated to be at play at the pore scale: vapor diffusion, which is modeled by Fick's law with a diffusivity dependent on pore tortuosity, capillary flow due to pressure differences depending on menisci curvature (Laplace equation), gas transport elicited by pressure gradients according to Darcy's law. Another possible mechanism which has recently attracted much attention is liquid flow in the films developing along the corners of rectangular cross-section pores, which acts to increase the drying rate as compared to circular cross-section capillaries[15, 16]. The same effect has been invoked to explain the higher drying rate found from a cell filled with a dense packing of silica spheres as compared to an empty cell[17, 18]. Enhanced vapor diffusion is another mechanism of which, although often invoked, no direct experimental proof has been given so far[19]. The enhancement would be due to condensation/evaporation across isolated liquid islands, leading to a vapor pressure lowering (dependent on curvature according to Kelvin equation). Further complications, such as liquid or vapor transport induced by thermal gradients and variations of surface tension and contact angles with temperature, arise when heat transfer is also taken into account. Surface tension gradients can also be induced by concentration gradient in multi-component liquid mixtures.

Although invasion percolation theory and pore network simulations have provided helpful insight in this problem, the physical understanding of drying dynamics is still incomplete and the prediction of drying rate is still a challenging issue even under isothermal conditions (slow drying). A further difficulty arises from the coupling between mass and heat transfer during the drying process, which is usually carried out by means of a stream of hot air (forced convection). While a complete analysis would require to include mass, heat and momentum transfer mechanisms, simplified models have been proposed for specific industrial drying application[20].

However, the complexity of the problem, together with the lack of a rigorous thermodynamic analysis, makes it difficult to obtain predictions of rate of drying. In particular, it is not clear, whether there is at the controlling mechanism of the process. It is likely that different regimes can become dominant depending on the pore size and thermodynamic parameters, as well as on non-dimensional parameters.

In conclusion, several open key questions concerning the physics of fabrics drying at the micro-scale need still to be answered. How is water spatially distributed and what is the interface dynamics in the drying process? What are the physicochemical mechanisms governing fabric drying? What is the interplay between mass and heat transfer? Is there a controlling mechanism, which can be exploited in order to enhance drying efficiency? Resolving these challenging issues would be a scientific breakthrough in the general framework of transport in porous media and the rationale for the development of predictive models of clothes drying, which is a key step to address the problem of enhancing clothes drying rate. In the following chapter a deep theoretical review as a basis for the experimental section will be made, having the intention to answer some questions aroused in this chapter and to let other question arise.

2 THEORETICAL BACKGROUND

"The lure of the distant and the difficult is deceptive.
The great opportunity is where you are."
John Burroughs

In this chapter the state of the art on the study of the flow of a multiphase fluid in a porous medium is presented. To understand the key role of this process in everyday life, some definitions are provided useful to the understanding of the structure of porous materials, such as porosity, permeability and the interfacial tension. Following the equations governing the mass and heat transport are presented, and then refer to an application of this physical phenomenon: drying rate process in cotton fabrics. This topic finds also application in similar fields like paper and food industry. Various experimental, theoretical, and computer simulation approaches to evaporation in textiles will be also reviewed.

From the phenomenological point of view, clothes drying apparently follow the typical behaviour of porous media, which is sketched in the following figure. The fabric moisture content on a dry basis decreases at a constant rate until a critical point is reached, marking the transition to the falling rate regime. The commonly accepted interpretation of this behaviour is that water in the larger pores between yarns is free to move to the outer fabric surface, where temperature remains fixed at the equilibrium value (adiabatic saturation temperature). In this region drying should be essentially dominated by external heat transfer. Once water recedes in the smaller pores transport to the outer surface is hindered and drying proceeds at a falling rate. Since saturation conditions are not present any more at the outer surface, temperature does not remain constant and starts growing with time tending to the value of air temperature.

2.1 Flow in Porous Media

The flow of a fluid in a porous medium is a topic of great interest in various fields, such as in the filtration of waste water, in the drying processes and in the study of leaching of pollutants within an aquifer; it also located strong response in the chemical industry, for the study of the flow of fluids in fixed bed reactors, and in the oil industry, for the extraction of fossil fuels. Issues that are common to all of these fields are the complexity of pore structure and its effects on the way the fluids of interest can flow and distribute throughout the porous media. Furthermore, different mechanisms can be at play, including heat and mass transfer, phase behavior and viscous, buoyancy, and capillary forces. There will be discussed flow phenomena only in a static porous medium, i.e., a medium whose morphology does not change during a given process.

2.1.1 Porous Media Structure

A porous medium consists of an interconnected three-dimensional network of pore space with non-uniform size and shape, characterized by a certain degree of vacuum and high specific surface. The variety of different pore shapes and sizes is different every time, depending on their origin. A porous medium can be described as a multiphase heterogeneous system made of both fluid and solid phases, whose physical properties are strongly influenced by the pores number, size, shape and degree of interconnection[21]. Two important macroscopic parameters to describe the internal structure of porous medium are porosity and permeability. Porosity, or vacuum degree φ is defined as the amount of voids contained in the porous medium. It is a dimensionless scalar parameter varying between 0 and 1, indicates the ability of the medium to contain fluids inside it, and is defined as:

$$\varphi = \frac{V_p}{V_b} \qquad (1)$$

where V_b is the volume of the porous medium and V_p is the sum of the volumes of individual pores contained in the volume V_b. Permeability k describe the ability of a porous medium to allow the flow of a fluid through

it. k is a vectorial quantity, depending on the direction along which it is measured. The flow of a fluid in a porous media is described by the Darcy's law:

$$\frac{Q}{A} = -\frac{k}{\eta}(\nabla P - \rho \boldsymbol{g}) \quad (2)$$

where Q is the flow rate of a fluid of viscosity η; A is the surface area of the porous medium, ∇P is a gradient of negative pressure (ie, the flow moves in the direction of decreasing pressure); ρ and $\boldsymbol{g}$ are the liquid density and gravity acceleration respectively. It is evident that the increase of k causes the decrease of the resistance offered to the flow[22].

Two characteristic length scales can be identified to describe a porous medium[23], making basic differentiation between the macroscopic and microscopic level. In the former, a representative elementary volume REV, that is much larger than the characteristic dimension of the pore, defines the scale of the system. In this case the system parameters are averaged over the elementary volume. This approach is adequate when the molecular dimensions are negligible compared to the average size of the pores, as in the study of the mass or heat transport in porous media. Regarding the microscopic level (i.e. pore scale), the material structure can be defined by the degree of vacuum, the pore degree of interconnected exposed surfaces and the distribution of the pores. According to the International Union of Pure and Applied Chemistry, the classification of the pores is based on their sizes as follow: nano-pores, with sizes ≤ 2 nm; meso-pores, with sizes in the range 2–50 nm; macro-pores with sizes ≥ 50 nm[24]. An example of porous media structured on all length scales, with no exception for the pore one are the geological formations[25, 26], that can also be characterized by non-homogeneity and anisotropy, making their properties dependent on the direction in which they are being evaluate[27, 28].

In light of the important role that porous media play in many aspect of science and technology, they have been widely studied, and many different

techniques have been applied to describe their geometry characteristics[721], such as mercury porosimetry[29, 30], adsorption-desorption methods[31], small angle neutron scattering (SANS)[32] and nuclear magnetic resonance (NMR)[33, 34]. The latter is based on the fact that certain atomic nuclei absorb and re-emit electromagnetic radiation in a magnetic field, and it is applicable to any kind of sample that contains nuclei possessing spin. In the specific case of a porous medium, different relaxation times for the NMR induced excitations are expected for molecules in the surface area and in the bulk volume of the pore[35]. Thus, NMR is a well-established technique for the characterization of both homogenous and heterogeneous[36] porous media, allowing the determination of characteristics[37] such as porosity and pore size distribution, permeability, water saturation and wettability.

2.1.2 Wettability and Contact Angle

Since it is very arduous to represent the physical structure of a porous medium, is even more complicate to describe the fluid flow through it. One of the principal parameters that affects the flow characteristics and the fluid distribution within a porous medium is wettability, that influences the way whereby a fluid expands on a solid and forms wetting films[38]. Thus, the fluid distribution in a porous medium is controlled by wetting, consenting the achievement of the lowest possible energy content state[39-42]. Wettability affects relative distribution of fluids[43], relative permeability[44], electrical conductivity[45, 46] and capillary pressure[47]. Otherwise, wettability can be affected by temperature[48], chemical agents such as surfactants[49] and by the presence of nano-particles dispersed in the liquid phase[50-53]. The degree of wetting of a solid surface is determined by the ability of a liquid to stay in contact with a solid surface, and is characterized by the contact angle θ. This is determined by a force balance when the interfaces of denser(water) and lighter(air) fluid meet a solid surface at a three-phase contact point, as illustrated in Figure 2.1. θ is defined by the Young's equation (Eq. 3)

$$cos\ (\theta) = (\sigma_{sl} - \sigma_{sd})/\sigma_{ld} \qquad (3)$$

where σ is the interfacial tension (N/m), with subscripts indicating the phases. i.e. σ_{sl} is referred to solid and lighter fluid; σ_{sd} to solid and denser fluid; σ_{ld} to lighter and denser fluids[54].

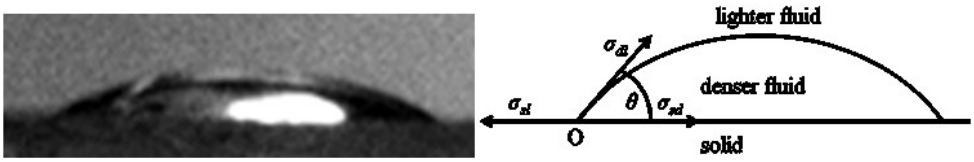

Figure 2.1 Water drop (denser fluid) on silica glass (solid) in air (lighter fluid) at room pressure and temperature on the left; contact angle schematic on the right.

Different initial conditions may then lead to different final configurations. When θ<90° the denser fluid wets the solid surface, while when θ>90° the lighter fluid wets the solid surface. In Figure 2.2 a case of spontaneous imbibition is illustrated. Starting from a condition in which a pore is saturated solely by water or by oil (Figure 2.2.A) the resulting equilibrium situations (Figure 2.2 from B to F) correspond to decreased values of θ[42]. Complete water-wettability occurs when $\theta \approx 0$ ($\cos \theta \approx 1$). In this case, a repulsive force between the surface and the oil across water occurs, and water shows a higher affinity for the surface, displacing the oil from the surface (Figure 2.2E and F).

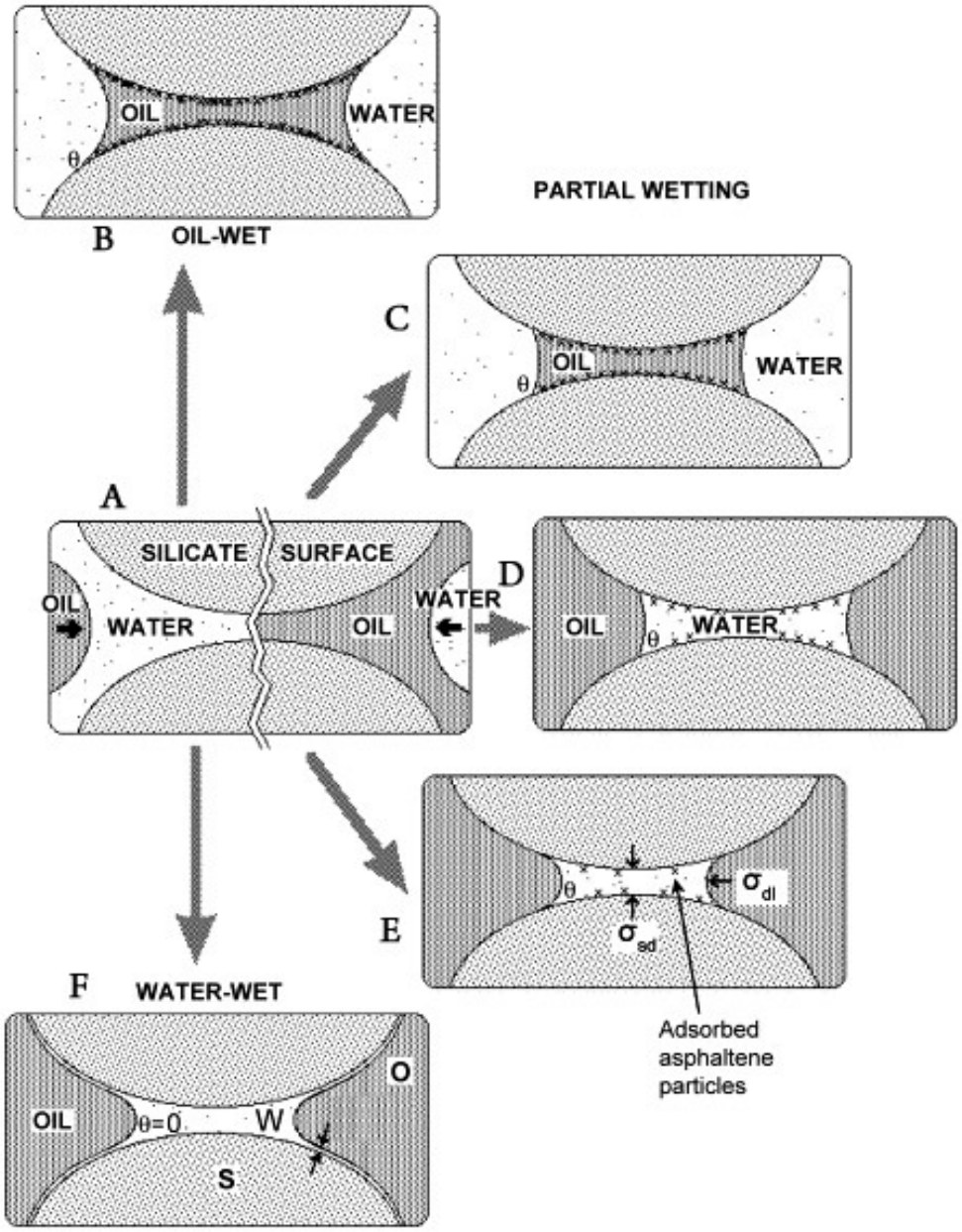

Figure 2.2 Adapted from Drummond et al., 2004[42]. Equilibrium wetting configurations for decreasing water contact angles (irrespective of the initial conditions, A). Effective displacement of oil by water starts to occur for θ<90°.

Low value of solid-lighter fluid interfacial tension σ_{sl} and high values of solid-denser fluid interfacial tension σ_{sd} are related to high values of $cos\theta$ and, consequently, low contact angle (Figure 2.2E); while low values of σ_{sd} mean low $cos\theta$ and high θ (Figure 2.2C). Thus, for effective displacement by water (θ<90°) (Figure 2.2D and E), the forces that acts between oil and

surfaces (across the water phase) must be repulsive or only weakly attractive. In addition to contact angle, an useful parameter for evaluating wetting degree is the spreading coefficient, that indicates if a fluid completely (wetting fluid) wets a surface, creating a stable hydraulically continuous film even at low saturation, or only forms a fluid layer (spreading film) onto the interface (see Figure 2.3).

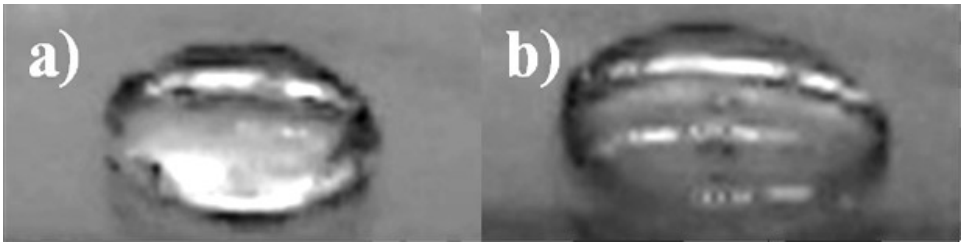

Figure 2.3 Spreading of liquid on PMMA surface: in a) the liquid is a water drop, in b) the water contains a small amount (20000 ppm) of surfactant (Na-LAS).

The wetting fluid can be advancing or receding: advancing contact angles occur in the displacement of oil by water, while the receding ones are operative when water is displaced by oil. On the other hand, when a fluid does not wet the solid is called non-wetting fluid[55-59]. Lenormand[60], by using experiment and computer simulations demonstrated the existence of three types of basic displacement when a non-wetting fluid invades a two-dimensional porous medium: i) capillary fingering (capillary forces > viscous forces), ii) viscous fingering (invading fluid less viscous than the defending), iii) stable displacement in the opposite case. The displacement have been characterized by statistical models: invasion percolation, diffusion limited aggregation (DLA) and anti-DLA[61]. Many transport process can be idealized as transport of fluid into a medium, but if the fluid path is determined by the medium and medium itself is random, the process is called percolation[62-64], this concept was introduced by Broadbent and Hammersley[65].

In natural porous media, three phases often coexist, i.e. water, oil, and gas. The effect of both medium characteristics (pore geometry and wettability) and interfacial tensions can be combined in a single factor, the capillary

pressure, that controls fluids equilibrium configurations, as described in detail in the following section. Thus, changes in capillary pressure affect the entrapment and the displacement in a gas/oil/water system, modifying the wetting properties. For example, in a water-wet condition, water can form stable wetting film along the pore walls, while oil forms a spreading film of variable thickness depending on the pore structure and on the pressure of the gas entering the pores. When gas is injected in the oil-wet condition, instead, interface movements are controlled by either the oil-gas or the oil–water interfaces, in dependence on the pore geometry, and on the values of interfacial tensions and capillary pressure. In this case, oil forms stable wetting films of thickness variable with the pore structure, and water and gas, being the non-wetting fluids, are cut apart by a spreading film of oil[59].

2.1.3 Capillarity Effect Inside Pores

Capillary pressure, together with geometrical parameters such as size of pores, tortuosity of capillaries, and porosity, as previously described in Section 2.1.2, is a key factor in the permeability processes in a porous medium. The motion of a finite liquid volume constrained between solid surfaces is governed by a complex interplay of capillary, viscous, and gravitational forces. In the absence of external force (pressure) and negligible gravity the flow of a wetting liquid into a porous medium is governed solely by capillary force[66, 67]. The potential gradient and liquid flow are caused by a difference in the capillary pressures on the free liquid at the porous medium surface (inlet) and at the liquid interface within the porous medium. The classical theory of capillarity, developed by Gibbs, postulate that the internal energy U of the interface is a function of the entropy S, the mole number N_i of the i components, the surface area A, and of the two principal curvatures of the surface c_1 and c_2[68]. If the concept of surface tension is introduced and a moderate curvature is assumed, the equation is:

$$dU = TdA + \sum \mu i \, dNi + \gamma dA \qquad (4)$$

where T is the temperature, μ_i the chemical potential of the i component and $\boldsymbol{\gamma}$ the surface tension. The well-known Laplace equation is based on eq. 4 as follows:

$$J\gamma = P_1 - P_2 \quad (5)$$

where $J=c_1+c_2$ is the mean curvature and P_1-P_2 is the pressure drop between two adjacent phases[68]. A particular expression of the Laplace equation is reported in eq. 6.

$$P_C = P_N - P_W = \frac{2\sigma_{NW}}{R}\cos\theta \quad (6)$$

where R is the capillary radius, θ is the contact angle, σ is the interfacial tension between the non-wetting and the wetting fluid, P_N and P_W are the pressure of the non-wetting and the wetting fluid respectively, and Pc is the capillary pressure. Note that $P_C = P_{oil} - P_{water}$, for a water-wet system, while $Pc = P_{water} - P_{oil}$ for an oil-wet system. If $P_C < 0$ a wetting reversal occurs. In presence of air as non-wetting fluid, as happens for air/water and air/oil systems, air pressure is often neglected, taking the liquid pressure in respect of atmospheric pressure[69]. Since eq. 5 and 6 are referred to situations of weakly curved interfaces, they can't be applied to cases in which the surfaces curvature is large. Boruvka and Neumann's theory[70] fulfills all the thermodynamics and mathematics conditions, generalizing the classical Laplace theory and maintaining the curvature terms in the interface fundamental equation[71, 72]. In addition to theoretical studies, a number of experimental approaches has been used to study the capillary flow in porous media, such as capillary rise[73, 74] and slug[75] and plug[76] motion in a capillary tube, as shown in the following sub-sections.

2.1.3.1 Capillary Rise

Because of the complexity of the pore network structure, capillary flow in porous media has been often simplified by using a two-phase model system in a single capillary tube flow[70, 76-81]. For decades, the capillarity phenomena

(also known as *wicking*) has been described by the Washburn equation[82] that derives the Poiseuille's law

$$\frac{dh}{dt} = \frac{R_D^2}{8\eta}\frac{\Delta P}{h} \quad (7)$$

where h is the height reached by the liquid menisci at time t, R is the mean hydrodynamic radius, η is the fluid viscosity and ΔP is the difference between capillary pressure P_C and hydrostatic pressure:

$$\Delta P = P_C - \rho g h \quad (8)$$

It is important to underline that R_D is dependent on the tortuosity of these pores, while in P_C is present R, that corresponds to the geometrical radius of pores. Thus, in the case that the hydrostatic pressure can be neglected ($h << h_{eq}$), integration of eq. 7 leads to the Washburn's equation[83],

$$h^2 = \frac{r\gamma \cos\theta}{2\eta} t \quad (9)$$

where $r = R^2_D/R$. When r and θ are unknown, commonly a total wetting fluid is used ($\theta=0$, $\cos\theta=1$) to calculate r, and then columns of constant packing dimensions can be used to calculate the non-wetting fluids contact angle. Siebold et al.[74] used the Washburn's equation in capillary rise experiments to measure the contact angles of several total wetting liquids, using both glass capillaries and packed powders columns. The capillary rise of a liquid in the gap between two cylinders has also been studied:[73] the relation between the height of the liquid meniscus at equilibrium and the gap between the cylinders is found to be nearly inversely proportional. The wicking behavior has been carefully predicted by both theoretical calculations and experimental tests. The same approach has been used for textile fibers, as example of complex porous media, but due to the very complex structure and the many parameters involved, the wicking in textile structures and its mechanism has been not fully understood. To overcome experimental difficulties, computational simulation[80] has been used to observe some processes at the micro- and nano-scale level. In a recent work,

many-body dissipative particle dynamics (MDPD) method has been applied to the study of water-oil displacement in capillaries[79], allowing the change of some fundamental parameters, such as wettability and miscibility of water and oil.

2.1.3.2 Surface Tension vs. Contact Angle

Two-phase flow regime in small circular tubes have been the subject of a number of studies[84-87], founding that surface tension is an important parameter, for the determination of different flow regimes. Concerning motion and evaporation in a capillary, an important parameter that determines the flow characteristics in a tube is the contact angle. Many theories have been developed to quantify how contact angle can be affected by several factors[88], such as by the capillary number[89, 90], tube diameter[91], driving pressure, temperature, and liquid plug length.[76] It has been found that, in a capillary tube, the flow resistance of a fluid is significantly affected by the advancing contact angle. Recently, three-phase flows behavior in capillaries with different internal diameter has been analyzed, predicting the spontaneous motion of the water/oil/gas system[77].

In conclusion, the surface tension gives indications about fluid-fluid interaction while the contact angle also contains information about the fluids interaction with the solid surface and its geometry; as often occurs, theory and practice collide: surface tension is much easier to be calculated, while experimental measures for contact angle can give different values and, on the micro- and nano- scale, the very definition of contact “angle” is no more valid, but it start to be named as “apparent” contact angle (as discussed in the next session).

2.2 Drying Process in Porous Media

Drying of porous media is an intensive energy process: a huge amount of energy is needed to force the liquid phase out from the smallest pores. In addiction energy is consumed in various means by the washing process. Electricity is required to power the motor for spin and agitation and for the automatic controls. Hot water energy is used is heating water from the house supply. The recent trend for energy conservation has been to develop washers that utilize less hot water. Horizontal-axis (HA) or front-loading washers use less water than conventional top loading or vertical axis (VA) machines and have been gaining market share. HA machines are still considerably more expensive than conventional top-loading machine (VA) and have longer cycle times than VA machines. HA machines currently have limited market penetration with about 15% of washer sales being HA1. This project focuses on improvements for traditional VA machines.

Nearly one-half of all energy consumed during the laundry process is in the form of hot water. About 40% of the total energy is used for heating the air in the dryer and the remaining 10% is used to power the motor and control systems. There are several opportunities to reduce the energy usage for the clothes washing process. The obvious energy reduction opportunity for the washer machine is hot water reduction. Advances in laundry chemistry will one day enable effective low temperature detergents for significant energy savings.

A second opportunity for improving energy efficiency via the washing machine is by improving water extraction. The amount of moisture remaining (RMC) in the clothes after the final spin cycle in the washer is transferred to the dryer and must be removed by evaporation. Reducing the RMC reduces the heat required during the drying cycle. The goal of this project is to reduce RMC by 20% from the baseline washer. Only about 15% of the energy used in the drying process is due to the mechanical action of the washer. Extending the spin time or increasing spin speed comes with

a very low energy cost. According to literature[92-94], approximately 40% of the laundry process energy is used by the dryer, 50 by hot water usage, and 10% in electricity for the washer motor and controls. The dryer energy is impacted by the amount of water remaining in the clothing after the final spin of the wash cycle. This water content, or Remaining Moisture Content, RMC, is defined as the amount of water, by weight, which remains in the clothing tested, shown as a percentage of the bone-dry weight of the clothing in Eq. 10.

$$\mathrm{RMC} = \frac{W_c - W_i}{W_i} \cdot 100 \qquad (10)$$

Dryers are one of the highest electrical energy users in U.S. households. The drying time for a load of clothes can be up to twice as long as washing time, bottlenecking the laundry process. The falling rate stage presents the core difficulty in detecting when the cycle is complete. The RMC and most other process values are asymptotic to the steady-state value and have very low slopes. High sensitivity sensors are not currently available to detect this type of event. Two areas of improvement are evident: improve the efficiency of the constant rate stage and improve end-of-cycle (EOC) detection to reduce energy usage in the drying stage.

Water extraction can also be affected by chemistry. The primary force holding moisture in the clothing fabric is capillary action. Small pores and channels in the fibers create large capillary forces that cannot be overcome by the centrifugal forces of the spin cycle. A prime driver of capillary action is surface tension of the water. Using chemical additives, the surface tension can be reduced, improving the water extraction. In this paragraph the heat and transport processes concerning drying were illustrated, at first for all the porous media and then for the specific case of the laundry.

2.2.1 Transport Phenomena

The collective behavior of a porous medium is dependent on transport phenomena such as diffusion, conduction, convection, the way the fluids are

spread in the medium and, most of all, system morphology[33, 95-97]. As outlined in Helmig et al.[98], the relevant flow processes can be described for the different length scales described in section 2, i.e. the pore scale and the representative elementary volume REV. Here, the equations that govern multiphase flow in porous media at the REV scale[99, 100], derived from the balance of quantities as mass, momentum, and energy are generally introduced, allowing their application to a number of works present in the literature. The balance equations for the mass of a component in a multiphase system is:

$$\frac{\partial}{\partial t}\left(\rho_\alpha \varphi_\alpha X_\alpha^k\right) + \nabla \cdot \left(\rho_\alpha \varphi S_\alpha X_\alpha^k u_\alpha + J_\alpha^k\right) = I_\alpha^k + q_\alpha^k \qquad (11)$$

where ρ is density, φ is porosity, S is fluid-phase saturation, X is mass fraction, u is velocity, J is diffusive flux, I is interphase mass exchange, and q the external sources and sinks. The subscripts k and α denote the component and the phase, respectively. Apart from the solid phase, a system can be made of an aqueous (w), a non-aqueous (n), and a gas (g) phase and of N components:

$$k \in \{1,2,\ldots,N\}; \qquad \alpha \in \{w,n,g\} \qquad (12)$$

Given the following constraints and definitions

$$\sum_k J_\alpha^k = 0, \quad \sum_k X_\alpha^k = 1, \quad \sum_k I_\alpha^k = I_\alpha, \quad \sum_k q_\alpha^k = q_\alpha,$$
$$\sum_\alpha I_\alpha^k = 0, \quad \sum_\alpha S_\alpha = 1, \quad \sum_\alpha q_\alpha^k = q \qquad (13)$$

The balance equation (11) can be expressed as one equation for each phase

$$\frac{\partial}{\partial t}(\rho_\alpha \varphi S_\alpha) + \nabla \cdot (\rho_\alpha \varphi u_\alpha) = I_\alpha + q_\alpha \qquad (14)$$

or one equation for each component

$$\sum_\alpha \frac{\partial}{\partial t}\left(\rho_\alpha \varphi X_\alpha^k\right) + \sum_\alpha \nabla \cdot \left(\rho_\alpha \varphi S_\alpha X_\alpha^k u_\alpha + J_\alpha^k\right) = q^k \qquad (15)$$

The flux of a fluid phase is generally expressed by the extended Darcy equation (2) as previously described in section 2.1.1, while a separate

momentum balance equation is usually not taken into account[99]. The diffusive flux can be well defined by a Fickian approach

$$J_{\alpha}^{k} = -D_{\alpha}^{k}\nabla\left(\rho_{\alpha,mol}X_{\alpha}^{k}\right) \qquad (16)$$

where D is the diffusion tensor and $\rho_{\alpha,mol}$ the molar density of phase α. When the transport results in a nonlinear growth of the variance of displacement with time is said to be non-Fickian[101], being impossible to described it by Fick's law. Experimental works demonstrated the non-Fickian nature of dispersive processes in heterogeneous porous media from pore to macro scales[102-104] even if the relationship between pore structure, velocity field, and transport is still unclear. In a recent paper, the non-Fickian transport[105] has been numerical simulated for systems as homogeneous bead-packs and more complex geological porous media.

In light of the complex physical phenomena discussed in section 2.1.3.2 for multiphase flow in porous media, mostly due to the peculiar geometric structure, none of the previous mass balance equations allows to describe, as it is, the transport processes that occur in some environmental applications such as groundwater remediation, CO_2 storage in geological formations, and oil recovery from rock reservoirs. In these cases, in fact, there is the need of highly non-linear, strongly coupled, parabolic equations. Thus, model coupling is needed when the processes are described by different sets of equations, for example, in the presence of chemical reactions, i.e. transport of dissolved chemicals and contaminants[106-108], the addition of heat transfer (see the following subsection) and multi-porosity models. The latter occurs when the porous medium consists of two or more distinct structures characterized by significantly different flow properties, as happens in fractured systems, where very fast flow with almost no storage is present in the fractures while there are little or no flow and very large storage capacity in the matrix[109-111].

For the phenomena that occur at the pore scale, the presented mass balance equations (11-16) are not valid any more. At the pore scale, as previously

highlighted, the mass transport is controlled by different forces, such as pressure gradients[112], buoyancy[113], viscous[114] and capillarity[115], and the relative relevance of these forces outlines the flow characteristics in the porous media. Thus, when the fluid that enters the medium (invading fluid) is less viscous than the one that is already present (defending fluid), there is a grown of the viscous fingering instability. The latter determines the formation of invading fluid channels, also called fingers[116-120]. At the contrary, when the invading fluid is as viscous as, or more viscous than the defending one, capillary instabilities can occur, mostly determined by heterogeneity in pore geometries and/or fluid saturation[121]. Since the formation of this kind of channels can affect the macroscopic (Darcy-scale) fluid release, a fractal approach[30, 33] has been widely used. Horvath et al.[122] characterized the surface geometry evolution during immiscible viscous phases displacement, founding that the interface evolution is controlled by dynamic scaling and also that this experimental path are much different from the prediction of a two dimensional model based on partially stable interfaces. Yu and Li[123] developed an unified model to treat fractal characteristic of porous media, being this model able to describe exact or statistically self-similar structures. By using fractal statistical property they also discerned from medium that can be characterized by fractal theory or not. Yu and Chen[124] developed a model for permeability based on the fractal characteristics of pores in the media. The fractal permeability model is found to be a function of the tortuosity fractal dimension, pore area fractal dimension, sizes of particles and clusters, micro-porosity inside clusters, and the effective porosity of a medium. They analytically calculated the pore area fractal dimension by approximating the unit cell by the Sierpinski-type gasket[125-127]. All the fractal dimension involved in the model were calculated by the box counting method[127, 128]. They found agreement between the fractal model prediction of permeability and experimental data.

Mass transport phenomena in porous media have also been widely investigated in experimental works. For example, experiments of flow front

instability either in homogeneous or heterogeneous porous media have been provided, using scaling laws to describe the spacing of fingers and their growth rates[117, 129]. Moreover, nuclear magnetic resonance NMR has been used to measure statistical average of different parameters over a range of spatial and temporal scales, allowing an easy comparison with averaged transport theories[130, 131].

Recently, micro-fluidics has been successfully used to model the pore scale of porous media[112, 132]. The origin of micro-fluidic is found in medicine and biotechnology [133-135], due to the related advantages, as the small sample volume required, the small transport length scales, low cost, precise control over fluid volumes and contact surfaces, increased safety and capacity for high pressures[133]. In the last decades this promising technique has been applied in different areas related to chemical reactions[136, 137] and to energy and fuels[138]. Examples can be found in the manipulation of instabilities in fluid-fluid systems in a Hele-Shaw cell[139-142] and in the diffusion process by using nano- and micro- fibrous media[143, 144], electrospun membranes[144] offering small diffusive resistance thanks to their good breathable properties. On the other hand, a wide range of numerical methods, such as dissipative particle dynamics[145] and lattice Boltzmann[146-148] (LBM) have been used to study pore-scale processes in a multiphase fluid flow environment.

2.2.1.1 Heat Transfer

One of the most common coupling model for porous media is the one between flow and transport of fluid phases and thermal energy. Thus, a balance of internal energy equation has to be solved together with mass balance equations (15-16), as in the following

$$\varphi \frac{\partial(\sum_\alpha \rho_\alpha U_\alpha S_\alpha)}{\partial t} + (1-\varphi)\frac{\partial(\rho_s c_s T)}{\partial t} - \sum_\alpha \nabla \cdot (\rho_\alpha H_\alpha \mathbf{v}_\alpha) +$$

$$-\nabla \cdot (\lambda \nabla T) = q_h \qquad (17)$$

where T is the temperature, U_α and H_α are the internal energy and the enthalpy of the fluid phases respectively, and the density ρ_s, the heat capacity c_s, and the thermal conductivity λ_{pm} are referred to the solid phase. In eq. 18 the Darcy velocity $\mathbf{v}_\alpha$ depends on the pressure p_α, on the saturation S_α via the relative permeability $k_{r\alpha}$, and possibly on the composition of the phases, i.e., on the mass fractions X^k_α, via the viscosity μ_α. Moreover, the density ρ_α depends on the pressure p_α and possibly the phase composition, and the phase enthalpy H_α also depends on the phase composition. On the other hand, the densities ρ_n and the viscosities μ_n can be strongly temperature-dependent.

The heat transfer processes in porous media has been the subject of a number of studies[149-151]. In 90's, a lot of work on the influence of the thermal dispersion effects as well as the inertial effects, the boundary effects and the porosity on the transport processes in porous media has been carried out[152]. The conditions in which the boundary can affect heat transfer have been investigated, founding that it has more importance when the thickness of the thermal boundary layer is comparable or less than the one of the momentum[153]. More recently, both experimental studies and numerical simulation has been performed to investigate heat transfer phenomena at the micro-scale. Examples of the former are measurements of the heat transfer coefficient for different combinations of water and nitrogen flow rates by using a microchannel[154], and the study of the effects of electrical double layer (EDL) on three dimensional heat transfer characteristic and pressure drop of water flow through a rectangular micro-channel are investigated[155].

2.3 Modelling Drying Process in Fabrics

In the study of a drying process, lots of research has been focused on characteristic studies of the textile materials. In the study of their properties in a drying process, cotton fabrics can be treated as porous materials like wood and bricks.[156, 157] The process in the drying of porous media has consisted of two separated periods, i.e. constant drying rate (CDR), so called because of the constant value of the drying rate, and falling drying rate (FDR) period, in which the drying rate decrease gradually until the moisture equilibrium value. A full investigation of a textile material drying process will be given in this section, beginning with an essential investigation in the enhancement of a drying process. As the drying process for porous materials cannot simply be described by linear heat transfer equations, some differential form heat/mass transfer equations[151, 158] and numerical simulation techniques have been proposed to give better modeling results for porous materials[159-163].

2.3.1 Air/water transport phenomena in porous media

Despite of conduction and radiation theories, convective heat transfer principles[164, 165] describe more accurately the characteristics of a hot air drying process, in particular for textile materials. When the hot air is used as the drying medium and blown on fabrics, as it happens also in the dryer, the moisture (liquid phase) in the fabric absorbs energy from impinged air and changes to vapor (gas phase) after gaining enough of thermal energy. The vapor then leaves the fabric structure after the breaking up the internal adhesive force. The reducing of moisture content and increasing of fabric temperature is a complicated heat/mass transfer process. Kowalski[166] has discussed a hot air drying process that can be divided into three periods and labeled as "*Preheating period*", "*Constant drying rate period*" and the "*Falling drying rate period*" as illustrated in Figure 2.4.

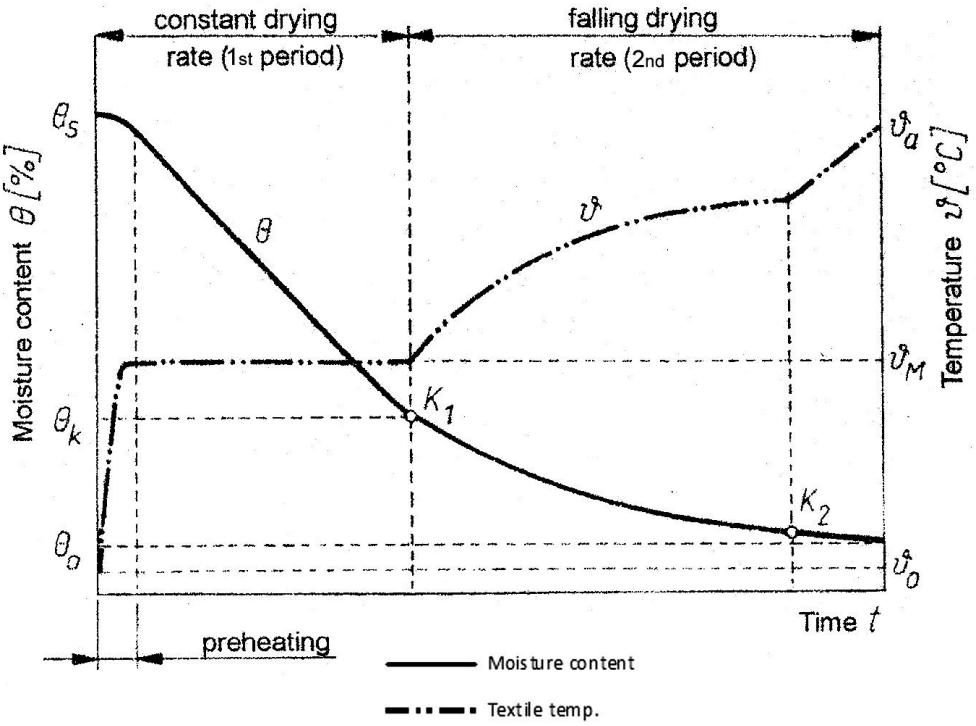

Figure 2.4 Adapted from Kowalski[166].A typical drying curve for porous type materials.

During the preheating period, thermal energy transfers from air to fabric and heats up the fabric surface. The moisture content (θ) reduction rate is low as the temperature is still low because air is not a good thermal conductor. While the fabric absorbs more thermal energy, the moisture content at θ_s on the fabric surface will change to vapor by evaporation. The moisture content reduction keeps at a constant rate at this period as it is just a simple conductive and convective heat transfer process between hot air stream and the moisture on the fabric surface. Water moves from fabric core to surface by capillary action to maintain a balance of the change of the gradient of moisture content. The rate of water transport in the fabric depends upon the environmental conditions, such as air temperature, air velocity and pressure gradient. The rate will also depends upon material properties, such as density, thickness, heat conduction resistance and knitting patterns. Due to the water reduction rate in the process is directly proportional to time, the process is therefore labeled as constant drying rate period. It can be simply

modeled by the linear heat transfer equations that have been well developed[167]. While the residual moisture contents in the fabric drops to the percentage of θ_k, the moisture left in the fabric cannot maintain a totally wet surface to form separated dry/wet regions. In the present of dry/wet regions in the fabric, an osmotic pressure gradient is then developed at boundaries of the dry/wet regions. While the moisture transports from wet to dry region under the osmotic pressure, a mass transport of the moisture is created. The phenomenon of a mass transport in the porous materials under unevenly distribution of the moisture content is called diffusion[168]. The process of diffusion is usually slow in comparison with the convective heat transfer process in the constant drying rate period, thus, a decrease of the moisture reduction rate is observed. The gradually reducing of moisture content from the fabric shows a non-linear behavior after the transition point θ_k, and labeled as falling drying rate period until the reaching of the final moisture content (θ_o). As the porous drying process consists of the linear and non-linear parts, using partial differential mathematics in the assistance of computational fluid dynamics analysis tools could be an effective strategy to construct the modeling equations to present the entire drying process precisely.

2.3.1.1 *Linear Heat Transfer Modeling for CDR Period*

The case of a porous textile dried by an hot air stream can be modeled as a fluid flow under predefined boundary conditions. Moisture in the fabric gains lateral heat from the hot air stream at constant pressure, and changes to vapor until the amount of energy gain is sufficient for the liquid to gas phase change. Moisture diffusion from wet to dry regions starts when a certain amount of moisture left in the fabric is distributed unevenly. Heat exchange characteristics between the hot air stream and moisture can be modeled by linear heat transfer equations under the conventional thermodynamic principles. In this case, moisture in liquid phase completely covers the fabric surface and inner portions to remain in a homogenous condition. The hot air stream flows on the fabric surface to create a dynamic

contact environment. This air-to-water interphase creates an exchange of thermal energy across the fabric surface in presence of a thermal gradient formed between the boundary layer as illustrated in Figure 2.5. The amount of energy exchange from air to water can be simply calculated from linear heat transfer equations; these have been well addressed in thermodynamic textbooks[167]. Equations that describe the convective linear heat transfer process will be reported as follows.

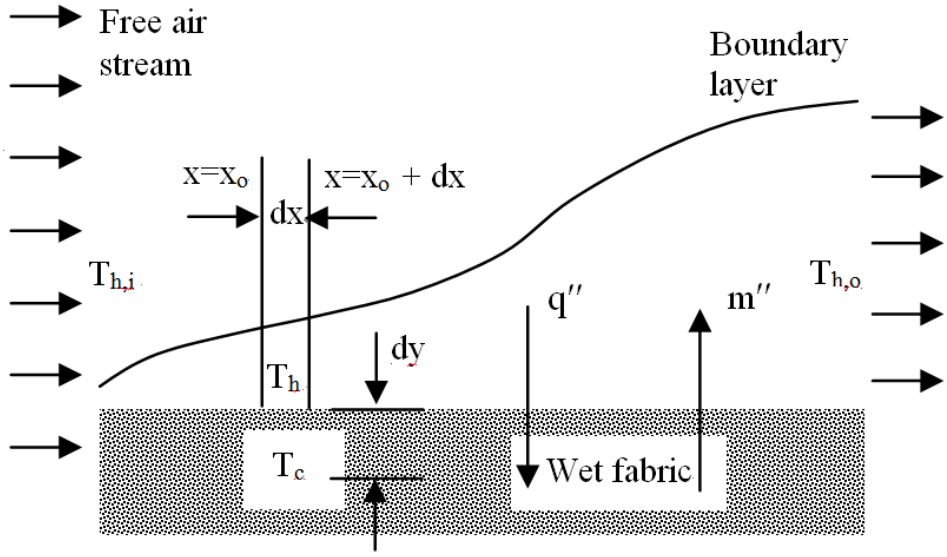

Figure 2.5 Principles of heat transfer under a boundary layer

Fabric drying under constant pressure is an adiabatic process. The heat transfer (q) through the fabric surface (dA) is given as:

$$dq = q''dA = C_h dT_h = C_c dT_c \qquad (18)$$

Being:

C_h = heat capacity of the hot air,

C_c = heat capacity of the moisture,

T_h = hot air temperature in the differential element between x_0 and x_0+dx,

T_c = moisture temperature in the differential element between x_0 and x_0+dx.

In order to apply Equation (18), the following assumptions have to be made:

- The overall heat transfer coefficient is constant and does not vary with location while the temperature difference continuously varies with location;
- The flow condition is steady;
- The specific heats and mass flow rate are constant;
- There is no loss of heat to the surroundings;
- There is no change of phase during the heat transfer; and
- The changes in potential and kinetic energies are negligible.

The amount of heat flow in Equation (18) can be written as:

$$q = \int Cdt = Ch(Th,i - Th,o)x = Cc(Tc,o - Tc,i)y \qquad (19)$$

In a drying process, moisture will evaporate by changing the phase in the gaining of heat from hot air. While the evaporation process does not have the change of temperature, it is an isothermal process and the Equation (19) can be rewritten as:

$$dq/C = dT = 0 \qquad (20)$$

If the heat capacity C in Equation (20) keeps constant for the entire drying process, a linear heat transfer equation deduced from Equation (18) can be given as:

$$dq \; = \; U\,(Th - Tc)local\,dA \; = \; U\,\Delta T\,dA, \qquad (21)$$

where *U* is the overall heat transfer coefficient in term of fabric thickness *dy* as shown in Figure 2.7.

The amount of heat (*q''*) transferred from hot air to moisture in the process can be found by integrating Equation (21) to give:

$$q = \int U\Delta T dA \qquad (22)$$

The overall heat transfer coefficient *U* in [W/m^{2}K] is a measure of the overall ability of a series of conductive and convective barriers to transfer

heat. It takes into account the individual heat transfer coefficients of air stream and moisture, and the resistance of the fabric material. It can be calculated as the reciprocal of the sum of thermal resistances due to conduction and convection process, and written as:

$$\frac{1}{UA} = \sum \frac{1}{hA} + \sum E \tag{23}$$

where h is heat transfer coefficient due to convective heat flow, and R is the resistance to the heat flow in fabric surface due to conduction process. The thermal resistance (R) in [K/W] due to the fabric surface properties is expressed as:

$$R = \frac{x}{k \cdot A} \tag{24}$$

where x is the fabric thickness and k is the fabric thermal conductivity in [W/mK]. In Equation (23), h is the heat transfer coefficient in [W/m^{2}K] and has been further defined by Dittus-Boelter correlation[169] for convective heat transfer process. It is given as:

$$h = k/xNu \tag{25}$$

In Equation (25), the Nusselt number (Nu) can be written as:

$$Nu = 0.023\, Re^{0.8}\, Pr^{n} \tag{26}$$

Re and *Pr* in Equation (26) are the Reynolds and Prandt number, they have been well defined and the values depend upon properties of the air flow in terms of density (ρ), velocity (V), viscosity (μ), heat capacity (c_p) and thermal conductivity (k). In addition, the index n in Equation (26) is 0.4 for heating (contact surface hotter than the bulk fluid) and 0.33 for cooling (contact surface cooler than the bulk fluid). As heat is absorbed by moisture in the fabric drying process due to the air stream temperature (Th) is high than fabric temperature (Tc), n equals to 0.33 is used in Equation (26).

Equation (22) is a linear equation used frequently to present conduction and convection heat transfer process for fluids in turbulent flow. An assumption of no phase change of the working fluid is made for a constant of U in

Equations (22) and (23). It is not true for the studied drying process due to a mass transfer of the moisture contents (*m''*) from fabric to air stream due to an evaporation process occurred. The mass transfer process starts at the transition point. While the residual moisture in the fabric is reduced, the thermal resistance (*R*) in Equations (23) and (24) is changed. On the other hand, thermal properties of air are also changed after the gaining of vaporized water to alter its moisture content. The heat transfer coefficient (*h*) in Equation (25) depends upon thermal conductivity, density, viscosity and heat capacity. All these parameters are sensitive to the change of air-to-water ratio, i.e. moisture content percentage. Therefore, the presented heat transfers Equations (21) and (22) cannot precisely describe the characteristics of the fabric drying process involving the change of the moisture content. Thus, it is necessary to study non-linear models that consider the change of moisture contents in a heat transfer process.

2.3.1.2 Non-linear Modelling for FRD Period

In the carrying out numerical simulations of convective drying of porous materials, the modeling parameters for internal heat and mass transfer characteristics could only be obtained empirically. The parameters co-relate to material structures, such as the pore size and knitting methods, and form a key role in the governing of the entire drying process. These parameters will be determined from experiments in this research because they are not as common as the construction materials, e.g. green bricks[170] that available from engineering data sources. A further investigation of porous material drying characteristics is the using of analytical models to approximate the real drying behavior from the commonly used textile materials. Reye et al.[171] have used Wet surface model to study sludge drying, and Moropoulou et al.[172] have applied First order kinetics model to study the drying of building materials. Although the analytical models could not provide as much information as from numerical simulation results, they can assist the control of a number of operations, such as cycle time predication, calculation of incident moisture contents, and estimation of real-time

conditions in a drying process. A group of analytical models has been developed but not all of them could be directly used to model a porous material drying process precisely. Research scopes in this study are to identify the most suitable models for the drying investigation work.

2.3.2 Modeling Evaporation in Capillary tubes

Drying modeling is classically done threw continuous volume averaged models.[173] In some applications, continuous averaged hypothesis aren't satisfied.[174] Then, discrete approach, like porous network modeling, can be used. They are directly based on the phenomena at the pore scale.[175] Thus, a good knowledge of the evaporation at that scale is fundamental for enhancing those kinds of models.[176] The present hypothesis addresses the evaporation of a liquid from a capillary tube of a circular cross-section, with the perspective of better understanding drying mechanisms in clothes and of improving the drying efficiency. The main idea is to use as a model system of clothes fabrics a capillary tube, which can be regarded as the building block of the complex porous network within a single yarn. This work is based on three distinct concepts, each taking into account different physical phenomena.

To realize these hypothesis a simple model for slow evaporation of a pure liquid from a capillary tube with a circular cross-section were presented, with the perspective of using the results in a porous network model[177]. This model, by assuming local equilibrium between liquid and vapor allows quasi-analytical resolution to predict film and vapor pressure profile. Although highly simplified, the model is useful for some practical cases such as evaporation of water from a capillary in ambient conditions. This model is composed by three distinct approaches, each one considering different physical phenomena.

The first concept concerns the effect of the thin liquid film trapped on the walls: based on literature, we propose that most of drying takes place through such liquid film (rather than in the meniscus region). The second

approach is about thermal gradients inside the capillary tube. Mass and energy transport equation are solved in liquid, gas and solid phase to evaluate the importance of the cooling of the meniscus on the global evaporation rate. The third concept is that such temperature gradients could, in turn, elicit concentration gradients of surface-active agents (by Marangoni effects, see 2.4.2.2), thus reducing the contact angle between the liquid film and the capillary wall. This approach is based on lubrication equation with disjunction pressure modification.[178] The overall effect of these processes could enhance the drying efficiency by surfactant-induced increase of the surface area of the thin liquid film region. In conclusion, this work supports the idea of exploiting surfactants to improve drying efficiency and provides a scientific foundation to investigate their effect on drying rate. The cited approaches gives the following equations:

Evaporation of the film threw the limit layer

$$\dot{m} = -D\frac{p_t - p_d}{L_f} \qquad (28)$$

where m is the evaporation rate, D is the diffusion coefficient, pd is the saturation pressure, pt is the saturation pressure including disjoining pressure effect and Lf the length of the diffusion limit layer [m].

Film cooling due to evaporation

$$\dot{m} = -\frac{\lambda_l}{\Delta H_{vap}}\frac{T_w - T_t}{\delta} \qquad (29)$$

where m is the evaporation rate, λ_l is the latent heat of evaporation, ΔH_{vap} is the enthalpy of evaporation, T_w-T_t is the temperature change between the wall and the center of the capillary tube and δ is the thin film thickness.

Mass balance in the film[178]

$$\dot{m} = -\frac{1}{3\nu_l}\frac{d}{dx}\left(\delta^3\frac{dp_d}{dx}\right) \qquad (30)$$

where m is the evaporation rate, ν_l is the cinematic viscosity of the liquid phase, δ is the thin film thickness and pd is the saturation pressure.

Diffusion in the capillary bulk

$$\dot{m} = -\frac{R}{L}\frac{\partial^2 p_d}{\partial x} \qquad (31)$$

where m is the evaporation rate, R is the perfect gas constant, L is the axial length of the gaseous phase in the capillary, pd is the saturation pressure.

Saturation pressure including disjoining pressure effect[179]

$$p_t = -\frac{M_v p_{sat}}{\Re T_t}\exp\left(\frac{-M_v\left(\frac{A}{\delta^3}+K\exp\left(\frac{l_0-\delta}{l_0}\right)\right)}{\rho_l R T_t}\right) \qquad (32)$$

where pt is the saturation pressure including disjoining pressure, M_v is the molar mass of the vapor, p_{sat} is the saturation pressure, R is the perfect gas constant, T_t is the temperature in the capillary tube, A is the dispersion constant, K and l_0 are constant values. In Figure 2.6 a schematic diagram of the adsorbed thin-film region with thickness δ_0 is shown.

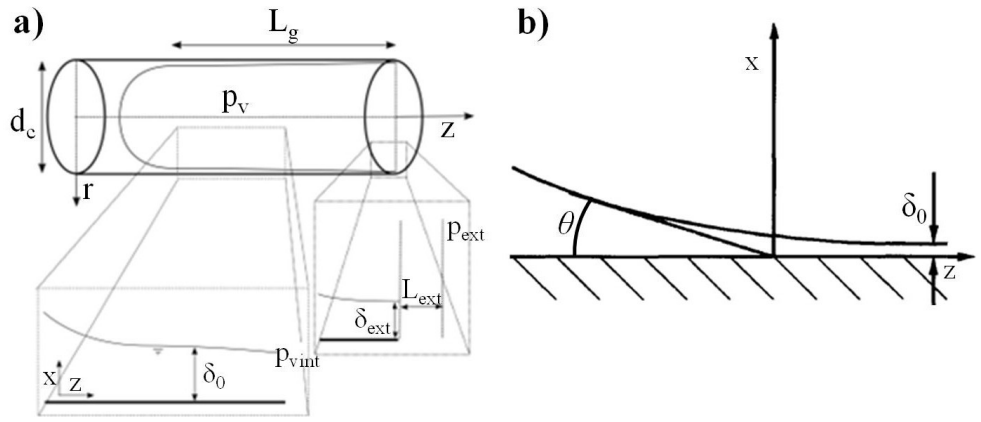

Figure 2.6 a) Lubrication film near the meniscus, inside a capillary tube; b) comparison between "apparent" contact angle and thin film near wall.

The apparent contact angle, Θ_E, is a function of the properties of the liquid, the dispersion constant, and the temperature difference, $T_w - T_t$, between solid and vapour temperature. Taking in account this liquid film, the second concept clarifies the thermal effect in the capillary during drying. In fact, a cooling occurs on all the liquid film and meniscus at the gas-liquid interface

due to evaporation process. Mass transfer in the gas phase is supposed to occur only by diffusion.

2.3.2.1 Marangoni Effect

The surface tension is not in general a spatially constant physical quantity on, say, a liquid-gas interface. Spatial variations in the surface tension may exist and result in additional shear stresses, that is, tractive forces on the adjoin bulk liquid. This gives rise to fluid motions in the bulk liquid. These motions induced by gradients in the surface tension are called Marangoni effects. The spatial variations of σ may arise from variations in different quantities such as the surface temperature, concentrations of surface active additives (surfactants), or in electric charge of surface potentials[180]. An important property of surfactants is that they may have strong effects on the pressure drop necessary to push a bubble through a fine capillary. The influence of electric fields on the surface tension is, e.g., used in pumping devices[181]. As mentioned the surface tension variation along an interface creates a tangential force per unit area, f_s, a tangential stress or shear stress,

$$f_s = \nabla_s \sigma \tag{33}$$

where ∇_s is the surface gradient. Note that the positive sign on $\nabla_s \sigma$ indicates that the liquid on/in the interface will tend to move from areas with low surface tension to areas with high surface tension. On Figure 2.7 areas of high and low surface tension are depicted.

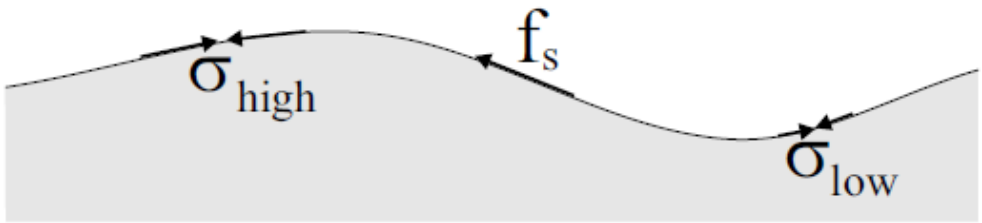

Figure 2.7 Areas of low and high surface tension are illustrated by small and large arrows, respectively. They induce a net tangential stress, the Marangoni effect.

As the surface tension represents the tendency to reduce area there must be a net surface tangential stress from the low to the high surface tension regions.

Newton's third law requires that stress vectors are continuous across boundaries. Both normal and tangential components. Surface tension however gives rise to discontinuous jumps across an interface: The Young-Laplace equation describes the jump in pressure (normal stress), and the Marangoni effects may give rise to jumps in the shear stress (tangential stress) and hence create forces in the bulk liquids.[182]

An idea of the size of temperature-induced Marangoni forces can be given by noting, for example, that cooling a water/air interface from 25 °C to 20 °C will increase the surface tension by 0.8 mJ/m^2 from 72.1 mJ/m^2 to 72.9 mJ/m^2. The shorter a distance over which this temperature gradient is maintained, the stronger the Marangoni force; a sufficiently large effect can be noticed only in micro-systems if compared with other forces. When a surface-active material (a surfactant) is introduced in the bulk liquid the flow in the thin film will cause a non-uniform distribution on the interface. This will in turn create gradients in the surface tension and hence surface shear stresses. The surfactant dramatically increases the shear stress in the film (it is not anymore zero on the interface). It has been demonstrated that the introduction of surface active materials dramatically increases the pressure at the water/air interphase[183]. The pressures can be from two to four orders of magnitude larger than those in the absence of surfactant.[180]

The Marangoni force can be used as a micro-scale propulsion system, as some bacteria actually do in nature, using a simple principle: as the interface tries to minimize the region of high surface tension in absence of surfactants while maximizing the region of low surface tension in presence surfactants, emitting surfactants that lowers the surface tension gives to the emitting body a propulsion.

Now considering the possibility to change the contact angle between solid and liquid phase using a surfactant, the effect on the drying rate could be explained considering the two concept illustrated before: first of all, a decrease of the contact angle involves an increase of the liquid film region.

As it's said before, the liquid on the film region evaporates faster than the liquid on the meniscus region; so, a larger film region means a faster evaporation. On the other hand, the cooling of gas-liquid interface at the meniscus creates a temperature gradient that concentrates the surfactants (by Marangoni effects) in the interfacial region, which is where it should belong to increase the evaporation.

Experimental results can be fitted with this model by measuring all the parameters needed in the set of equation showed before. Most of these parameters, like the capillary radius R, are chosen in the experimental set-up or can be found in literature, like liquid properties. The drying rate can be measured by optical microscopy, monitoring the receding of the meniscus in time. The film thickness $\boldsymbol{\delta}$ can be measured directly by some optical technique (e.g., interferometry). The temperature difference $T_w - T_t$ can be monitored during evaporation by thermocouples or, indirectly, by thermal analysis with a TAM (Temperature Analysis Monitor) instrument. With the same thermo-analytical procedure also the vaporization latent heat ΔH_{vap} and the thermal conductivity λ_l of the liquid can be measured. Other quantities to be determined include the apparent contact angle and the interfacial tension.

3 EXPERIMENTAL SECTION

"One world, one experiment"
Carl McDaniel and John Gowd [184]

After an exhaustive discussion on the aim of this work and on the literature produced so far on this topic, here is the main core of this thesis. In this chapter, materials, experimental apparatus and procedures used in data analysis are illustrated in details. The main experimental results will be presented in the next chapter.

3.1 Materials

3.1.1 Aqueous Solution

3.1.1.1 Hard Water

In the experiments, water solutions with different hardness have been tested. We started with demineralized (DEMI) water (which is commonly used in ironing to prevent the formation of calcium aggregates and in electrical batteries). All other solutions used in our experiments were prepared using the same sample of DEMI water. To prepare water solutions at different hardness salts of calcium and magnesium hydrates to be dissolved in DEMI water were weighted by a precision balance. Depending on the dissolved salts quantity, solutions having different hardness are obtained. In the table 3.1 the solutions realized and their characteristics were summed up.

Water Hardness	**Concentration**	**Salts [mg/dl]**	**Salts [mg/250ml]**
Moderately Hard	2,5 mmol/l 250 ppm	27,57 $CaCl_2 * 2H_2O$ 12,71$MgCl_2 * 6H_2O$	689,16 $CaCl_2 * 2H_2O$ 317,66 $MgCl_2 * 6H_2O$
City Water	2,6 mmol/l 260 ppm	28,67 $CaCl_2 * 2H_2O$ 13,21$MgCl_2 * 6H_2O$	716,82 $CaCl_2 * 2H_2O$ 330,36 $MgCl_2 * 6H_2O$
Hard	4,2 mmol/l 420 ppm	46,31 $CaCl_2 * 2H_2O$ 21,35$MgCl_2 * 6H_2O$	1157,7 $CaCl_2 * 2H_2O$ 533,66 $MgCl_2 * 6H_2O$
Very Hard	5,4 mmol/l 540 ppm	57,34 $CaCl_2 * 2H_2O$ 26,43$MgCl_2 * 6H_2O$	1433,4 $CaCl_2 * 2H_2O$ 660,73 $MgCl_2 * 6H_2O$

For some of these solutions accurate characterizations were also done to better understand the contribution of electrolytic parameters to the drying process (see table 3.2).

Table 3.2: PH characterization of water solutions

Water Hardness	**PH**	**Temperature (°C)**	**Conductivity (µS/m)**	**Potential Difference (mV)**
Demineralized Water	5.52	27	5366	94.2
Moderately Hard Water	5.86	27	5300	74.5
Hard Water	5.81	27	6860	77

3.1.1.2 Surfactants

In aqueous solution surfactants self-assemble into a range of well-defined structures, due to their amphiphilic nature; the structure growth mainly depends on surfactant nature and concentration and on temperature.[185, 186] In particular, an almost spherical multilamellar structure consisting of onion-like stacked bilayers separated by solvent were shown, at rest, by surfactant vesicles. The rheological behavior of multilamellar vesicles (MLV) were studied in different flow conditions in order to characterize their properties for several applications, such as biomembrane models[187] or carriers for drug delivery[188]. In particular the deformation of unilamellar vesicle and capsules under capillary flow were deeply investigated.[189, 190] Due to the analogy between MLV and biomembranes structure, [191-193] the study of MLV dynamics in capillary flow is often cited as a model for blood flow in microcirculation.[134, 194-198] In linear flow multilamellar vesicles mimic the complex deformation of white blood cells.[199, 200] The similarity in confined flow is so close that cluster of red blood cells[193, 201] present the same hydrodynamic interactions of vesicles clusters.[190, 202, 203]

Recently,[204, 205] were showed that MLVs of linear alkylbenzenesulfonic acid (HLAS) deform at a constant volume under flow with different dynamic regimes tumbling, breathing and tank-treading[188, 206, 207]. Furthermore, a scaling analysis based on the definition of a capillary number were carried out in analogy with emulsion droplets[208] and a possible mechanism of the deformation of MLVs were proposed based on the experimental data of vesicles deformation acquired by confocal microscopy at rest and in polarized light under flow.[205] The dynamic behavior of an HLAS solution were considered also under capillary flow, performing as a power law viscosity fluid. Moreover the MLVs concentration gradient in the micro-capillary section and its relation with flow velocity were pointed out; in fact the wide of the vesicle concentrated region scale with the product between the velocity and the micro-capillary diameter. If the influence of surfactant structures like MLV on interfacial phenomena are well known, very few reports exist in the literature about the influence that these structures have on evaporation rate. Rate of evaporation of water droplet depends on several key factors like relative humidity, temperature, additives such as surfactant, electrolytes, etc.[209] The drying mechanisms of surfactant solutions were documented by gravimetrically monitoring the water loss in air and at controlled relative humidity. Alexandridis et al.[210] monitored the water loss of an alkyl-propoxy-ethoxylate surfactant aqueous solution films exposed to air of constant relative humidity until the equilibrium was reached; results shows the rate of water loss depends on some parameters such as the air relative humidity, microstructure in the surfactant film, and the attractive interaction between the head group and water molecules at the interface. Doganci et al[211] successfully prepared liquid marbles by encapsulating graphite micropowder on aqueous sodium dodecyl sulphate (SDS) droplets and determined their total evaporation rate and buckling periods in a closed chamber having constant relative humidity and temperature. The evaporation rates of graphite liquid marbles obtained from different concentration of SDS droplets and the results compared with the graphite

liquid marbles from pure water. Dandan et al.[211] studied the effect of SDS anionic surfactant concentration on the diffusion-controlled evaporation rate of aqueous solution drops placed on TEFLON–FEP substrate with different concentrations. Rodríguez et al.[212] successfully studied the evaporation behavior of solutions of an amphiphilic polymer, phosphonated polybutadiene in toluene and in water the vapor pressure and evaporation rate measurements. The polymer reduces the vapor pressure and evaporation rate of toluene, while the opposite effect was observed in aqueous solutions. Thus, it can be concluded that the evaporation rate is totally depends on the relative humidity, temperature, and the presence of additives such as surfactants and polymer molecules and so on. Normally, at the higher relative humidity (RH) as the water vapor percent in the environment is high so evaporation rate successively decreases; instead, because of the tight binding of surface water molecules through electrostatic force with head groups of monomer surfactant molecules, in the presence of surfactants the evaporation rate increases.

The surfactant used in this work is the commercial anionic surfactant Sodium linear alkylbenzenesulfonate (Na-LAS). In **Errore. L'origine riferimento non è stata trovata.** the chemical structure of the Na-LAS molecule is shown. The benzene ring linking a sulphonic acid group (hydrophilic head) and a linear alkyl group (hydrophobic tail) are shown.

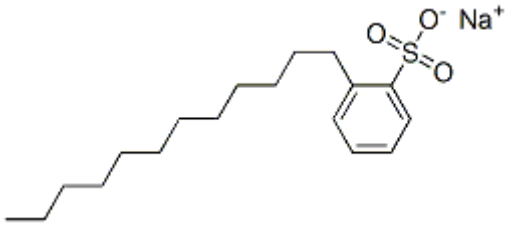

Figure 3.1 Na-LAS chemical structure.

Na-LAS have a Critical Micellar Concentration in pure water equal to 450 ppm; the phase diagram of Na-LAS – water solution shows three different

regions depending on surfactant concentration and temperature as shown in **Errore. L'origine riferimento non è stata trovata.**, where the grey area represents the range of interest in this work.

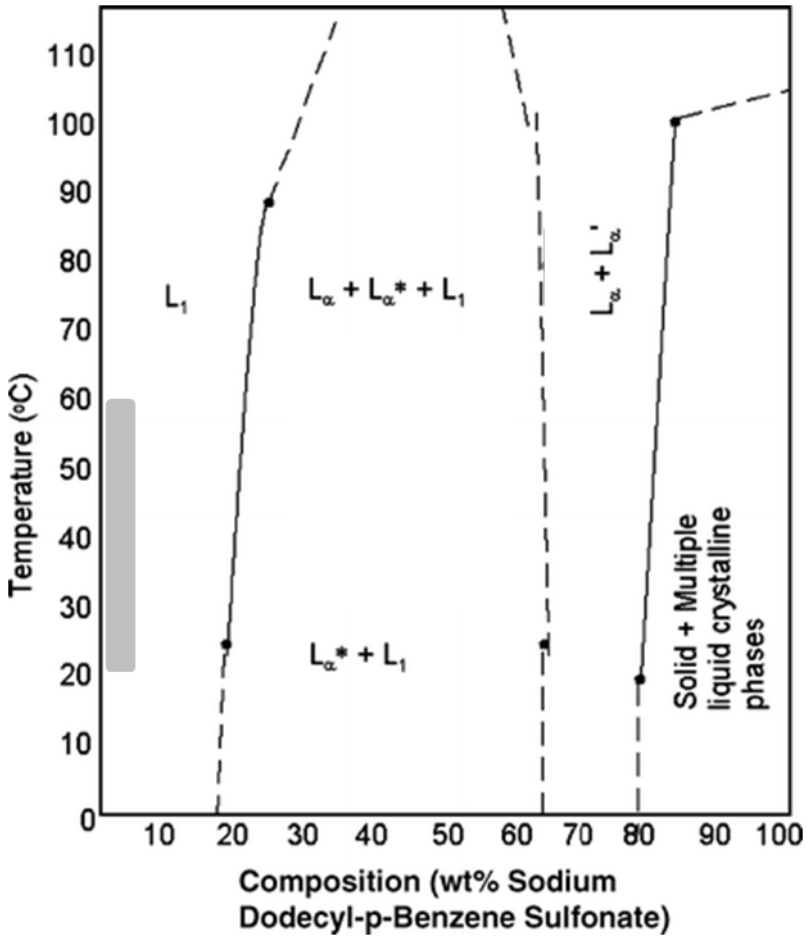

Figure 3.2 Phase diagram of the Na-LAS/water system, adapted from Richards et al.[43] A micellar solution is observed at low concentrations (L_1). Next is a multi-phase region where two or more lamellar phases (L_α) co-exist with a micellar solution. In this region L'_α is used to denote the appearance of two or more L_α phases. $L_\alpha*$ indicates a situation whereby multiple L_α phases coexist with L_1. In the concentrated region, solid and multiple liquid crystalline phases co-exist.[44]

Regarding temperature, all the observations were done at room temperature (≈25° C) and at ≈40°C, trying to simulate a common dryer inner environment. At these temperatures, the diagram shows that for diluted Na-LAS concentration (< 5% wt.) only the isotropic micellar L_1 phase is present, while the lamellar L_α phase is the only one present at the highest concentration (> 67% wt.). The solutions utilized in the experiments were prepared using deionized water (pH 5.52) and Na-LAS surfactant (Sigma-

Aldrich product) and have different concentrations (see following table) lower than 5% wt; a characterization of these solutions was carried out using instruments for the measurement of pH and conductivity. Measurements after a calibration with a solution at pH 4 gave the results reported in table 3.3; as can be notices, conductivity increases with surfactant concentration, as expected.

Table 3.3: Na-LAS concentration and PH characterization of diluted surfactant solutions

Na-LAS/Water		***Conductivity***	***pH***
[ppm]	**[%wt]**	**[µS/m]**	
0	0	19.39	5.52
250	0.025	108	2.98
500	0.05	162.6	2.74
1000	0.1	325.5	2.61
2000	0.2	483.1	2.26
5000	0.5	1025	/
10000	1	1274	/
20000	2	4234	/
50000	5	10430	/

3.1.2 Cotton Fabrics

Cotton is the most common textile material, frequently used in clothes making; it is light, soft, and has a high water absorption value. Its special properties make cotton widely used for clothes making, and mixed with other textile materials to form artificial fibers. Thus, a great majority of fabric materials used in the tests were made of cotton fibers.[45]

The fabrics used in experiments are both 100% white cotton; one is a common cotton fabric with a simple thin structure, taken out from a cloth, and the other is a standard cotton provided by P&G. These two samples have different knitting and specific weight, but same porosity (0.7). Cotton main properties are resumed in table 3.4.

Table 3.4: Cotton fabrics main characteristics

Description	Width (cm)	Area Weight (g/m^2)	Weave	Yarn Count (dtex)
Common Cotton	100	70	plain	170/170
Standard Cotton	100	170	twill	295/295

3.1.3 Capillary tubes

During the drying processes in porous media different transport mechanisms are involved, as discussed in chapter 2. The vapor diffusion in the pores is regulated by Fick's law, where vapor diffusivity depends on the tortuosity of the pores. The transport of gas generated by pressure gradients follows the Darcy's law. Another possible mechanism which has recently aroused interest is the flow of liquid along the edges of a pore with a rectangular section, whose geometry contributes to increase the drying rate compared to capillaries with circular cross section.[15, 16] The increase in the speed of drying found in a cell filled with a high density of silica spheres with respect to the case of an empty cell of equal volume is also attributed to the same effect.[17, 216] The diffusive flow of steam can increase[217] due to the presence of mechanisms of condensation/evaporation through remote areas of liquid, which entails a lowering of the vapor pressure (dependent on the curvature in accordance with the Kelvin equation), although so far has not been given any direct experimental evidence. Many theoretical and experimental approach for the porous media modeling were evaluated. Because of the complexity of its pore network, a porous medium is a heterogeneous system. Furthermore, porous media are really different from each other, so it is difficult to think about an approach that can be valid for anyone. Following the experimental approach of Metzger et al. (2010)[48], the complex structure of the cotton fabric was simplified with a mimicking structure composed by

a number of interconnected capillary tubes (lattice model), where the drying process is mainly influenced by the geometrical shape and connection of each pore, as showed in **Figure 3.3**.

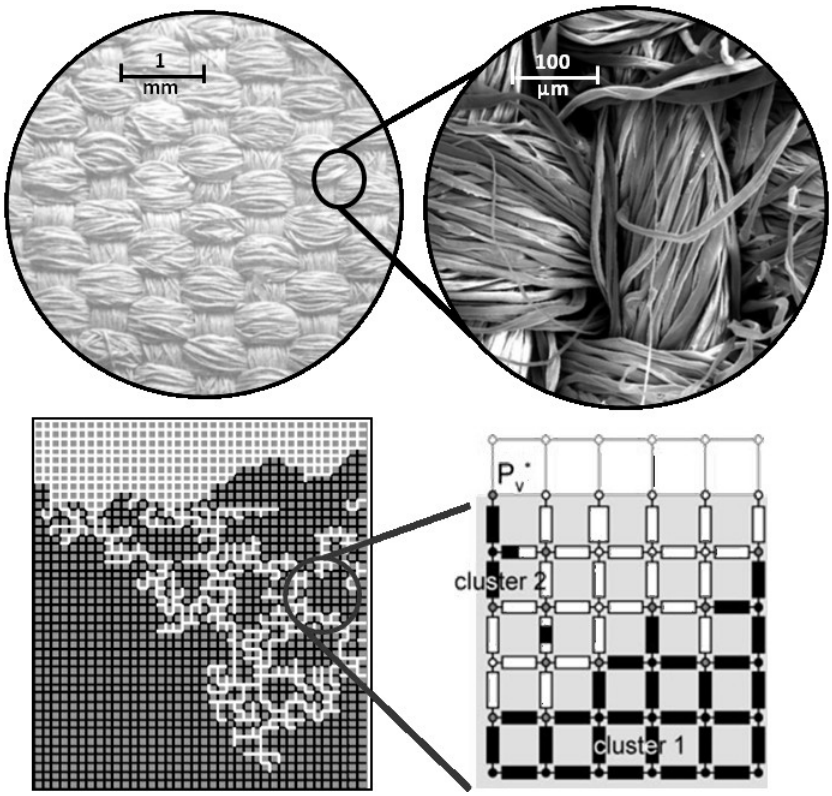

Figure 3.3 The complex structure of a cotton fabric, in the upper part, were compared with a lattice model, in the lower part.

To understand the driving forces of a such complex structure, the porous network were simplified and a single pore system was identified as the constitutive element of the whole structure. The capillary tubes used in this work are made by fused silica which in its simplest form is silicon dioxide SiO_2, formed by a chemical reaction between silicon and oxygen.

A schematic of capillary tube is shown in Figure 3.4.

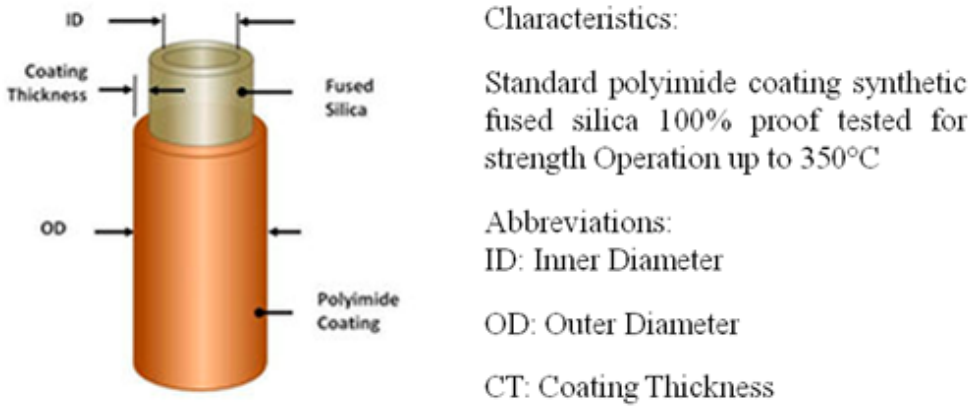

Figure 3.4 Typical schematics of a capillary tube.

The capillaries used in experiments present the following technical details:

Table 3.5: Characteristics of Capillary Tubes

	Capillary Tube 100 µm					***Capillary Tube 50 µm***					***Capillary Tube 10 µm***				
	ID	**Err**	**OD**	**Err**	**CT**	**ID**	**Err**	**OD**	**Err**	**CT**	**ID**	**Err**	**OD**	**Err**	**CT**
	µm	µm	µm	µm	µm	µm	µm	µm	µm	µm	µm	µm	µm	µm	µm
Nominal	100	4	363	10	20	50	3	150	6	12	10	2	150	6	12
Beginning	99		360		18	49		150		11	11		150		12
End	99		364		19	50		150		11	9		147		12

:

3.2 Methods

3.2.1 Gravimetric Analysis

3.2.1.1 Analytic Balance

Some experiments were performed to measure the rate of drying of aqueous solutions in a cotton fabric placed in a Petri dish (Ø = 35 mm). The results were compared with the drying rate of the same amount of water placed in a Petri dish having the same apparent surface area (Figure 3.5).

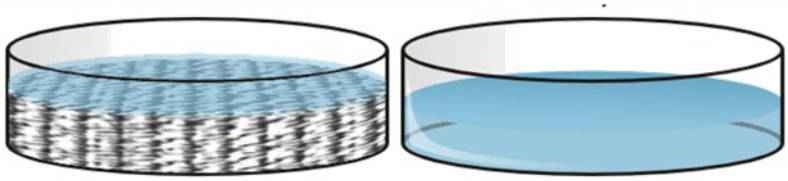

Figure 3.5 Scheme of the two Petri dishes compared.

The experiments were carried out in pairs using two analytical balance, in order to measure the drying rate of the two samples under the same conditions of temperature and relative humidity (RH). The balances (Ohaus Explorer Pro model EP214C) have a precision of four decimal places and a capacity of reading from 0.1 mg to 10 μg; they present an integrated draft shield enclosure. The enclosure is required due to the extreme sensitivity of the instrument. Two hygrometers were used to measure temperature humidity inside the balance enclosure. The first operation of the experimental procedure consists in measuring the empty Petri dish weight; then the dry weight of the cotton fabric samples was measured in order to calculate the Remaining Moisture Content (RMC), which is given by water weight divided by fabric weight. Finally, the same amount of solution was poured each Petri dish, paying attention that the surface of the plate without the cotton fabric was completely wet. The experimental apparatus is shown in Figure 3.6.

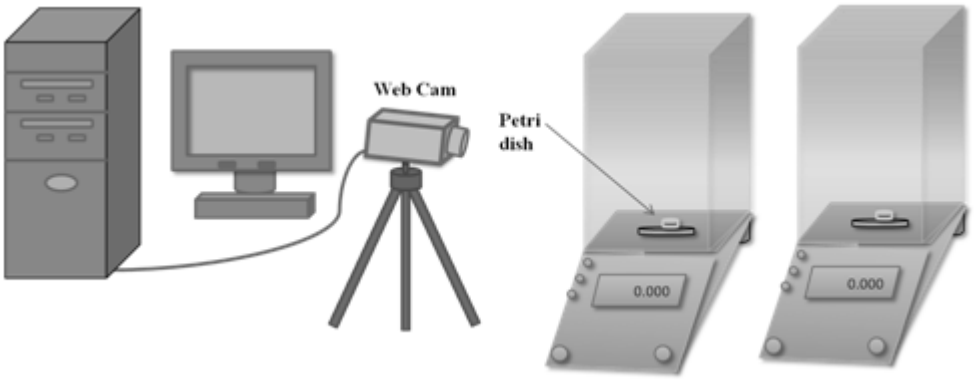

Figure 3.6 Schematics of the experimental apparatus for thermo-gravimetric analysis.

A computer was connected to a webcam in order to monitor the progressive decrease in weight measured by the scales. A program, WebCamImageSave, allows to capture images in time with a defined interval. In our case, given the duration of the experiments, it was decided to take a picture every two minutes. The acquired image were manually converted into values so in Excel were reported the weight change over time, at the end of the evaporation process. The apparatus illustrated so far were built to bypass a simple problem: analytic balances work at equilibrium and allow to print values only under stable conditions, whereas drying is a non-equilibrium process.[49]

From the data acquired, the drying curve in terms of water saturation and RMC and the time derivative of the weight loss over time were calculated. The saturation were expressed as the ratio between the instantaneous weight of the solution and the initial weight of the solution; it follows that this value changes in the range [0,1]. The RMC (Remaining Moisture Content) is expressed as the ratio between the weight of the solution and the dry weight of cotton fabrics, expressed in percentage. The derivatives are calculated point by point as the change in weight over a time interval, divided by that time.

3.2.1.2 Dynamic Vapour Sorption

Dynamic vapor sorption (DVS) is a gravimetric technique that measures how quickly and how much of a solvent is absorbed by a sample: such as a dry powder absorbing water. It does this by varying the vapor concentration surrounding the sample and measuring the change in mass which this produces. Water vapor is most commonly used, but it is also possible to use a wide range of organic solvents. DVS was originally developed to replace the time and labor-intensive desiccators and saturated salt solutions to measure water vapor sorption isotherms.

The main application of DVS is to measure water sorption isotherms. In general, a vapor sorption isotherm shows the equilibrium amount of vapor sorbed as a function of steady state relative vapor pressure at a constant temperature. For water sorption isotherms, water relative vapor pressure is more commonly expressed as relative humidity (RH). In a DVS experiment a sample is exposed to a series of step changes in relative humidity and the mass change as a function of time were monitored. The sample mass must reach gravimetric equilibrium at each step before progressing to the next humidity level. Then, the equilibrium mass values at each relative humidity step are used to generate the isotherm. Isotherms are typically divided into two components: sorption for increasing humidity steps and desorption for decreasing humidity steps. Sorption can be further divided into adsorption (sorbate located on the surface) and absorption (sorbate penetrates the bulk).

3.2.2 Thermal Activity Monitor

Thermal activity monitor III (TAM III) is a micro-isothermal calorimeter that can test thermal behavior under various storage temperatures; here was used to calculate the latent heat of evaporation of the porous media. All sample set-up and data acquisition steps are performed by a devoted software package, TAM III Assistant™, which can also perform most common types of data analyses.

In the isothermal mode, the high level of control enables both long and short-term experiments to be performed with excellent baseline stability.[220] The scanning mode operates a linear ramp of temperature with time. Because the instrument records data continuously, also during the temperature change, phase transitions or other temperature-dependent effects will be detected. Since measurement is continuous, there are no breaks in the data collected. All samples were prepared within a dry-bag that was filled with dry nitrogen, and a humidity detector was used to control relative humidity.

3.2.3 Microscopy Techniques

3.2.3.1 Confocal Microscopy

A confocal laser scanning microscope (CLSM) is an imaging instrument in which a specimen is illuminated with a focused light spot. A light beam passes through a light source aperture and then is focused by an objective lens into a small focal volume within a specimen. A mixture of emitted as well as reflected light from the illuminated spot is then recollected by the objective lens. A beam splitter separates the light mixture and reflecting the light into the detection apparatus. After passing a pinhole, the light is detected by a photo-detection device, transforming the light signal into an electrical one that is recorded. The detector aperture obstructs the light that is not coming from the focal point, resulting in sharper images than those from conventional light microscopy techniques. Background information on the general field of CLSM is presented in detail in several sources.[51-54] To summarize, a confocal arrangement isolates information from volume elements without the necessity of physical sectioning.

An investigation of the internal structure of cotton fabrics was performed by the LSCM technique. A fluorescent marker (Rhodamine-B , 1 μg/ml) was used to make a 3D reconstruction of the tissue structure using a commercial software of image analysis software package (*Image Pro Plus 7*). Another dye at low concentration (Fluorescein isothiocyanate, 0.01%wt), in order to

not modify the constitutive properties of the liquid phase, was used to highlight the liquid film that lay on fabrics. The confocal microscope was a Zeiss LSM 5 PASCAL. It's made by the transmitted light microscope Axiovert 200 M equipped with a high resolution digital camera AxioCam, a high magnification optics (40x, 63x) was used. The module of the laser comprises a first Ar laser emitting at three different wavelengths (458, 488, 514 nm) and a second HeNe laser emitting at a wavelength of 543 nm. The scanning module comprises a confocal pinhole with a variable diameter and a channel equipped with high sensitivity PhotoMultiplier Tubes (PMT) for the detection of the signal. There is also an additional channel for detecting the transmitted light.

3.2.3.2 Time-Lapse Microscopy

The microscopy workstation used to run the experiments comprises an inverted optical microscope (Zeiss Axiovert 200), mounted on an anti-vibration table, with a 5x objective (Carl Zeiss CP Achromat PH1). The microscope is provided with a table and a focusing system both equipped with stepper motors, which allow to remotely select a field of view within the sample under examination. Images were acquired using a monochrome CCD camera (Hamamatsu Orca AG) and sent to a personal computer via Firewire interface. The digital image is made up of a matrix of 1344x1024 pixels. The value of each pixel, between 0 and 255, is equivalent to the brightness of the corresponding image point . The microscope is placed inside a "home-made" incubator with Lexan plates, with a radiator and a fan to improve heat exchange and maintain constant temperature. The temperature inside the incubator is monitored by a thermocouple and the adjustment is made by software using a PID controller (proportional - integrative - derivative). The microscope table is equipped with a box in which the microclimate is controlled by means of an air stream fed to a bubbler (Figure 3.7).

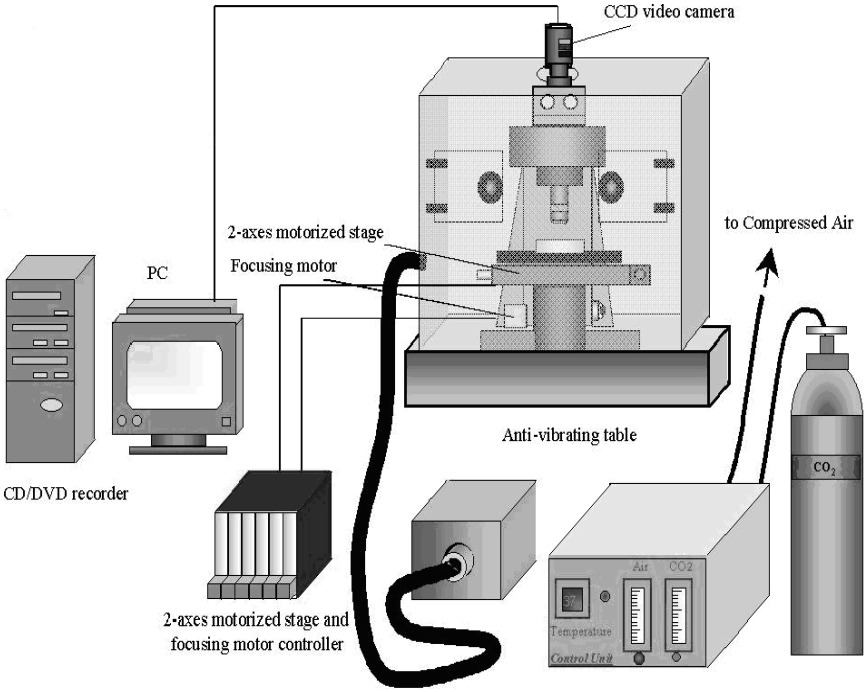

Figure 3.7 Schematics of the Time Lapse microscopy apparatus.

The entire workstation is controlled by a controller (ObjectiveImaging) via computer through a time-lapse software that runs on Labview. Such software allows you to scan periodically predetermined areas of one or more samples. The fields of view to be scanned are manually selected using an electronic joystick and the time interval between two consecutive scans is an input parameter.

Once started, the program stores the coordinates of the selected fields of view and controls the motorized table so as to bring each selected region in the field of view of the microscope, capturing and storing the corresponding image. At the end of each scan, the program pauses until the next iteration. Scanned images are saved on the hard disk in separate directories for each selected region. At the end of the experiment for each field of view the recorded images can be merged in a video that allows to observe the qualitative evolution of the sample over time.

3.2.4 Image analysis

The study of the parameters relating to the drying of liquid in a capillary tube has been carried out on the images acquired in real time from the camera and transferred to the computer in digital format using the commercial software Image Pro Plus 6. The analysis of the acquired images consists in the determination of certain geometrical quantities of the meniscus in time. The analysis process of the image sequences can be divided in the following way:

1. Acquisition of single images.
2. Evaluation of the meniscus shifting
3. Evaluation of the contact angle

During the analysis many difficulties have been encountered. A problem regards the issue of the calibration of the microscope. In fact, the program Image Pro Plus requires the calibration factor μm/pixels that converts the measurements made in pixels in quantities expressed in microns. The factor μm/pixel depends on the objective and the microscope used. Generally, proceeding to the analysis directly on the program by setting the calibration, the values come out in microns; the risk is that, in case of a mistake with the optics, there is no possibility to correct the values and a repeat of the measure is needed. In order to avoid this risk, the values were processed directly in pixels and, after that, multiplied by the conversion factor. Another source of error is the contact angle evaluation; the methods used require a manual analysis. Often manual analysis proved to be more accurate and therefore preferable, while other times has been less necessary. For this reason, several approach were applied to minimize observer's influence on the contact angle evaluation process. Beyond the technical problems related to the proper use of the software, the real obstacles are the experimental ones. Some common problems are:

Uncertainty in defining meniscus contours: due to a poor focus of the images or the absence of immersion oil for microscopy. In these cases we resort to common sense and we considered a contour line intermediate.

Light Distortion effect: this is a problem caused by the capillary tube curvature and translates in the presence of a dark band near the inner capillary wall. This effect can damage the analysis because it alters the perception that one has of the meniscus contour.

3.2.4.1 Meniscus Displacement

The images captured in time-lapse microscopy were processed and analyzed in order to calculate the rate of drying of the solution contained in a capillary. The analysis is performed using *Image-Pro Plus*, *Excel* and *Sigma-Plot*. For the evaluation of the drying rate, we used the images obtained by time-lapse and two softwares, an image analysis one (image pro plus) and Excel for data reduction. The time lapse gives a series of images, as reported in Figure 3.8.

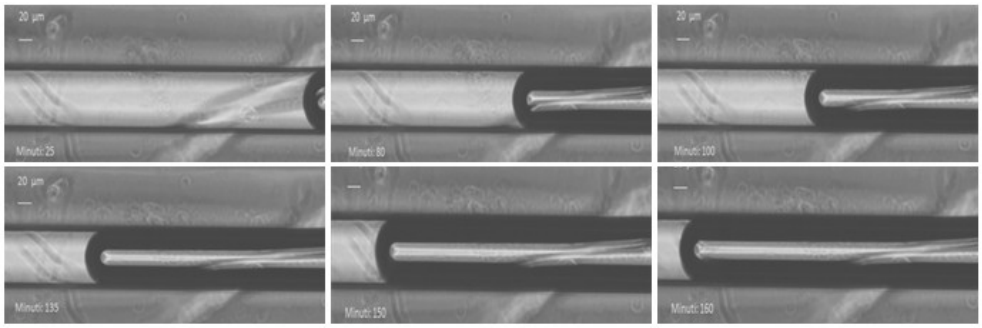

Figure 3.8 Water evaporates over time in a 100 µm capillary tube.

The sequence of frames is imported into *Image-Pro Plus*, which through a special function shall connect together the various images to show the sequence of photos as a video. Then, the meniscus center were taken as a reference and its shifting along the x axis with time were followed (Figure 3.9).

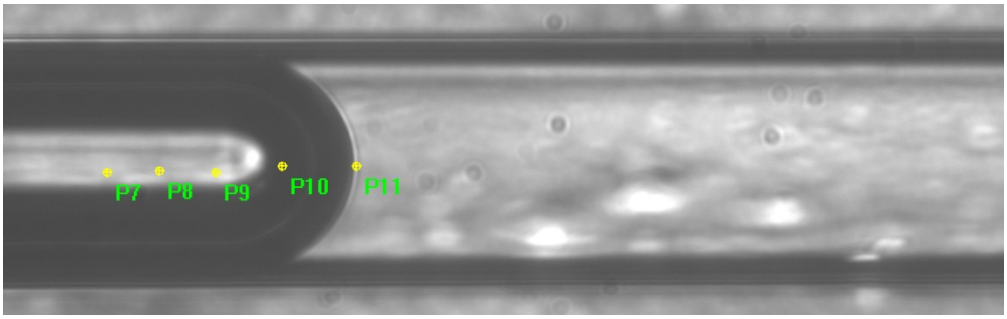

Figure 3.9 Analysis of meniscus shifting.

The program output gives the x, y coordinates of the points Pi in pixels that, multiplied by the appropriate conversion factor (summarized in table 3.5), depends on the magnification used, transforming the values in microns scale.

Table 3.6: Conversion factor for the optical magnification used

	Conversion factor pxl\µm
10x CP - ACHROMAT	0.613(2)
20x LD A - Plan Ph1	0.304(6)
5x EC Plan - NEOFLUAR Ph1	1.210(8)

The coordinates of the points Pi x against time in seconds relative to the frame analyzed are reported in an excel file. The sequence of the times it comes from a time lapse that in addition to the images were recorded in a text file and provides the time sequence expressed in seconds. A sequence of points more or less linear is obtained; the best curve passing through the experimental points were obtained using the regression technique. A method to derive the curve that best approximates the data trend is to apply the method of least squares. This technique is based on the principle that the best-model curve which interpolates the experimental data, is the one for which the relationship applies:

$$\sum_{i=1}^{n} w_i * (y_i - y_l)^2 = minimum \qquad (34)$$

where w_i are said weights of the experimental data (take account of the greater or lesser uncertainty with which the experimental data themselves are known), and (y_i - y_l) is the difference between the experimental values y_i and those calculated y_l. In our case, by applying the technique of simple linear regression a straight line of equation is obtained.

$$y=ax + b \qquad (35)$$

where *a* and *b* are coefficients that represent, respectively, the intercept and the slope of the line. The slope of the line corresponding to the angular coefficient provides the value of the drying rate expressed in µm\s. In **Figure 3.10** the speed of drying of demineralized water at a temperature of 38 °C and for a capillary of 100 µm equal to 0,1472 µm/s is shown.

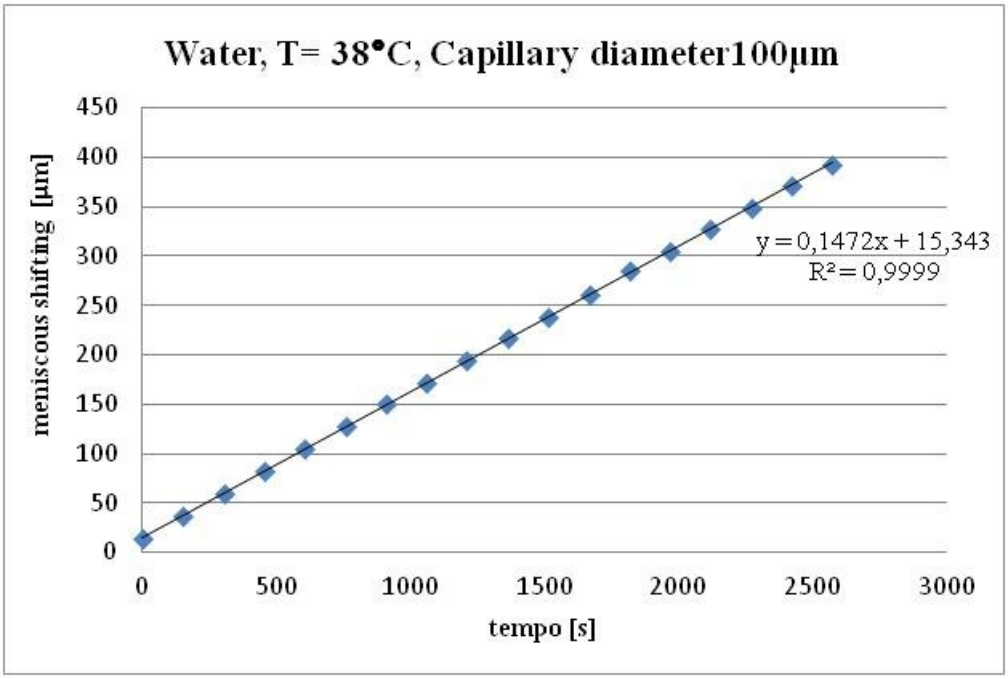

Figure 3.10 Example of a drying curve of DEMI water solution in a 100 µm capillary tube.

It was also used another function of *Image Pro Plus* that allows the reconstruction of the whole capillary by connecting consecutive images to measure the void degree (L), defined as the distance between the open side of the tube and the meniscus position at a defined time.

In this way, the images were placed side by side and shifted until they match together, as shown in Figure 3.11. In order to properly rebuilt the capillary, the imperfections on the image were taken as a reference.

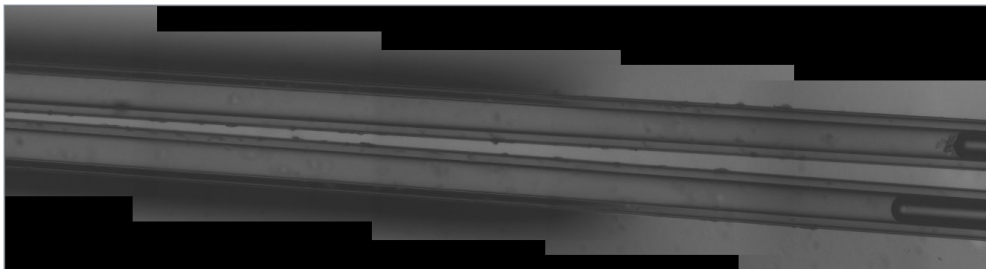

Figure 3.11 Two capillary tubes (100 μm) containing DEMI water.

This operation is repeated for all the images that show the receding of the meniscus in order to make a reconstruction of the evaporation in the whole capillary.

3.2.4.2 Contact Angle Evaluation

The evaluation of the contact angle through experimental procedures turns out to be quite complex, in fact we have not come immediately to a method that will provide us with values comparable with those reported in the literature. The first two methods used initially were subjected to a large error in measurement of the contact angle, giving values very different from those reported in the literature. The third method is the one that we used and that is what gives us the best results, it is also reproducible and presents measurement errors is limited.

First method

The upper and lower contact angle measurement is performed by the software "Image Pro Plus". This measurement is carried out using the tools available in the software library but it is a measure that is affected by a high degree of error because the operator has to manually evaluate the angle. In Figure 3.12 the measure found is 45°.

Upper and lower contact angle have the same measure, but the resulting value is far from the one of 33° reported in literature.[225] In addiction, this kind of measurement is strongly operator-dependent.

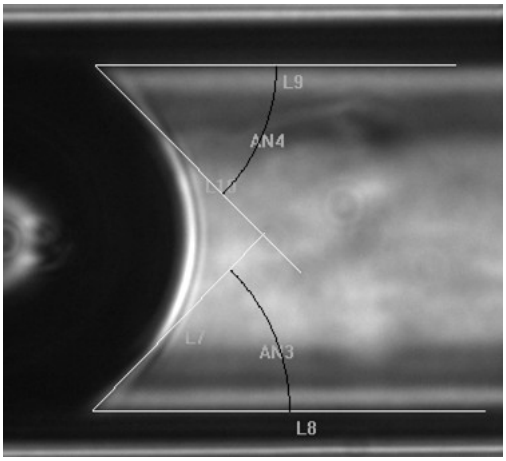

Figure 3.12 Picture of meniscus in a capillary tube taken in time lapse and analyzed in image pro plus.

Second method

This method requires a combined use of two softwares, Image Pro Plus and Excel. With Image Pro Plus the meniscus contour were evaluated (Figure 3.13).

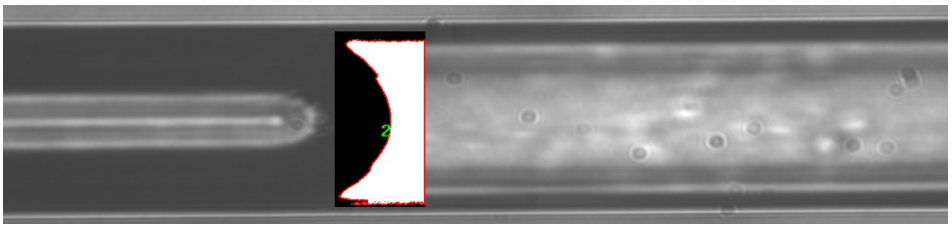

Figure 3.13 Meniscus discretization.

The coordinates of these points in a text file and we import into excel by constructing the profile of the contour as shown in Figure 3.14.

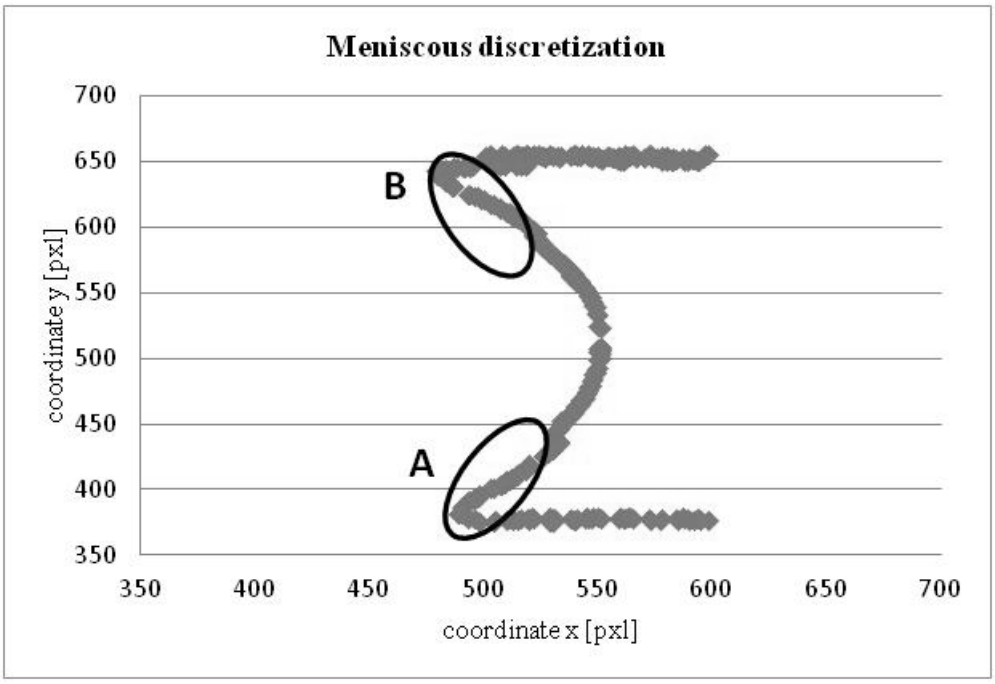

Figure 3.14 Discretized meniscus imported in Excel.

Once the discretized profile values were acquired in Excel, the two oblique lines A and B will be considered separately and both points series were fitting with a trend line; the slope of this line gives the contact angle value. For the lower contact angle the value obtained is 45° 6', see Figure 3.15, while the upper contact angle has a value of 40° 6'. The huge difference between the two values requires the development of a more accurate evaluation method.

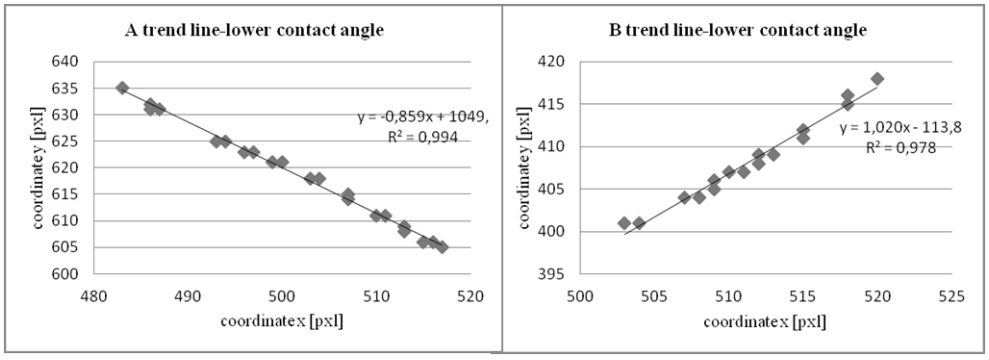

Figure 3.15 Trend line representation for lower and upper contact angle.

Third method

A picture of the receding meniscus is taken and analyzed using an image analysis software; the meniscus profile is discretized in points by gray levels evaluation. The value of these points is exported in a datasheet: the parabolic equation of the curve that fits all the point is carried out. In addition, other two points were tacked near the capillary inner wall to evaluate the effective capillary tube diameter. The derivative of the parabolic equation calculated in these two points returns the effective contact angle of the water solution inside the tube. The analysis starts with a live image of the receding meniscus (Figure 3.16) inside a capillary tube having of diameter of 100 micrometers; using a sophisticate software of image elaboration, the picture contrast were altered to discretize the meniscus profile; as the images shown, the contact angle region as a very low definition, and is impossible trough them to measure the contact angle accurately.

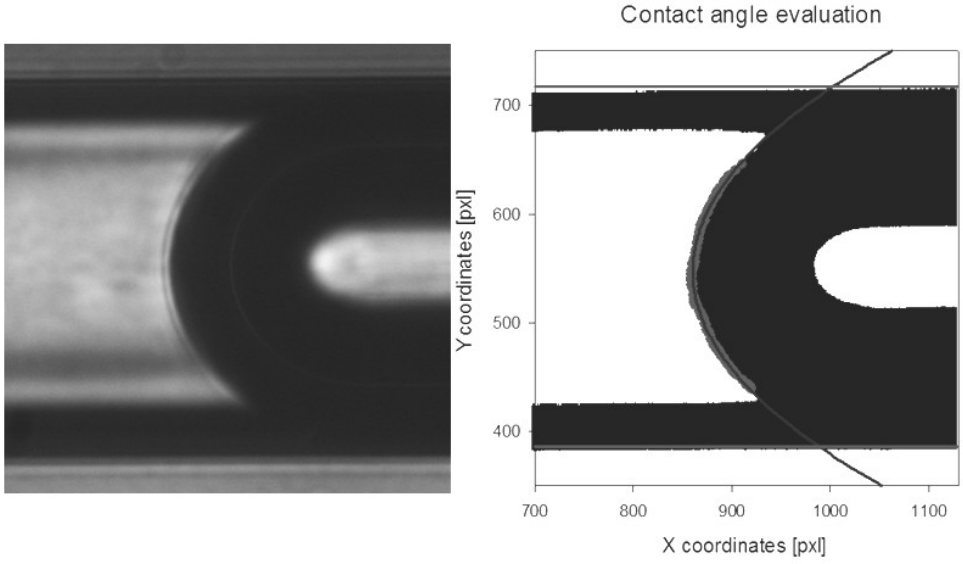

Figure 3.16 More accurate discretization of the meniscus.

As a result the software gives the coordinates of a high number of points along the meniscus profile; these data were plotted in a graph and another

software (*SigmaPlot 11*) is used to calculate the best-fit equation between the points. It returns the quadratic equation of an elliptic curve:

$$f(x): y = ax^2 + bx + c \quad (34)$$

$$f'(x): y = 2ax + b \quad (35)$$

Calculating now the point in which the first derivative of this equation is zero, the center of the curve was found. Summing and subtracting the capillary radius at y coordinates of the center, the contact points on the capillary walls are calculated. The first derivative of the elliptical equation in these two points gives the angular coefficient of the straight line tangent to the curve and passing through that points; then, the arctangent of each point gives the value in radians of the contact angle, that can be easily translated in degrees. Both angles shows the same value that corresponds to the value of 33° reported in literature.

4 RESULTS

"Technology is destructive only in the hands of people who do not realize
that they are one and the same process as the universe."
Alan W. Watts

4.1 Drying in Cotton Fabrics*Gravimetric results*

4.1.1.1 *Water Hardness*

These experiments have been done to understand the difference between bound water (i.e., the amount of water absorbed by the cotton fibers) and unbound water (corresponding to the amount of water laying on the surface). In these experiments the same amount of water soaked by a cotton swatch sample was put into a Petri dish. Water covers all the Petri dish bottom surface and has the same apparent surface area of the cotton swatch (which is actually cut to fit into the dish). Results in Figure 4.1 show that the drying rate of the cotton fabric is faster than the water evaporation speed in a dish.

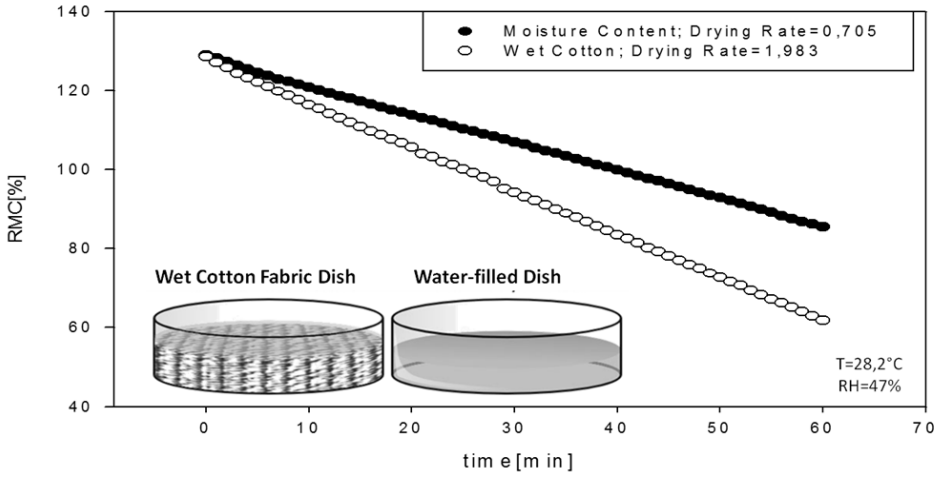

Figure 4.1 Comparison of drying rate in a cotton swatch and a dish filled with water.

Comparing the results obtained it can be seen that with the same apparent surface, the drying rate is greater for the porous sample than for a pool of solution of the same quantity. This highlights the importance of the surface water-air interface and demonstrates that the porous medium has an effective area more extensive than a flat water layer.

A large number of experiments were also performed on DEMI water in order to find an average trend for the drying curve both as regards the cotton fabric both as regards only the solution in the Petri dish (Figure 4.2).

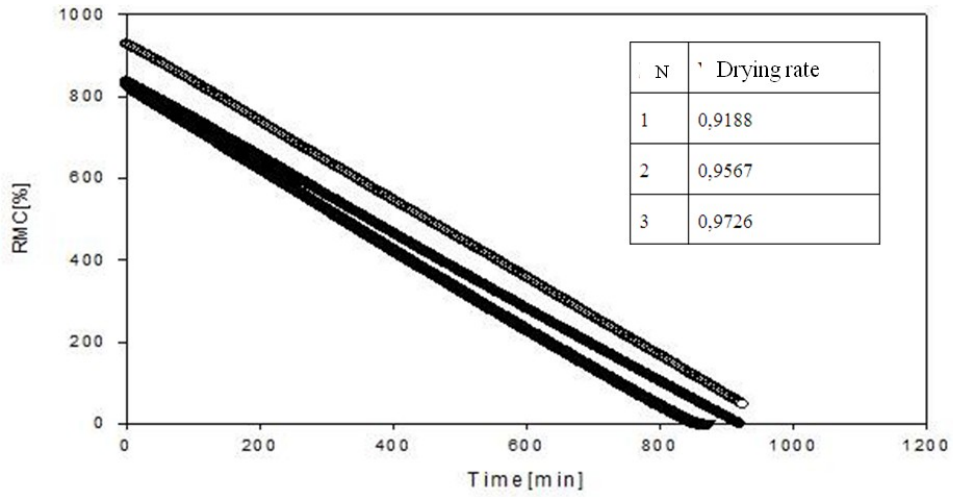

Figure 4.2 Comparison between different water drying curves in absence of cotton fabric.

The same tests were also performed by replacing the DEMI water solution with water solutions at different hardness to experimentally show whether, with increasing of water hardness, the drying rate in the cotton fabric would be increased. Results are shown in Figure 4.3.

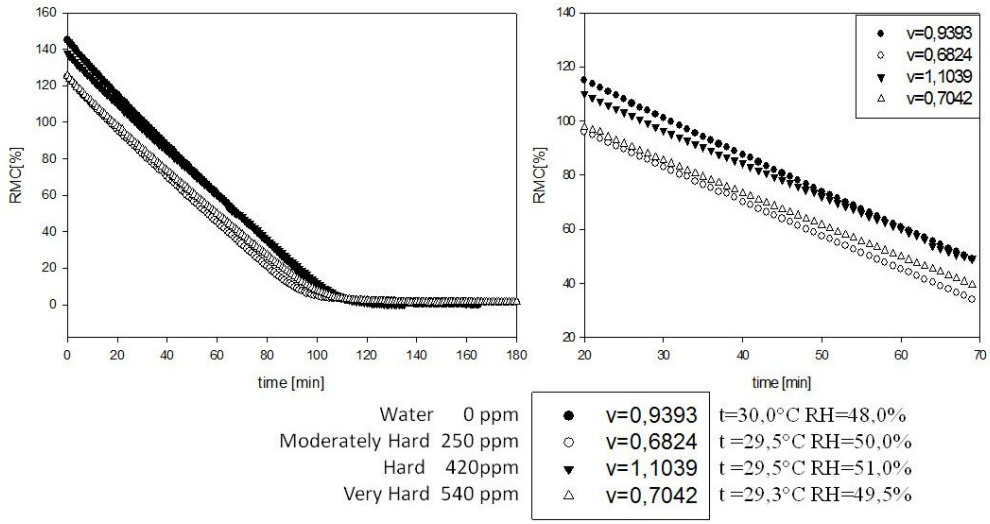

Figure 4.3 Comparison between different drying curves in a cotton fabric soaked in water having different hardness.

Drying curves show a counterintuitive results: an increase of the drying rate of the cotton fabric with the increase of the water hardness from 0 to 420 ppm of salt

concentration and a decrease of the drying rate value with the Very Hard water solution. It should be pointed out that 540 ppm is a really high concentration value, near to the solubility limit. After a complete characterization of the water solutions at different hardness degree in the cotton fabric, this condition were compared with the experiment in absence of cotton fabric as showed in Figure 4.4.

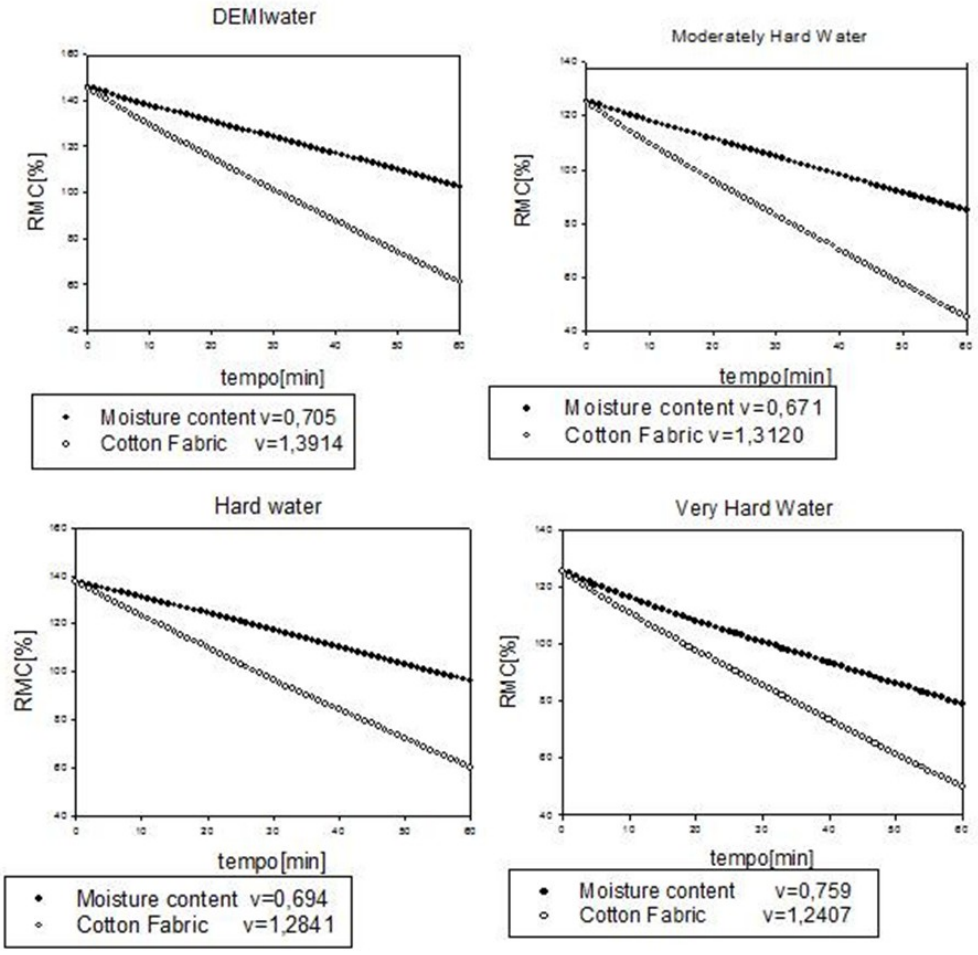

Figure 4.4 Comparison between the drying rate in a cotton fabric and in absence of fabric for water solutions at different hardness, the two samples having the same apparent surface area.

Again these experiments confirm that the wet cotton fabric sample evaporates faster than the same amount of water in a Petri dish.

Finally, having shown the effect of salts on porous media and the differences in drying rates with and without fabrics, other tests were carried out to compare the drying rate in absence of porous media for DEMI water and Hard Water solutions, in order to evaluate the hardness effect in the same conditions of temperature and

relative humidity. Figure 4.5 demonstrates that water hardness affects drying rate only in porous media.

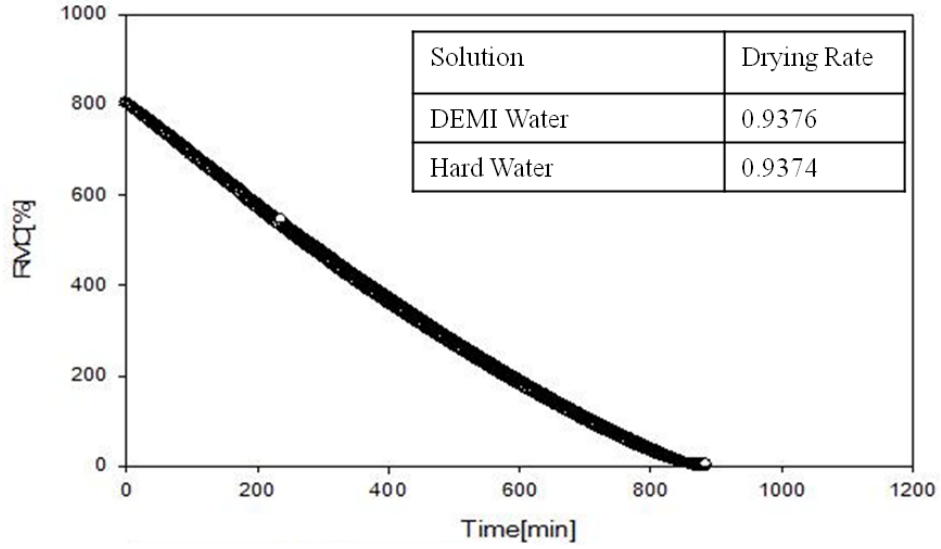

Figure 4.5 Comparison between the drying rate of DEMI water and Hard water solution in absence of fabric.

From these tests it is possible to see the presence of salts does not produce an increase in the rate of drying for a pool of water in the range investigated, while in cotton fabrics, the drying speed of the salt solutions is always greater than that of distilled water. As the graphs show, in experiments in which there is a porous medium, we have a drying rate greater than in experiments in which we only have a water pool. The reason for this increase must be sought in a different area of air-water interface that characterizes the two samples. In particular, the porous medium sample has a larger effective surface, which justifies an increase of the rate of drying.

4.1.1.2 Surfactants

Two sets of experiments were performed in this task: in the first set, a cotton swatch or wire was soaked in water and the amount of moisture was determined by measuring the net weight (i.e., the weight during the drying process minus the dry swatch or wire weight) as a function of time by a precision balance; in a second set of experiments, a dish with the same surface area of the cotton swatch was filled with water and again the net weight was measured as a function of time.

Determination of the drying rate in cotton fabric

Commercial softener products were tested. The water-surfactant solutions concentrations in water were chosen according to the product information. The drying speed value of DEMI water was chosen as the reference value so that the drying speed increase due to the surfactants can be evaluated. The drying curves for a cotton fabric are shown in Figure 4.6.

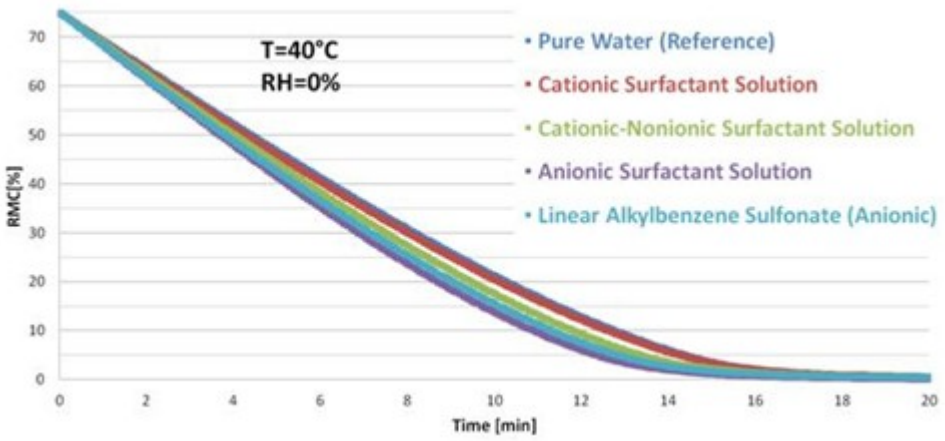

Figure 4.6 Water content versus time in a cotton fabric (area 5 mm^2; dry weight 0,35 g) by DVS.

The central part of the data sets was used as before to calculate the drying speed of the cotton fabric sample. The percentage increases are resumed in table 4.1 and graphically showed in Figure 4.7.

Table 4.1: DEMI water and surfactants solutions compositions and rate values.

	Sample	Composition	Drying Rate	Deviation
#		*[ppm]*	*RMC%/min*	*%*
1	Pure Water (Reference)	X	6,1	0
2	Cationic Surfactant Solution	18000	6,3	4
3	Cationic-Nonionic Surfactant Solution	18000	6,6	9
4	Anionic Surfactant Solution	6000	7,2	19
5	Linear Alkylbenzene Sulfonate (Anionic)	20000	7,2	19

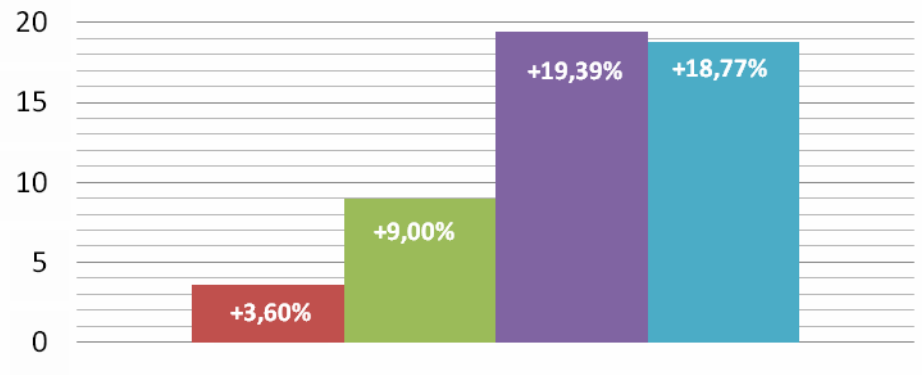

Figure 4.7 Increase percentage in drying rate due to surfactants.

Determination of the drying rate in a dish filled with water

This test shows that the actual interfacial area between air and water is larger than the apparent surface area in the cotton swatch. The same procedure was used to test the 2000 ppm Na-LAS solution (Solution1) drying rate. As usual the dish filled with water with and without Solution 1 was chosen as the reference sample. Another sample was a cotton swatch soaked in the same amount of Solution 1 into the Petri dish. The graph in Figure 4.8 shows the results of the experiments, reporting the slope of the three samples data. It can be noticed that, as a control, there is no significant difference in drying rate of water in the Petri dish with or without Solution 1.

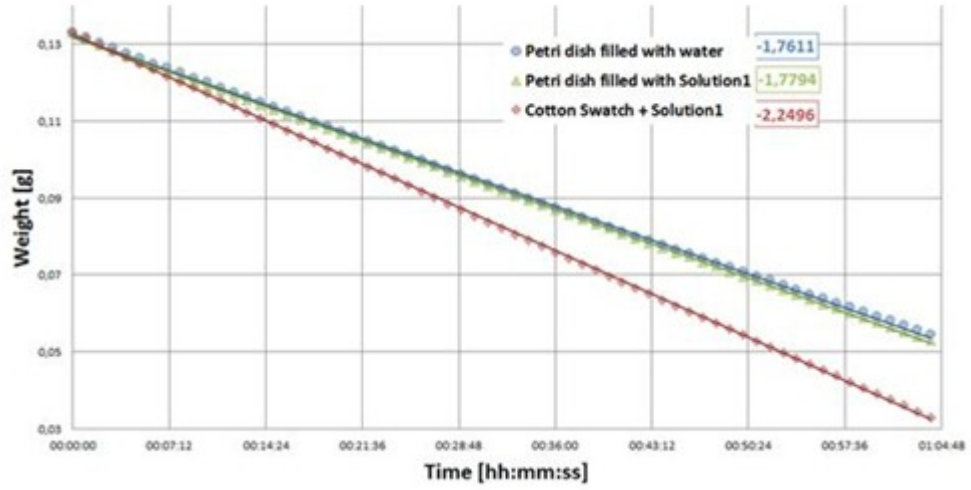

Figure 4.8 Comparison of drying rates in a cotton swatch and in a Petri dish filled with Solution 1.

In conclusion, as shown in Figure 4.8, the drying speed of the cotton swatch sample is 34% higher than the drying speed of the water in the Petri dish. A similar increase of 19% is found in Figure 4.6 for Solution 1 (the difference is due to a change in room temperature). This increase can be attributed to the higher actual surface area of the cotton swatch. More support to this conclusion is provided by the experiments described in the following sections.

4.1.1.3 Surfactant and Hard Water

Other experiments were carried out at the Dynamic Vapor Sorption to validate the well known effect of surfactant passivation due to water hardness.[226] In the following table 4.2 the solution tested and their effect on water evaporation were resumed.

Table 4.2: Surfactant and hard water solution effect on the drying rate in a cotton fabric.

	Sample	**Composition**		**Drying Rate**	**Deviation**
#		*Salts [ppm]*	*Na-LAS [ppm]*	*%/min*	*%*
1	**DEMI Water**	/	/	6,1	0
2	**DEMI Water+Na-LAS**	/	2000	7,2	19
3	**Medium Hard Water**	250	/	6,8	11
4	**City Water**	260	/	7,0	16
5	**City Water+Na-LAS**	260	2000	6,2	3
6	**Hard Water**	420	/	7,2	19
7	**Very Hard Water**	530	/	6,9	12
8	**Very Hard Water+Na-LAS**	530	2000	6,4	5

Two main results can be highlighted from these values. First of all, the drying rate trend due to water hardness was confirmed DVS, as shown by the graph in Figure 4.9.

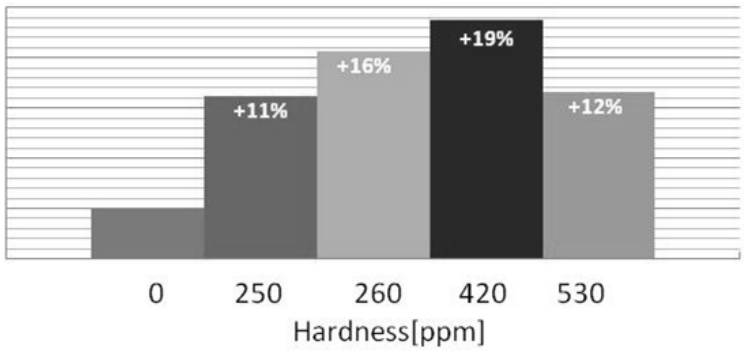

Figure 4.9 Increase percentage in drying rate due to water hardness.

The following graph (Figure 4.10) the strong effect that the water hardness has on surfactants is shown: a decrease of more than 10% in drying rate can be appreciated comparing the drying rate of surfactant in DEMI water (W+NaLAS) and the rate of drying in surfactant solutions made by City Water (CW+Na-LAS) or Very Hard Water (VHW+Na-LAS).

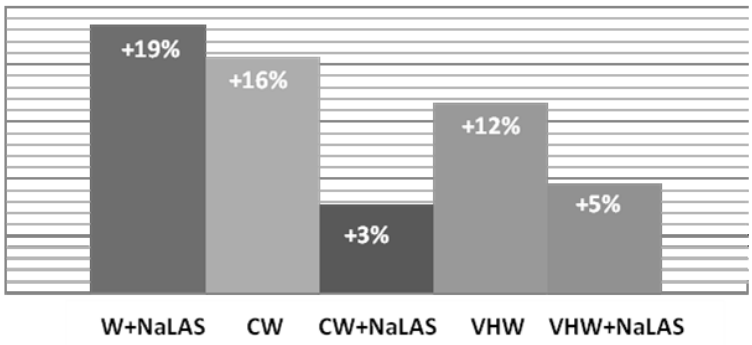

Figure 4.10 Drying rate changes due to surfactant and water hardness.

The second result is that the drying rate value of Hard water solution and NaLAS solution is the same. This could open the way to other new approaches and to new active agents that could take advantage of water hardness effect only.

4.2 Drying in a Capillary Tube

4.2.1 Meniscus Displacement

The drying process of a liquid solution inside a silica capillary tube with an inner diameter of 100 μm, closed by one side, was evaluated using the procedures described in section 3.1.3. The void degree (*L*), defined as the distance between the meniscus and the open capillary side at a certain instant of time, was identified as a measure of water evaporation, being the evaporation rate inversely proportional to

L. By using the automated microscope stage to hold the sample, the relative position between the open side of the capillary tube and a fixed point on the meniscus was measured. This procedure allows the observation of the drying process in real time in multiple capillaries. In Figure 4.11 the drying of DEMI water in a capillary tube (Ø 100 μm) under room temperature is shown. According to the theory illustrated in section 2.3.2, the data can be fit with a power low curve with an exponent equal to 0.5.

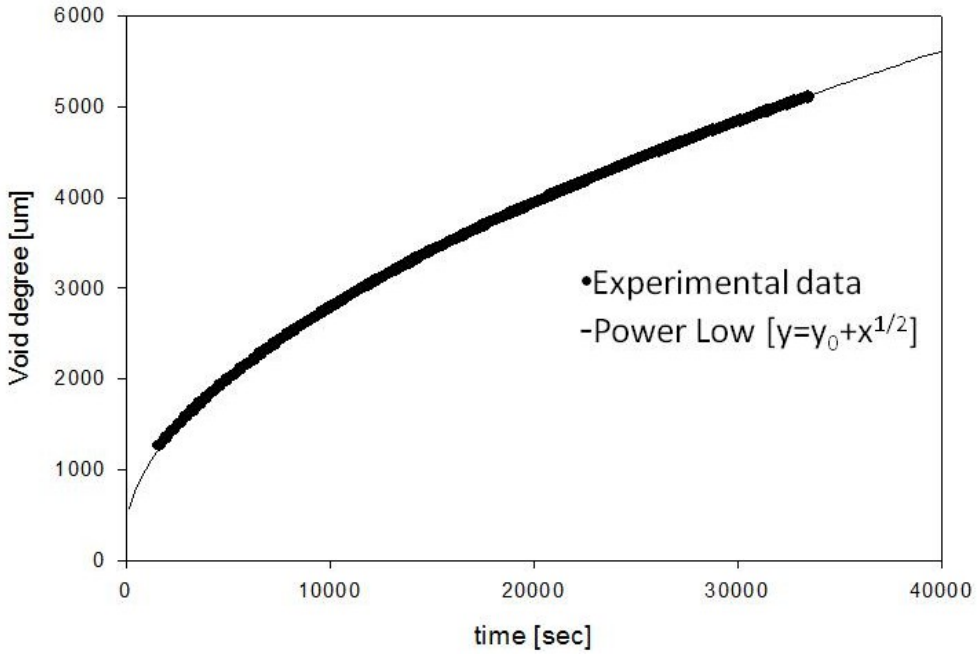

Figure 4.11 DEMI water evaporation in a capillary tube of 100 μm.

To highlight the drying rate changes in time, drying rate were plotted versus time, as reported in Figure 4.12.

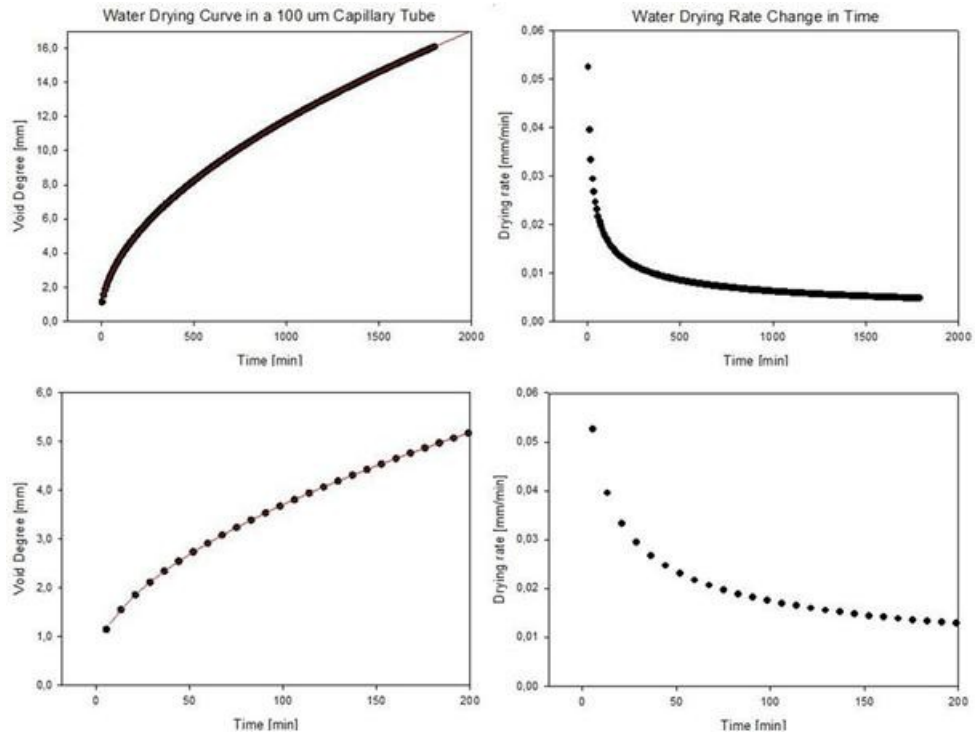

Figure 4.12 Water drying in a 100 μm capillary tube as in Figure 4.11. Drying curves on the left, drying rate vs. time on the right.

In this plot, two drying rate regimes are clearly distinguishable. When L has a value comprised between 0 and 2.5 millimeters, the drying rate is really fast and water molecules are free to evaporate, driven by a high concentration gradient between meniscus surface and the region near to it; for L greater that 2.5 millimeters a strong decrease of the drying rate occurs.

4.2.2 Contact Angles

The evaporation of diluted surfactant solutions in capillaries were influenced by the angle that the solution forms in contact with the walls of the capillary itself. The contact angle depends on the concentration of surfactant (t decreases with increasing surfactant concentration), as shown in Figure 4.13.

.

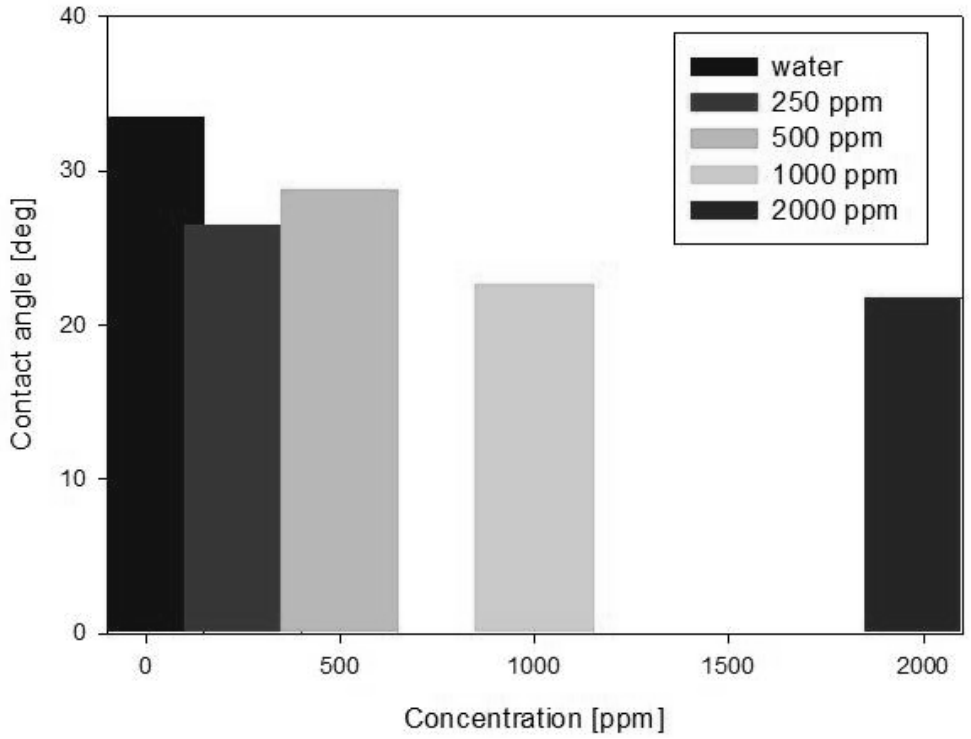

Figure 4.13 Contact angle changes due to surfactants concentration.

4.3 Topography of Cotton Textile

The Solid and liquid surfaces can be characterized by theirs chemical composition, geometry and roughness. The way liquids interact with textile fabrics may involve one or several physical phenomena such as fiber wettability, depending on the intermolecular interaction between liquid and fiber surface, their surface geometry, the capillary geometry of the fibrous assembly,[56] the amount and chemical nature of the liquid as well as on external forces. A rough textile surface possesses pores, crevices, capillaries or other typical structures with their own characteristic wetting and penetration properties. As a consequence, the apparent contact angle on these surfaces will be affected by thermodynamics and kinetics associated with such intrinsic structures.

Texture of fabric changes the porosity value and strongly influences the textile characteristics such as mass, thickness, draping ability, or air permeability.[57-59] However, there are very few systematic investigations of quantitative relations between construction parameters, topography of fabrics and their wettability.

4.3.1 Imaging by CLSM

Confocal microscopy is defined as a method of optical microscopy by which structures in the focal plane are visible and those outside the focal plane are suppressed. The scanning of the focal plane through the object being imaged enables the collection of three-dimensional microscopic image data sets (also known as z-stacks). This technique was applied to evaluate the fabric microstructure of the cotton sample. To highlight the fibers a tracer dye (Rhodamine B) was used. In Figure 4.15 the helix shape of a single cotton fiber is shown; this 3D reconstruction was made from a z-stack consisting in 15 slices distant from each other 1 μm along the z axis. The fiber section seems to be flat because the sample is compressed between two slides..

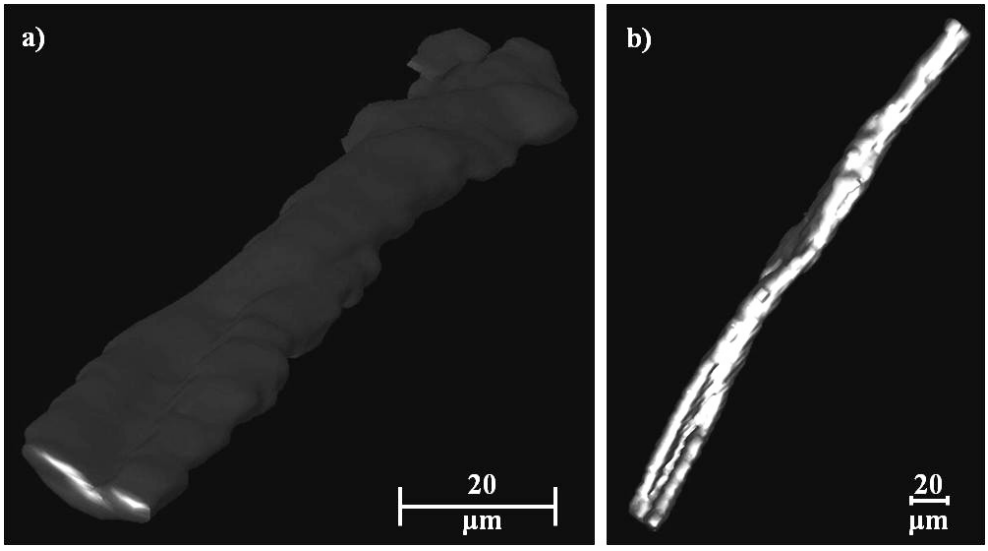

Figure 4.14 3D reconstruction of a single cotton fiber from a z-stack acquired in confocal microscopy. In a) arrangement in space underline the fiber section, in b) the helix structure were shown.

In Figure 4.15 some pictures shows the investigation carried out in confocal microscopy on single cotton fibers at high magnification (40x). Fibers thickness was evaluated and the typical helix shape of cotton fibers was taken into account (Figure 4.15 a-c); thickness ranges from 16 to 22 μm, in line with literature results. Other measurement were done to evaluate space between fibers in fabrics, showing an inter-fiber characteristic space of 7-25 μm.

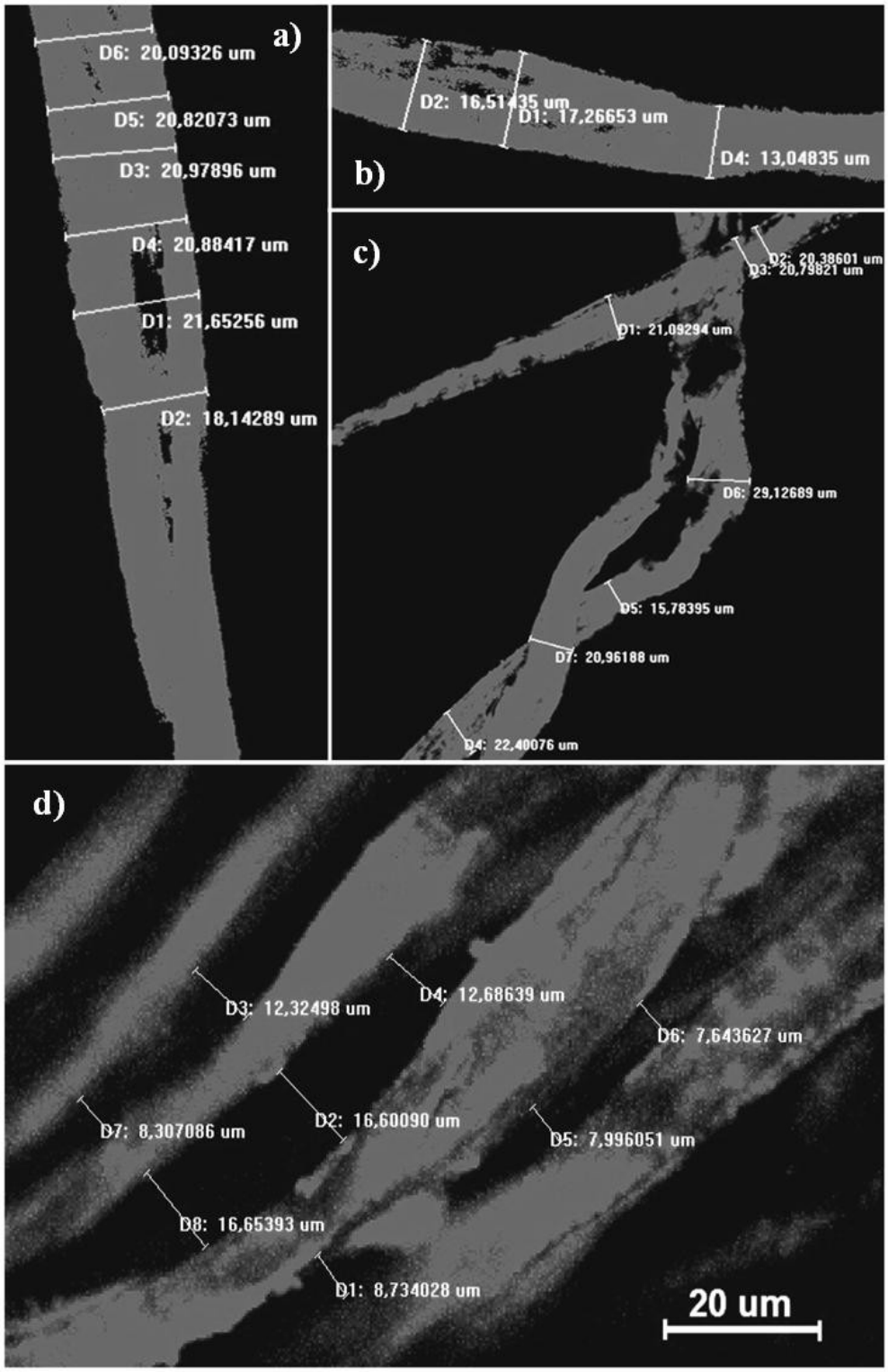

Figure 4.15 Cotton fibers visualized in confocal microscopy at high magnification (40x); in a-c) fibers thickness evaluation; in d) space between fibers measurement.

In addition, similar experiments were carried out on a single cotton yarn (Figure 4.16) to evaluate fibers location and porosity. The twisted shape of the yarn geometry can be appreciated, due to the twist the fibers were subjected to during yarn fabrication.

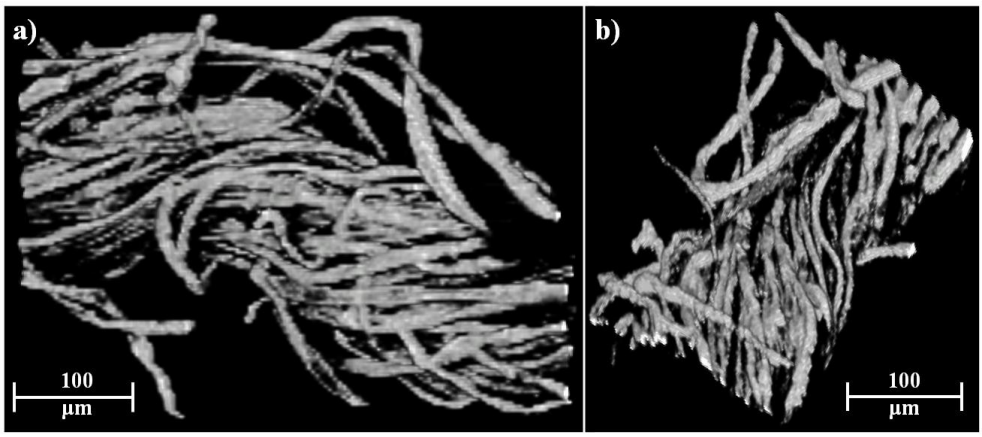

Figure 4.16 Single yarn 3D reconstruction by confocal microscopy.

The average porosity of the single yarn was found to be equal to 0.7, so that the 70% of the intra-yarn space can be occupied by a liquid during wetting. Finally, the whole cotton fabric structure was investigated. In Figure 4.17 a 3D reconstruction of a *z-stack* consisting in 65 slices distant from each other 5 µm along the z axis is shown as viewed in the x-y plane. These results confirm the previous experiments about the effective cotton fabric surface and give a qualitative measure of the cotton surface roughness.

Figure 4.17 Cotton fabric microstructure at high magnification (10x) by confocal microscopy

The same 3D reconstruction is presented in the next images (Figure 4.18) with a different angle to show the roughness of the cotton surface.

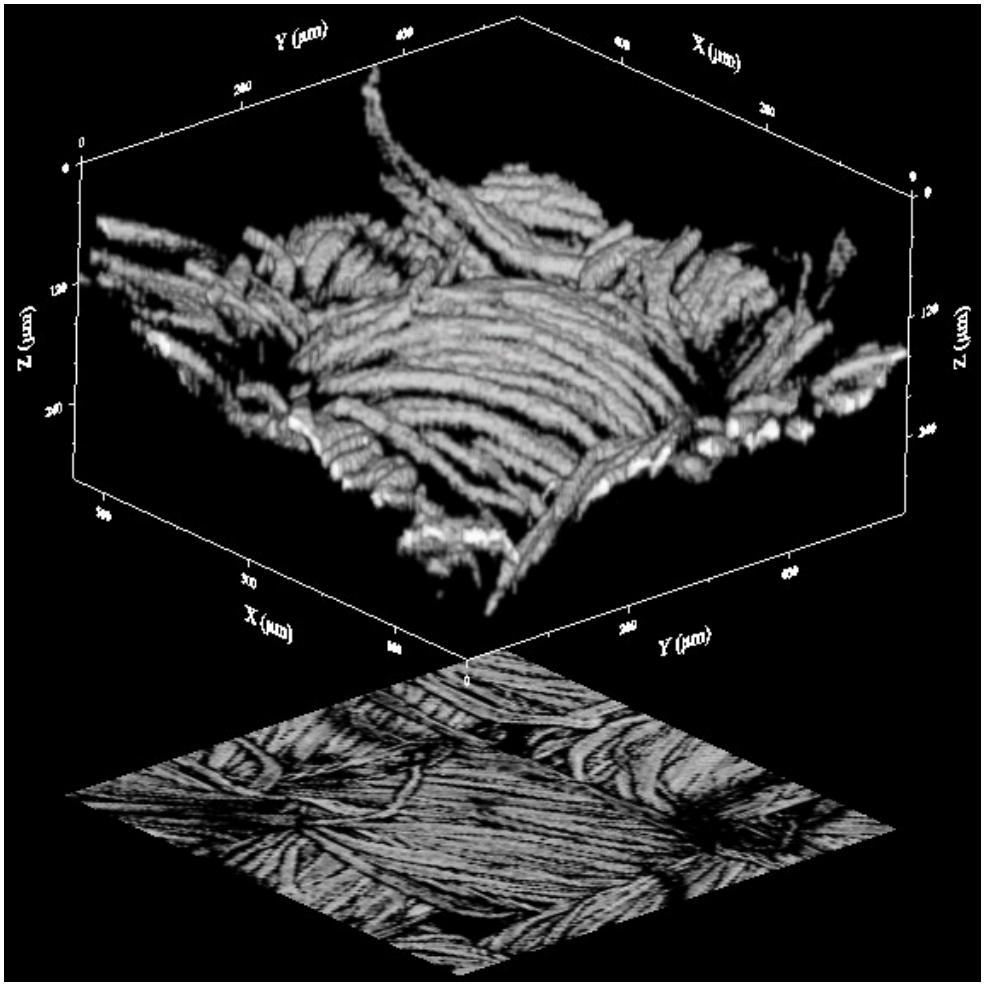

Figure 4.18 3D reconstruction of the z-stack showed in Figure 4.17.

Porosity evaluation give back the same value of 0.7 obtained for the single yarn. To evaluate the effective surface area of a cotton fabric, more accurate investigations of the fabric surface were made. Taking advantage of the affinity of the dyes (Rhodamine-B and Fitch) used in the experiments with the immersion liquids (water and silicone oil), another imaging tecnique was developed to highlight the liquid surronding the fibers (so that the latter are seen in negative by confocal microscopy). Cotton fabric was immersed in a silicon oil at low viscosity; the dye (Rhodamine-β) goes preferentially in the oil and shows the cotton surface as a mold (see Figure 4.19).

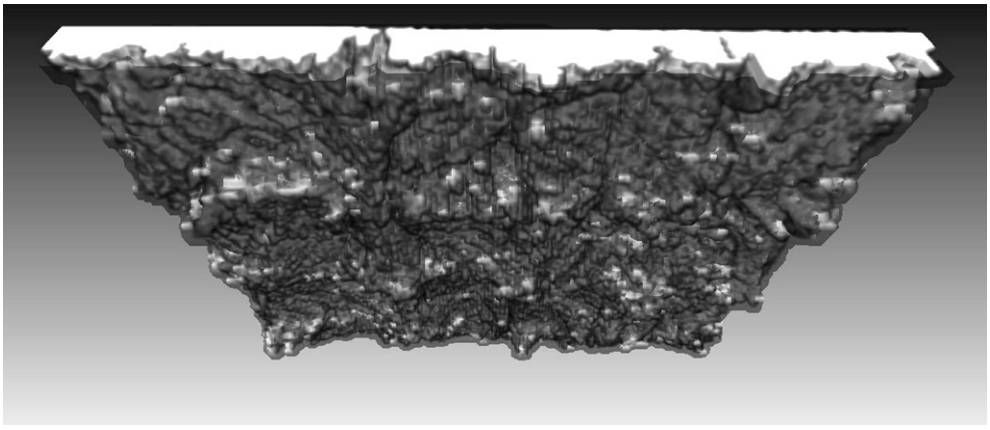

Figure 4.19 3D Mold reconstruction from a negative z-stack of cotton fabric in silicon oil.

In this conditions, the surface evaluation is easiest and more accurate. The increase in surface area between a flat surface and the cotton fabric is about 60%. These results confirm the previous thermo-gravimetric results and give a qualitative measure of the cotton surface roughness.

4.3.1.1 Visualization of fabric microtomic slices

Some cotton fabric samples were included in an epoxy resin, which polymerizes in 48 hours at 70°C, and then cut in a sequence of 20 μm deep slices, as shown in Figure 4.20.

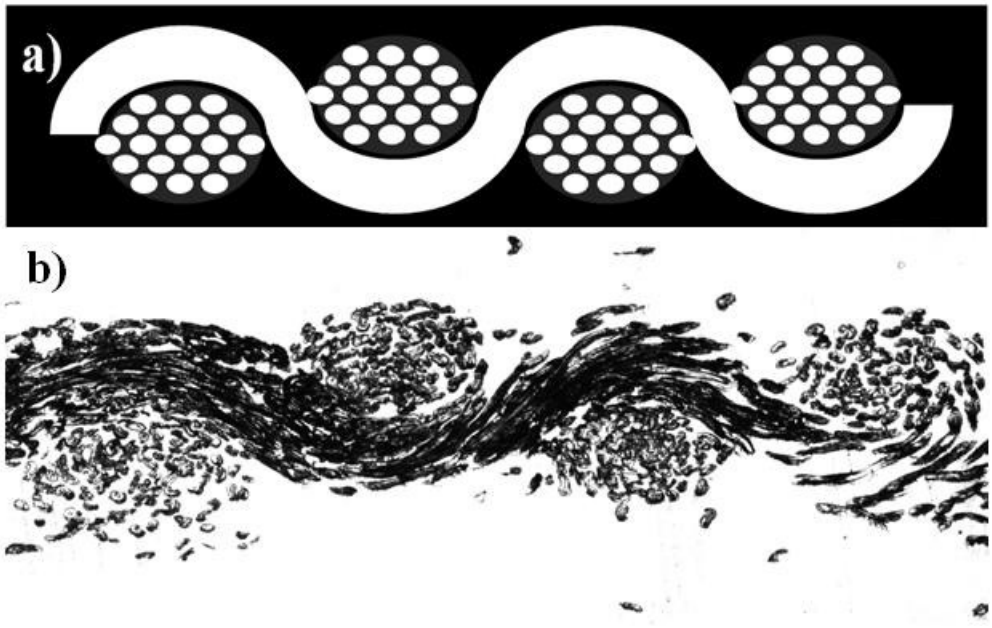

Figure 4.20 a) schematic of cotton fabric slice, warp and weft yarns are highlighted; b) image of a cotton fabric slice in bright field.

After this process, the slices were placed on a slide and dyed with Rhodamine-B. As can be noticed in Figure 4.21, these pictures allow one to appreciate the intra-yarn and inter-yarn porosity. In this fabric, warp and weft view present the same yarn arrangement. Each fiber composing the warp and weft yarns can be distinguished.

Figure 4.21 Expanded particular from Figure 4.20.

Other analysis were done to highlight the crystalline structure of the cotton fibers. In polarized light, as known from literature[231, 232], cotton fibers presents a birefringence, that can be clearly seen in Figure 4.22.

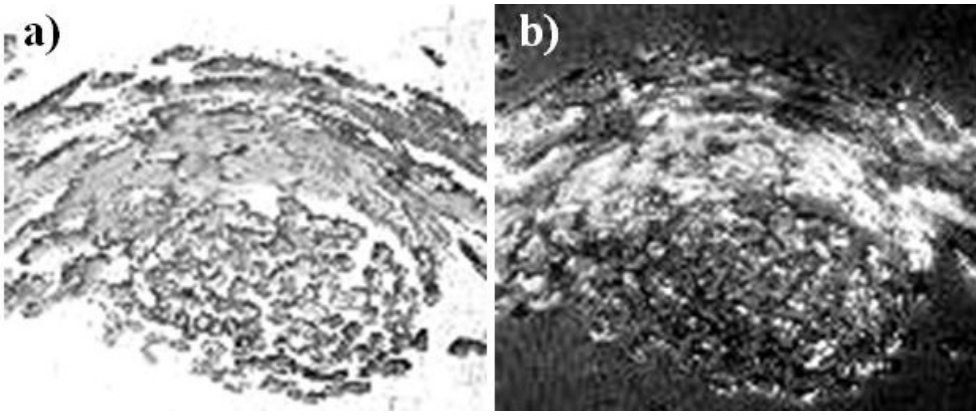

Figure 4.22 a) image of a cotton fabric slice in confocal microscopy, b) same view in polarized light.

4.3.1.2 Water Layer Visualization on Cotton Surface

While the microscopy of dry cotton has been extensively described, real time microscopy characterization of a water film on a cotton surface is an open

challenge. A non-invasive procedure was developed to observe the water layer on a cotton fabric by CLSM. This methodology allows to examine and reconstruct the three-dimensional structure of liquid and solid surfaces with a depth of several hundred microns. The systems examined were constituted by a cotton fabrics substrate wetted by a volume of water equal to 8 times the volume of the cotton fabrics (a scheme of the system is shown in Figure 4.23).

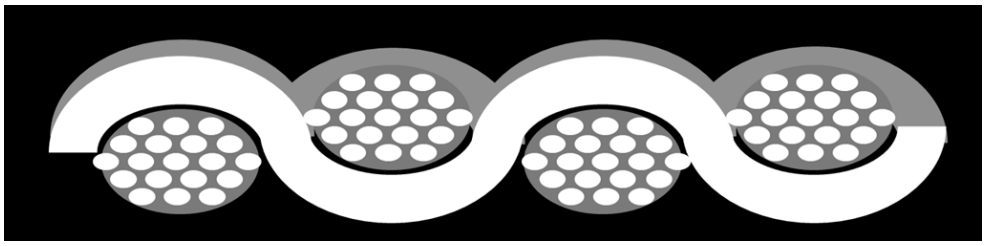

Figure 4.23 Scheme of the water (gray) on the textile substrate (white).

This considerable amount of water is necessary to observe the increasing corrugation of the air/water surface that, initially flatten, becomes more and more rough during the evaporation process. First attempts to investigate the water film laying on cotton fabric are shown in Figure 4.24.

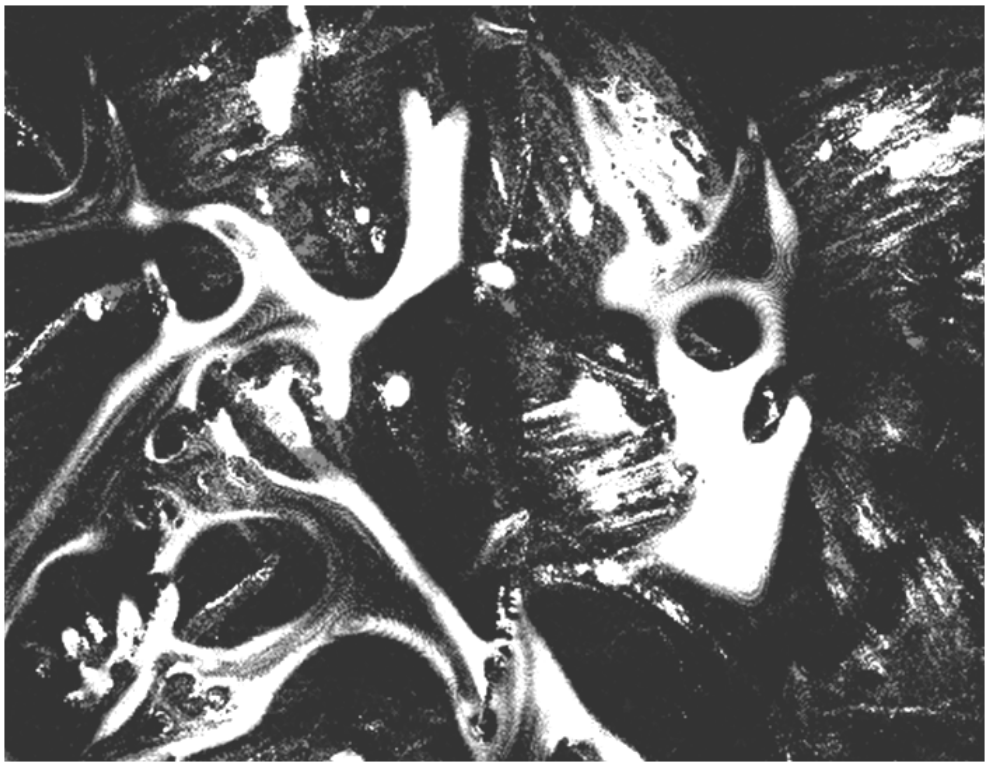

Figure 4.24 Water film laying on cotton fabric visualized by confocal microscopy.

In Figure 4.25 and Figure 4.26 the well-defined structure of the porous substrate underlying the liquid film can be appreciated.

Figure 4.25 Section of the 3D reconstruction of the water surface (in white) on cotton fabrics (below, in black) showed in figure 4.16.

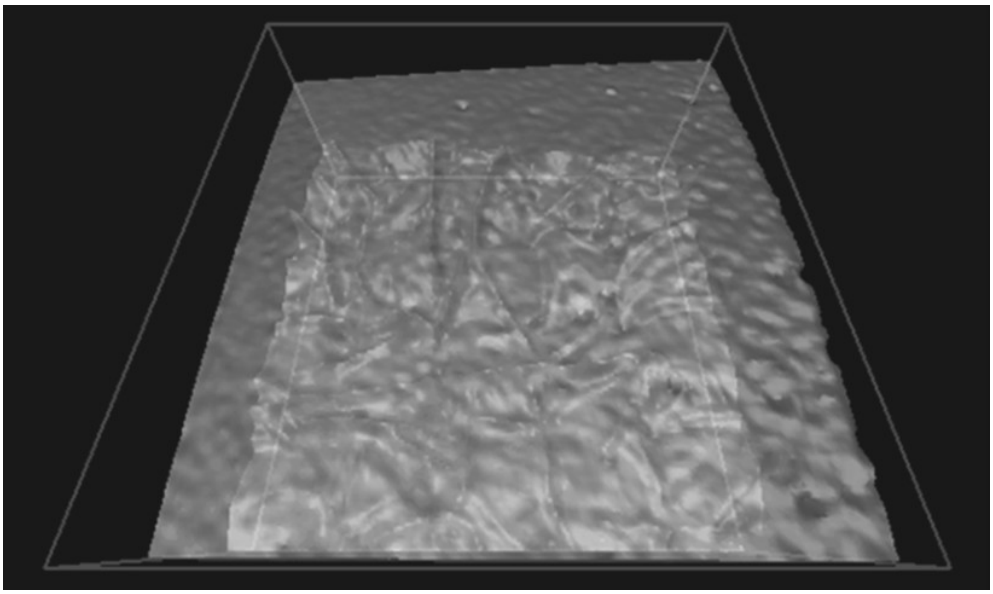

Figure 4.26 3D reconstruction of a z-stack acquisition in confocal microscopy. Water surface on cotton fabrics.

This visualization of the gas/liquid surface has been carried out to investigate the drying of the water layer during time (Figure 4.27).

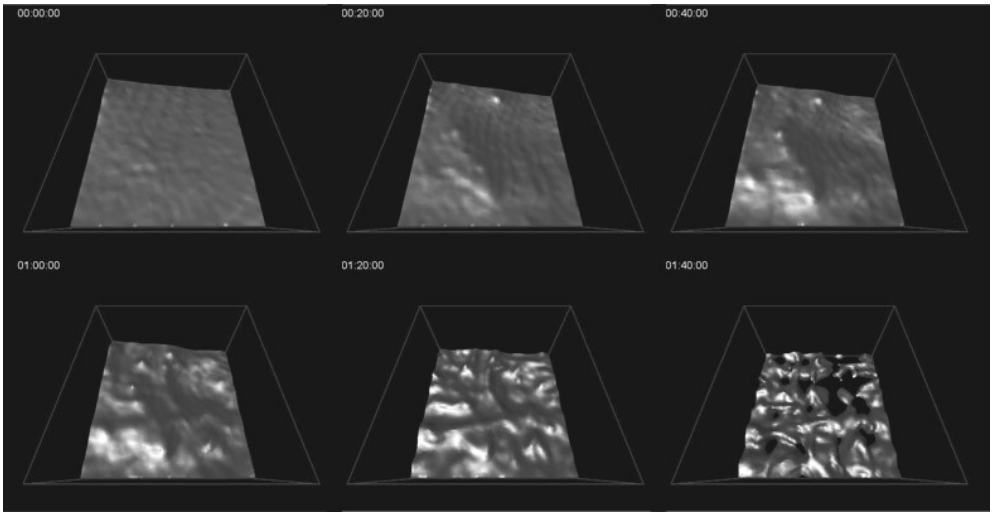

Figure 4.27 Water surface drying on cotton fabrics.3D reconstruction of a z-stack acquisition in confocal microscopy.

The surface receding was not only visualized but also 3D reconstructed from the z-stack, giving the possibility of area calculation and curvature evaluation. The method illustrated in this work is relevant for the study of the fluid interphase; visualization of the gas/liquid surface and the liquid/solid surface below can help understanding the way these two interfaces interact with each other. A quantitative analysis of the water layer surface area vs time is shown in Figure 4.28.

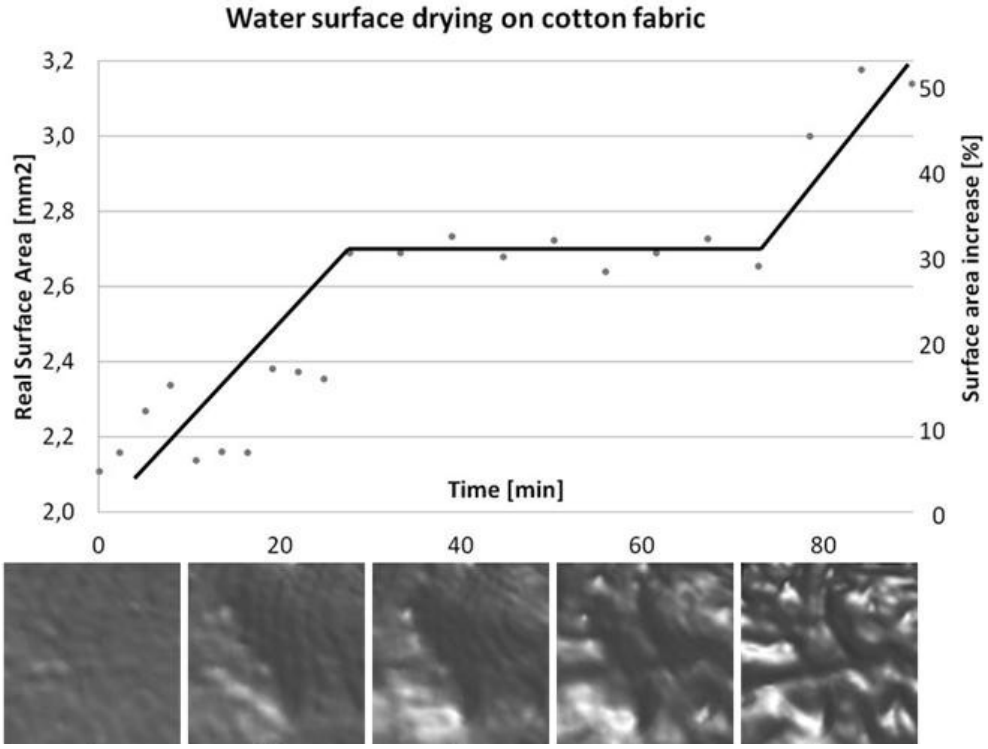

Figure 4.28 Surface area increase in time, as can be seen in **Figure 4.27**.

The surface increase is shown in the upper part of Figure 4.28 in terms of surface area [mm^2] (left axis), and percent increase [%] with respect to the initial area (right axis). It should be pointed out that the initial surface, as it can be seen in the images of Figure 4.28, is not completely flat but slightly corrugated and curved. This corrugation, if compared with an ideal flat surface, shows an increase of about 20%, equal to 0,4 mm^2. The images in the sequence of Figure 4.28 correspond with the value on the time axis. It should be notice that initially the surface area increase (0-25 min) because of the fluctuation of the receding surface, and then (25-70 min) remains constant around 30%. In the final period (70-90 min) the surface increases steeply to reach the 60% final value, equal to the dry surface value, as found out from Figure 4.19. The question that arises from these data is: If the constant drying rate is connected with an increase in surface area, why does the surface area show such a complex time dependence? A possible answer to this question lies in the equilibrium between two "forces", evaporation and capillarity; both have an important role in the drying process and both tend to increase with the increase of surface area. Another possible explanation is in the dimentions of the observed region. The surface we are looking at measures 1,7 mm^2 and represents a

very small region compared whit the apparent surface of 962,1 mm^2, equal to the surface of a Petri dish (Ø 35 mm) investigated in section 4.1.1. The general trend of data is a surface increase from 0% to 60% in a defined amount of time, and probably is the only result to look at because of the surface fluctuation in a dynamic process like drying. Last thing to specify is about the time scale; the process appears faster because of sample dimensions.

4.3.2 Reflected Light Macro Imaging

Visualization experiments based on light reflection were done to obtain a tridimensional image of the water layer on the cotton fabric surface. The procedure to run these experiments consists in lighting the sample with a lamp at a certain angle of incidence. Sample surface reflects the light that bounces back with a different angle of reflection. To catch the reflected light a camera is oriented along the angle of reflection, aimed at the sample, and is connected to a PC. To show the difference between the water layer surface in a Petri dish and the wet cotton surface, both samples are analyzed. The image in Figure 4.29 shows the water layer surface in a Petri dish.

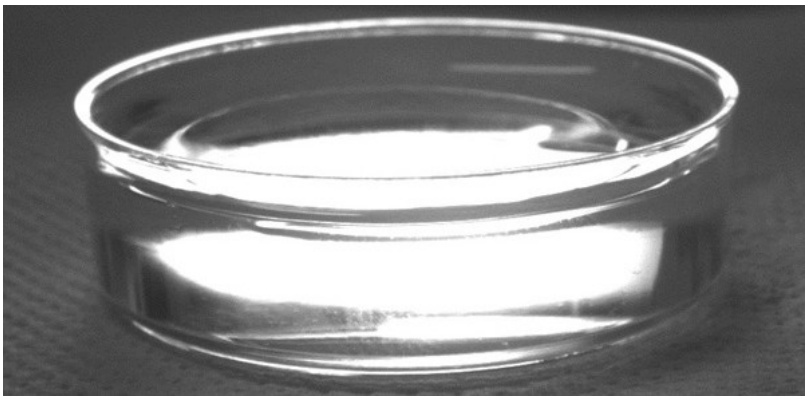

Figure 4.29 Water surface in a Petri dish.

Near the wall the surface curves under the capillary effect and is flat elsewhere. The short sequence in Figure 4.30 shows a cotton swatch before (a) and after (b-d) pouring water on top of it. The cotton fabric (which is a low magnification view of the microstructure shown in Figure 4.18) is visible as a surface roughness in Figure 4.30.a. Right after pouring water (Figure 4.30.b), the water layer is almost flat and surface microstructure is still visible below. As time goes on, waves and valleys appear in the water layer (Figure 4.30.c), which becomes more undulated in Figure

4.30.d. Eventually, the same appearance as in Figure 4.29.a is found at the end of the evaporation process. These images provide evidence of a corrugated air-water surface, which will then expose a higher interfacial area for mass transfer as compared to the almost flat surface of water in a Petri dish (Figure 4.29). In conclusion, higher drying rate in cotton fabrics is mostly due to a larger interfacial area. Interfacial agents capable to increase the water surface area in the fabric should be then selected in order to speed up the drying process.

Some experiments, as described in section 3.2.1.1, were conducted visualizing the samples surface by optical imaging in reflected light during the thermo-gravimetric analysis. In Figure 4.31.a the characteristic drying curve were reported in graph and the points that corresponds to the images from b to e were indicates; in the sequence reported in Figure 4.31.b-e, the increase of surface area can be appreciated, as previously shown in Figure 4.30. These pictures offers another confirmation of the cause-effect correlation between the surface increase and the drying rate improvement.

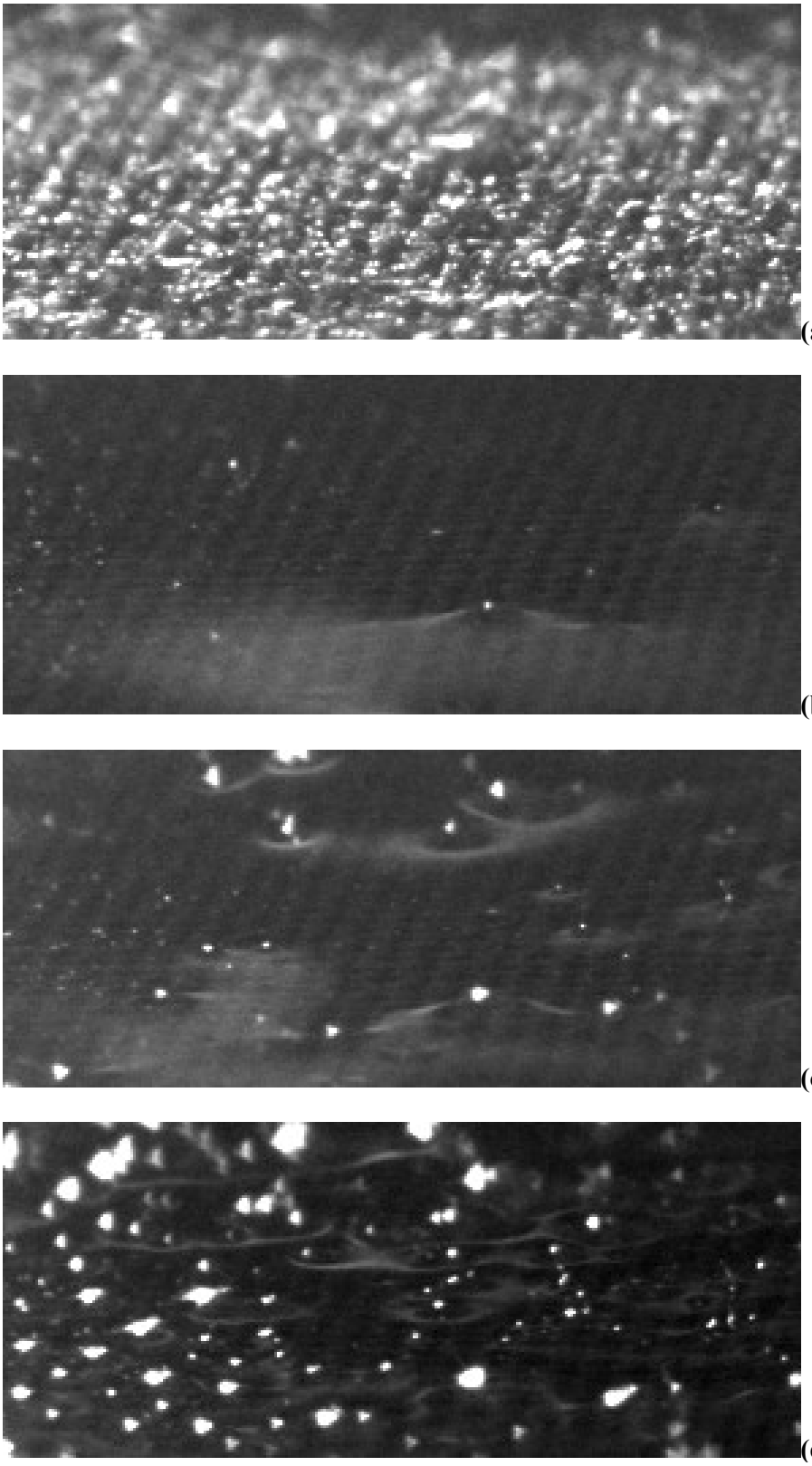

Figure 4.30 Image sequence showing a cotton swatch before (a) and after pouring water on top (b-d).

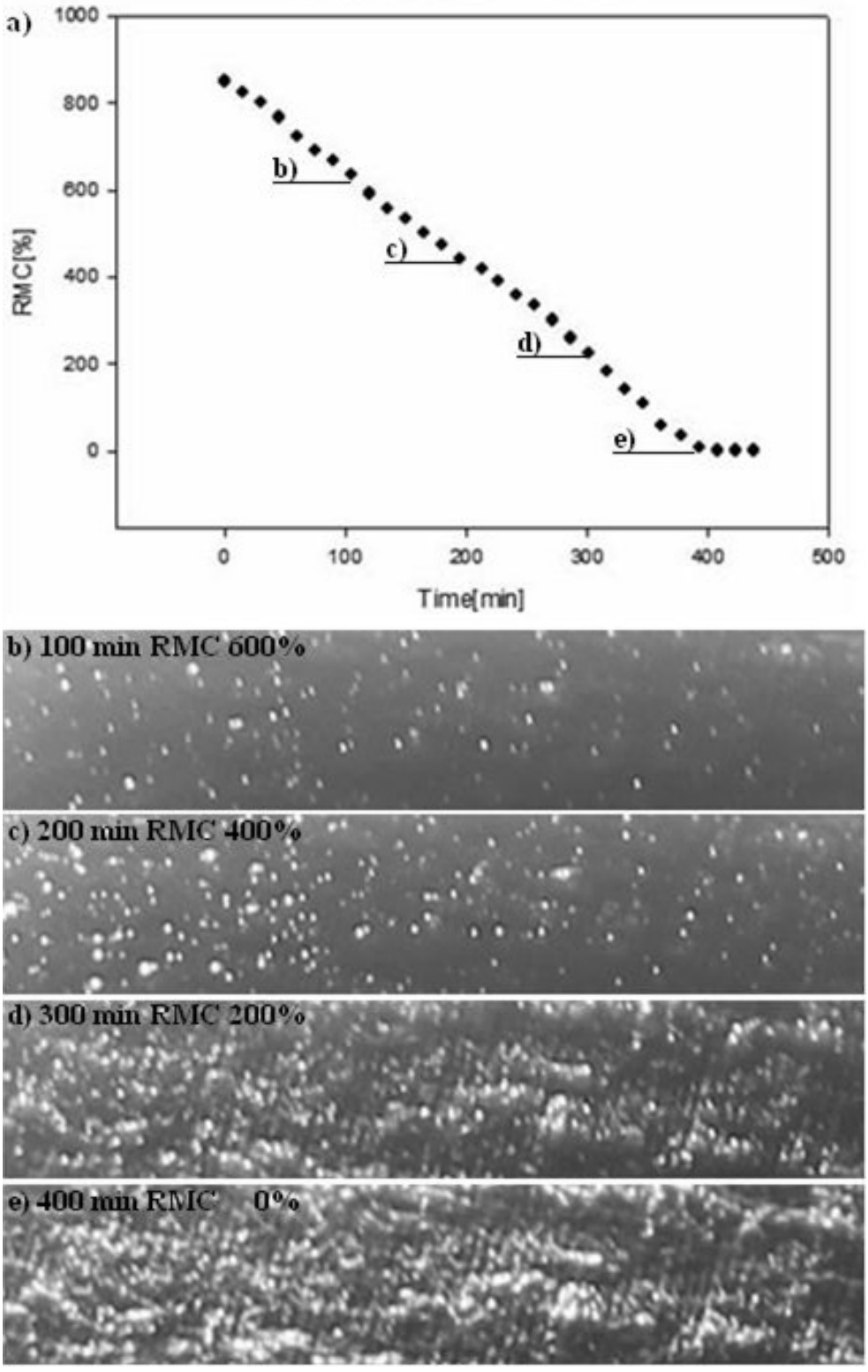

Figure 4.31 Thermo-gravimetric experiment coupled whit reflected light optical imaging.

5 DISCUSSION

"The real point of honor is not to be always right.
It is to dare to propose new ideas, and then to check them."
P. G. de Gennes[1]

Jackson and James[233] in 1985 define cotton fabric a fibrous porous material; all fabrics are in fact a porous media with a fractal structure[123] with different complexity degrees. For cotton, things are complicated by nature: each cotton fiber is a natural cell with a complex structure, as shown in Figure 5.1. The fiber is most often spun into yarn or thread and used to make a soft, breathable textile.

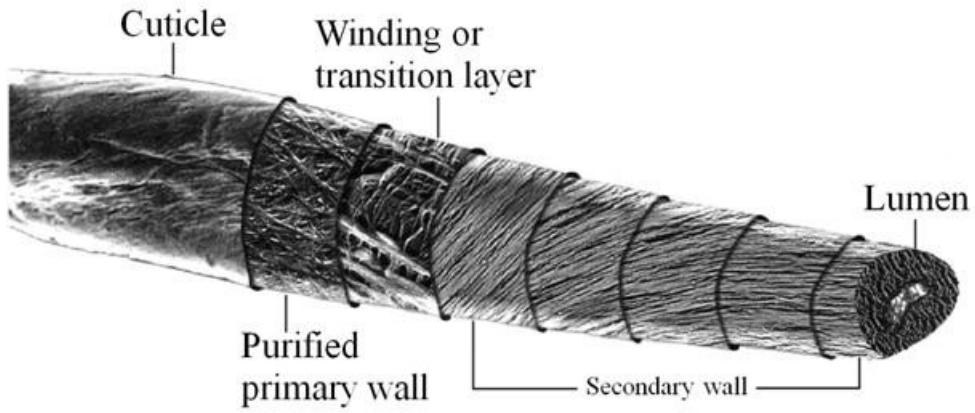

Figure 5.1 A computer-generated montage of a fiber segment constructed from individual transmission, adapted from *Cotton fiber chemistry and technology*[234].

In Figure 5.1, fiber surface, primary wall, and secondary layers were shown at different magnifications to better visualize fibrillar structures and the various fiber layers from surface to lumen. The surface marked cuticle is an SEM view of a scoured and bleached fiber surface and was used as the skeleton of the montage. All other segments are taken from transmission micrographs and are shown at higher magnifications. No fibrils are visible in the SEM of the cuticle because of its relatively low magnification as well as the presence of non-cellulosic materials. The fiber surface at the cut end of the fiber shows fibrils that have been separated by swelling[234]. Structures and porosity of cotton fibers will be examined in the next

[1]Extract from a speech delivered Honor and Patience at the Institute of France Tuesday, October 22, 2002 on the occasion of the return of the five academies.

section with the clear intent of understand where the water is located inside the fibers, a concept deeply discussed in section 1.3.

5.1 Cotton Fiber Structure and Porosity

The fundamental unit of cotton fabrics' structure is the fiber, each fiber being substantially composed by the cell wall remnant of a single cotton cell. Cotton fibers used for fabrics are approximately 2.8 cm in length[235] and approximately 20 microns in diameter (30 μm when wet[236]) thus having an aspect ratio[234] of 10^3. The primary wall is estimated to be composed by 100 to 200 molecules in thickness (0.1 to 0.2 μm), and is made up of cellulose (30%), other neutral acid polysaccharides, waxes, pectic compounds, and proteins[237]. The secondary wall thickness is 8 to 10 μm. At maturity, cotton fiber is 89% cellulose[238].

The cross section of a cotton fiber is a complex structure, as shown in Figure 5.2. When wet, it appears like a capillary tube with a 15 μm water-filled space called the lumen surrounded by a 7.5 μm thick cell wall that is more than 98% cellulose. The lumen is where the cytoplasm of the original cotton cell was located when the plant was still growing. When cotton fibers are removed from the plant, there is also a less than one micron of hydrophobic cell wall coating that is scoured away during the process of making cotton fabric.

5.1.1 Fibers and Lumens

The cross sectional area of a wet fiber is 700 μm^2; of this, 525 μm^2 is cellulosic and 175 μm^2 is the lumen(Figure 5.2.b). Assuming an average fiber is 3 cm long, a typical wet fiber contains a volume of $1.6*10^7$ μm^3 of cellulose and has a lumen with a volume of $5.3*10^6$ μm^3. In dry cotton the volume of the lumen approaches zero as the fiber collapses into a kidney shape and nearly all of the volume of the dry fiber is cellulose. Cotton cellulose has a density of 1.55 gm/cm^3. Thus each dry fiber weighs 25 micrograms[239]. Thus there are $4x10^7$average fibers in a kilogram of dry cotton. If only the lumen of cotton could be filled with water, 1 kilogram of dry basis weight cotton would contain 210 grams of water.

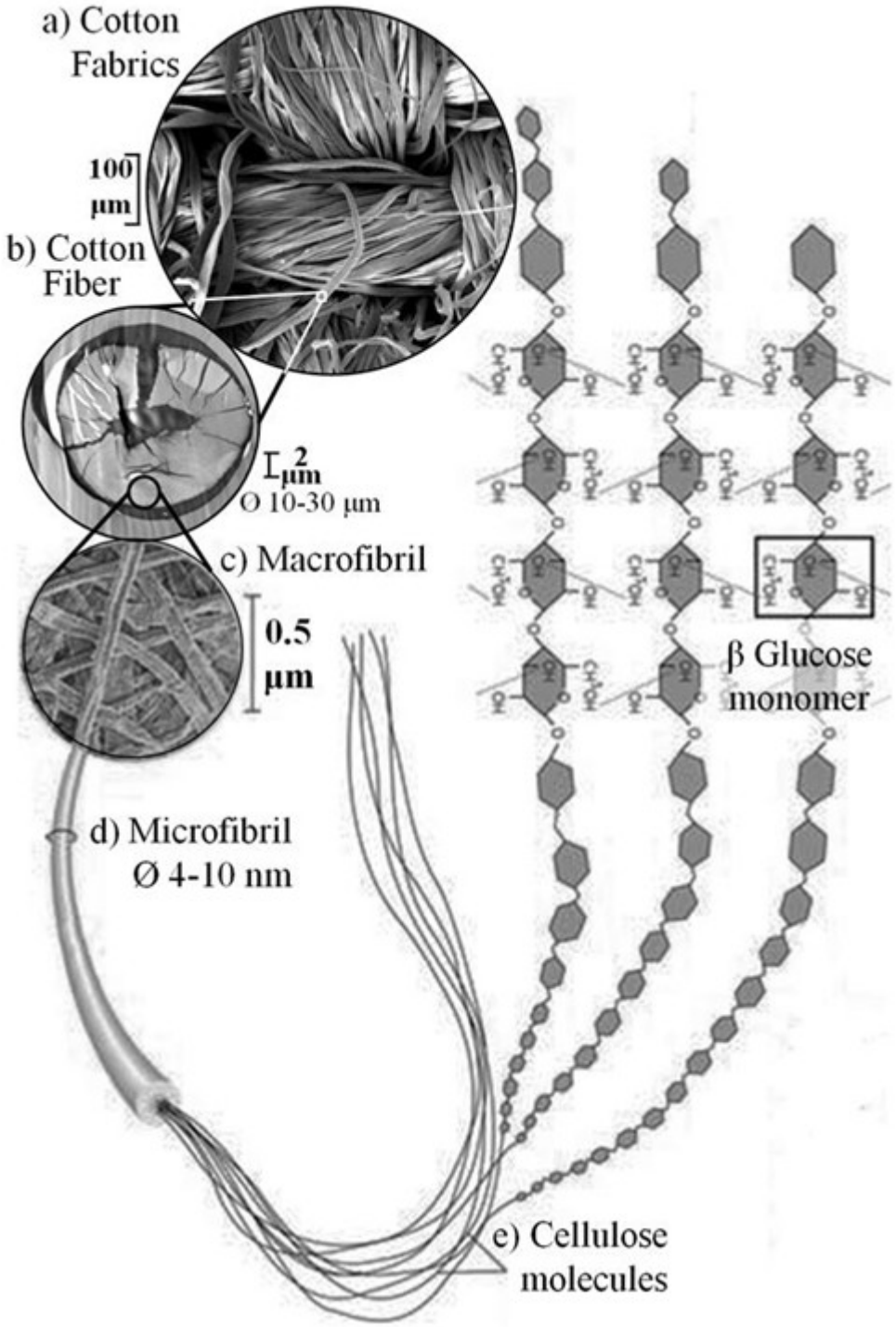

Figure 5.2 Essential schematics of cotton structure from mesoscopic to molecular dimension: (a) SEM image of Cotton Fabrics. (b) section of a single cotton fiber. Macrofibrils compose each fiber. (c) Each macrofibril is composed of bundles of microfibrils. One microfibril (d), in turn, is composed by bundles of cellulose chains (c).

5.1.2 Macrofibrils and Macropores

The cross section of the cellulosic portion of each cotton fiber is composed of 3200 circular macrofibrils(Figure 5.2.c) each with a cross sectional area of 0.16 micron^2 (160,000 nanometer^2) and a diameter of 0.45 microns (450 nm). These are arranged in a hexagonal close pack pattern with "macropores" at the intersections of each set of three macrofibrils. There are 2750 of these macropores in the cellulosic interior of each fiber. Assuming these macropores are circular, each would have a cross sectional area of 4450 nm^2 and a diameter of 75 nm. These macropores are easily accessible by liquid water which has a cross sectional area of 0.025 nm^2 (This was calculated from the fact that 18 cm^3 is the volume of one mole of water and the assumption that water molecules are very nearly spheres. If only these macropores in a kilogram of dry cotton were filled with water, 1 kilogram of dry basis weight cotton would contain 15 grams of water.

5.1.3 Microfibrils and Micropores

The cross section of each macrofibril is composed of 250 circular microfibrils(Figure 5.2.d) each with a cross sectional area of 600 nm^2 and a diameter of circa 30 nm (100-400 Å)[240]. These are arranged in a hexagonal close pack pattern with "micropores" at the intersections of each set of three microfibrils. There are 200 of these micropores in the interior of each macrofibril. Assuming these micropores are circular, each would have a cross sectional area of 20 nm^2 and a diameter of 5 nm. These are easily accessible by liquid water which has a cross sectional area of 0.28 nm^2 and a diameter of 0.3 nm[241, 242]. If only these micropores in a kg of dry cotton were filled with water, 1 kilogram of dry basis weight cotton would contain 1.5 grams of water.

5.1.4 Elemental Fibrils and Elemental Pores

The cross section of each microfibril is composed of 20 nearly circular elemental fibrils(Figure 5.2.e) each with a cross sectional area of 30 nm^2 (3000 Å^2) and a diameter of 6.2 nm (62 Å)[243]. These are arranged in a hexagonal close pack pattern with elemental pores at the intersections of each set of three elemental fibrils. There are almost 20 of these elemental pores in the interior of each microfibril. Assuming these elemental pores are circular, each would have a cross sectional area of 80 Å^2 and a diameter of 10 Å. These are hypothetically accessible by liquid water which has a cross sectional area of 3.8 Å^2 and a diameter of 3 Å. If only

these elemental pores in a kg of dry cotton were filled with water, 1 kilogram of dry basis cotton would contain 1.5 grams of water.

5.1.5 Crystal Fibrils and Crystal Pores

The cross section of each elemental fibril is composed of 20 cellulose crystals each with a cross sectional area of 146 $Å^2$ and a diameter of 14 Å. These are arranged in a hexagonal close pack pattern with crystal pores at the intersections of each set of three cellulose crystals[244]. There are 14 of these crystal pores in the interior of each elemental fibril. Assuming these crystal pores are circular, each would have a cross sectional area of 4.1 $Å^2$ and a diameter of 2.3 Å. These pores are not accessible by liquid water.

5.1.6 Cellulose Polymers and Polymers "Pores"

Cellulose crystals are composed of 5 cellulose polymer chains with a square, face centered orientation[245]. Each cellulose polymer has a cross sectional area of 32 $Å^2$ and a diameter of 3.2 Å. The degree of polymerization of cotton is 9,000-15,000[246]. The spaces between these polymer chains are less than 2 Å in diameter and are thus too small and too tortuous to be accessed by liquid water.

5.2 Distribution of Water in Cotton Fabrics

It is estimated that around 80% of water (on a dry clothes basis, the so called residual moisture content or RMC) is still retained in fabrics after spinning in the washer (at 800 rpm[247], and most of it (apart from the equilibrium moisture content which is around 7-5% at ambient conditions[248]) needs to be removed by drying. Since the packing density (i.e., the fraction of fibers) of yarns in textile is 40%, an RMC of 60% could be accommodated in the smaller intra-yarn pores which are made by the interstices between the fibers or inside the fibers themselves. Further support to this hypothesis is given by the capillary forces which act to keep water trapped in the smaller fabric pores even after centrifugation[16] (RMC is still 43% even after spinning at 1800 rpm[247]). So, it is essential to study the physics of drying at the pore network scale, because that is where most RMC is located from the beginning of the drying process.

Thus cotton can apparently hold about 80% of its own weight of water tightly enough to survive the washing machine. In addition it can hold water up to 5 times this amount between fibers, threads and yarns which is removed during the spin of

the wash cycle. Of the 80% carried over into the dryer, 56% does not have to diffuse through cotton to evaporate and thus dries fairly easily (free water). The remaining 24% which is held in the lumen and in small pores is harder to remove (bound water)[249]. The 5% of the bound water that is held in non-lumen pores and within a couple of nanometers of the cotton surface can be removed if sufficient heat is applied in the dryer but it returns when the cotton is exposed to normal temperature and humidity.

Caurie identify three types of bound water[250]. These are the type 1, most tightly bound primary water up to m_0 grams of molecules which have non-freezing and non-solvent properties (m_0 = 4.98%). The type 2 bound water starts from m_0 grams up to nm_0 grams (being n = 4.52 for cotton). These molecules equal to ($nm_0 - m_0$) grams are bound weakly with non-freezing but have solvent properties. The type 3 bound water are the ($m_0^2 - nm_0$) grams of loosely bound water molecules with solvent and modified or limited freezing properties. These type 3 bound water molecules have full solvent and normal freezing properties[251]; an intensive literature search were done for identifying the location of Types 1-3 water, of the water that is hard to remove in the dryer, and of the water that is not removed by the spin cycle but is relatively easy to remove in the dryer. In Figure 5.3.a a schematic of cotton fabric section is proposed to highlight arrangement of yarn in space.

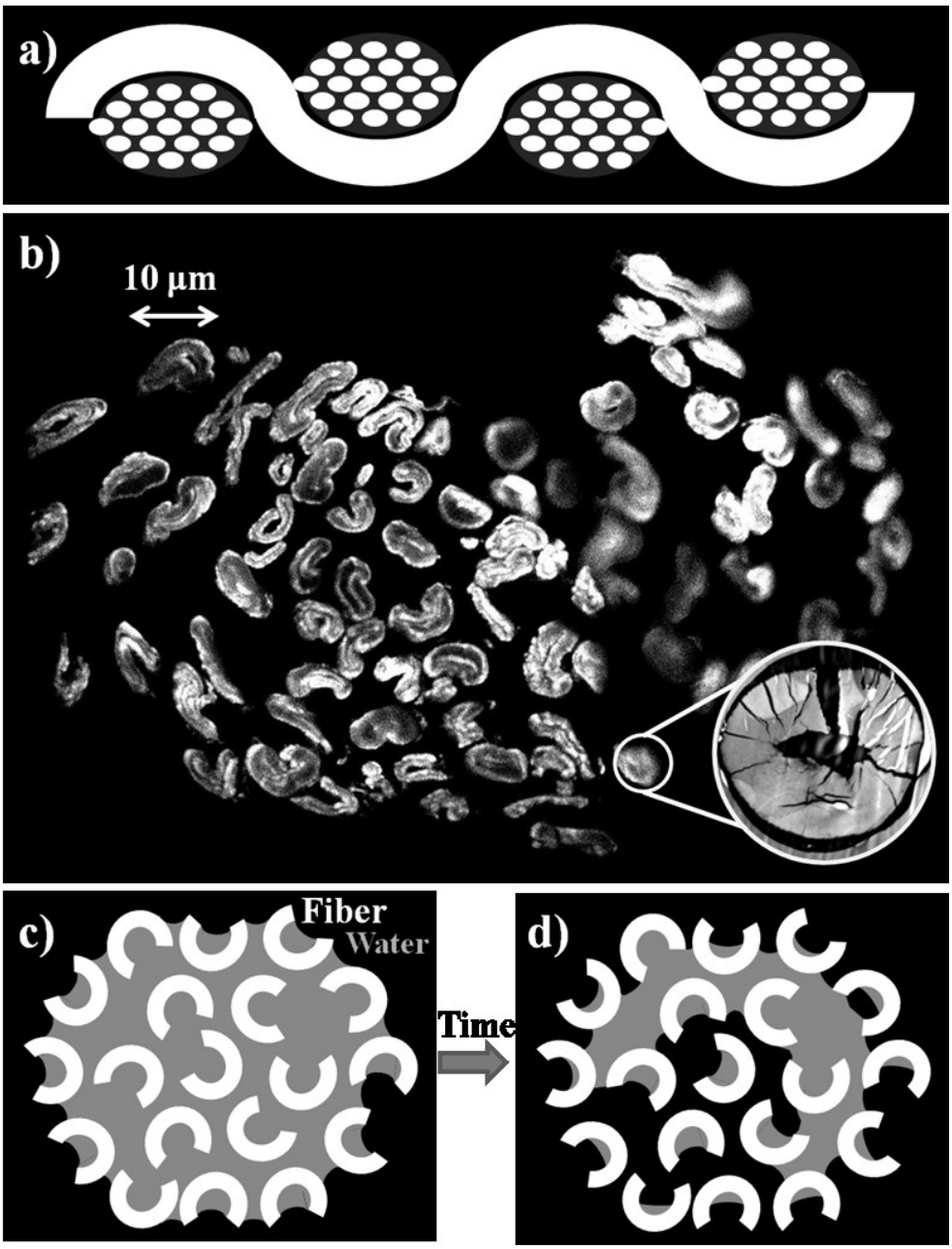

Figure 5.3 In a) a schematic of a section of cotton fabric is proposed to highlight yarns arrangement in space. In b) a microtome slice of a single cotton yarn in confocal microscopy show the fibers constituting it. In the inset single cotton fiber section as shown in fig. 5.2.b. In c) and d) a scheme represent how water evaporates from fibers.

In Figure 5.3.b a single cotton yarn structure were shown to highlight the high porosity of this material.

5.2.1 Source of Type 1 Water

Cotton normally contains about 5% of Type 1 water and another 17% of Type 2 water and 2% of Type 3 water[249, 252]. We can surmise from the previous section

that the 1.5% water in the crystal pores of radius 5 Å are part of the Type 1 water. The Laplace equation suggests that such a narrow capillary would pull a column of water 40 kilometers long. There is no known combination of treatments that could reduce this to below 3 cm which would be necessary to have an effect on the water held in these pores. The next larger pore is the micro-pore with a radius of 2.4 nm. All of the 1.4% water in these pores is also Type 1. The Laplace equation confirms that pores of this diameter would pull a column of water nearly 9 kilometers long which again is expected to be untouchable.

The Macro-pore has a radius of 0.5 μm. All of the 1.5% water in these pores is also likely to be Type 1. The Laplace equation suggests that pores of this diameter could pull a column of water about 56 meters long. In the typical wash one could expect to lower the surface tension by a factor of 2 or 3 and to have a spin cycle of 100 to 300 g's. The g's in the spin cycle must be reduced by a factor of 2 to account for the random orientation of the pores with respect to the g vector. Even the most aggressive combination of surface tension lowering and spin speed would not reduce the column of water sufficiently to affect even the longest fibers. Thus water in these macro-pores is untouchable.

If the above assumptions for the location of Type 1 water are correct, we have accounted for 4.5% of the reported 5%. A likely source of the remaining 0.5% is the water in intimate contact with the cellulose surface of the fibers. If one assumes that water within 2 nm of the surface is fairly tightly bound to the surface, it amounts to 0.5%. This accounts for all of the reported 5%.

5.2.2 Source of Type 2 and 3 Water

The next larger pore is the lumen with a radius of 7.5 μm. The Laplace equation suggests that such pores could pull a column of water about 2.5 meters long. Given typical combinations of surface tension lowering and spin speeds (reduced by half for orientation), almost 90% the water contained in the lumen would survive into the drying phase. Thus 19% of the 21% moisture that resides in the lumen would survive to the dryer. Thus the lumen is the likely location of the Types 2 and 3 water.

5.2.3 Source of "Hard to Remove" Water

Thus all 24 to 25% of the Type 1, 2 and 3 water, which is virtually all contained within cotton fibers, were accounted. In Figure 5.3.c and d a scheme represent how water can be trapped in fibers during evaporation, after that all "free" water evaporates. Fibers are the likely sources of the 20 to 24% "hard to remove" water that is distinguished by a falling rate of evaporation in the dryer. This water is hard to remove not only because it is more tightly bound to the cellulose surface than bulk water but also because most of it has to diffuse through the cellulose fiber wall to be removed.

5.2.4 Water Carried Over from Washer to Dryer

The next problem is to understand the source of the 80% water that survives the wash and needs to be dried. The above analysis seems to assure us that Types 1, 2 and 3 water survive into the dryer and is likely the moisture that is removed during the falling rate of evaporation. Thus we can account for 24% of the 80%. From photomicrographs we can ascertain that the space between cotton fibers is 20-30 μm. These "pores" would also trap water via the Laplace mechanism but this water would be expected to be easier to remove in the dryer since it does not have to diffuse through cellulose to do so. There are about the same number of these pores as lumens and because of their larger radius they contain almost twice the water. Assuming 80% of this water survives the wash gives us about 34% extra fibrillar water that when added to the Types 1-3 water gives a total of 58% which is reasonably close to the stated 60%.

In conclusion cotton can apparently hold about 80-60% of its own weight of water tightly enough to survive the washing machine. In addition it can hold water up to 5 times this amount between fibers, threads and yarns which is removed during the spin of the wash cycle. Of the 80% carried over into the dryer – 56% does not have to diffuse through cotton to evaporate and thus dries fairly easily. The remaining 24% that is held in the lumen and in small pores is harder to remove and correspond to the total bound water value suggested by Caurie for cotton[250]. The 5% of water that is held in non-lumen pores and within a couple of nm of the cotton surface can be removed if sufficient heat is applied in the dryer – but it returns when the cotton is exposed to normal temperature and humidity.

5.3 Surfactant retention in fabrics after rinsing

The present section focuses on the dilution of detergent during clothes washing. Here is exposed a calculation about the concentration of detergent during washing cycle, considering two cases: the best situation, in which clothes fibers do not retain any detergent, and the worst situation, in which clothes retain all the detergent that pass through the fibers.

The following calculation can be applied to all different kind of laundry washer. This paper takes in account the mean water per load value of front load and top load models, to give a generic evaluation; this value for standard cotton program at 40°C consists in 50 liters, 25 liters for the first wash and the other 25 for the second wash. The average washing machine uses less than 10 liters of water for every kilogram of cottons it washes. A 7kg capacity machine loaded at 80% is considered (load weight 5,6 kg). To calculate the amount of water inside the fibers, density of cotton and the void volume fraction inside clothes have been investigated (see table 5.1).

$$Load\ Volume = Load\ Density * Load\ Mass \quad (36)$$

$$Moisture\ Content = Void\ Volume = 70\%\ of\ Load\ Volume \quad (37)$$

Table 5.1: Mass and volume values in laundry.

Load Mass	80% of 7kg	5600 g
Load Density		1 g/cm^3
Load Volume	Density*Mass	5600 cm^3
Void Volume	70% of Load	3920 cm^3
Fabric Volume	30% of Load	1680 cm^3

The last information needed is about the detergent concentration. Again a mean value can be carried out from the manufacturer's suggested soap amount (50 ml). So the detergent concentration is about 0.2% in the first washing. In this condition we examine two cases:

*The best situation, in which clothes fibers do not retain any detergen*t.

The concentration at the end of the first wash is again 0.2%. Hence, in 4 liters of moisture retained in the clothes after the first wash there are 8 ml of detergent. The latter is diluted in the second wash to a concentration of 0,03% (8ml in 29l), so in 4 liters of moisture there are 1,2 ml of detergent. After rinsing we can consider that 80% of moisture remain in clothes, so there are 3,2 liters containing 1 ml of detergent.

The worst situation, in which clothes retain all the detergent through the fibers.

According to Kim and Hsieh[253] and Schott[254], cotton fibers retain 0.3% of detergent; it means that in the 4 liters of moisture absorbed by the loads, since detergent concentration is 0.2% (i.e., less than 0.3%) all the detergent stays in the fibers, even after the second wash. Rinsing leaves 80% of moisture from clothes, so we have 3,2 liters of moisture with 6 ml of detergent. During drying only water evaporates from clothes, so the concentration grows while water content decreases. We can suppose that, at a value of 10% of the moisture content inside the clothes, the detergent concentration grows to 2%.

5.3.1 Corrective parameters for Temperature and RH

Drying experiments in cotton fabrics, as presented in section , have a duration of several hours and were carried out in different boundary condition, due to the season and the weather of the day in which were run out. Figure 5.4 show how RH and temperature changes over a day; similar changes occurs over an year with the change of seasons. So long, all the experiments shows a different drying rate value, due to the boundary condition of RH and temperature.

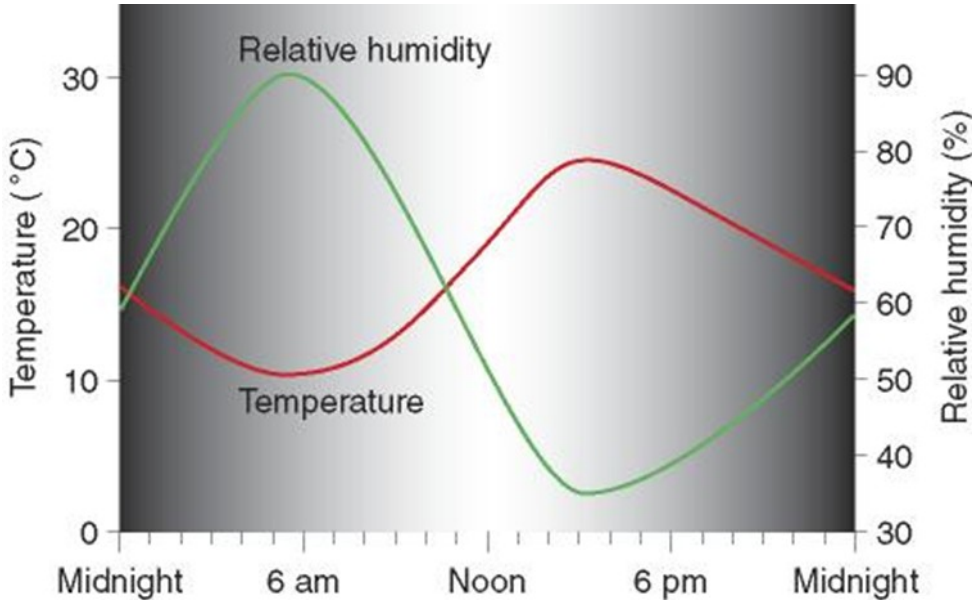

Figure 5.4 Relative humidity and temperature changes during the day. §Courtesy of the American Meteorological Society

In this section a corrective parameter to overrun this problem were proposed.

When two experiments (1 and 2) having different boundary conditions need to be compared, one of them (1) was taken as a reference while the other one (2) was multiplied point by point by the corrective parameters.

Corrective parameters:

$$K_T = \lambda^1_{ev} / \lambda^2_{ev} = T_1/T_2 \ [K/K]$$

$$K_{RH} = RH_1 / RH_2$$

$$K = K_T * K_{RH}$$

where λ^N_{ev} is the latent heat of evaporation, T_N is the mean temperature expressed in Kelvin, and RH_N is the mean relative humidity for the experiment N in the time interval considered. This linear relation was verified for small changes in temperature (20-27 °C) and relative humidity (34-51%). In Figure 5.5 the drying curves for DEMI water in cotton before and after the scaling were reported.

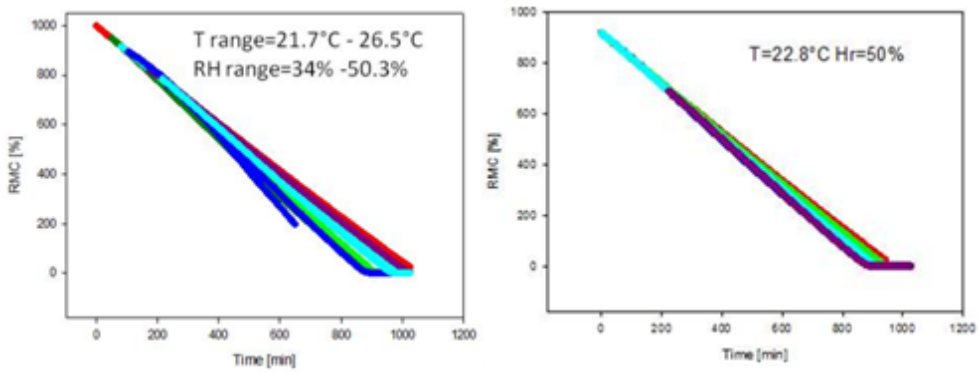

Figure 5.5 Drying curves of water in cotton fabrics. Raw data on the left (T and RH range for all the experiments) were compared with data scaled by using corrective parameters, on the right (T and RH of the experiment used as reference).

After scaling, experimental curves were used to calculate a mean curve; standard deviation was found and represented in graph by error bars as shown in Figure 5.6.

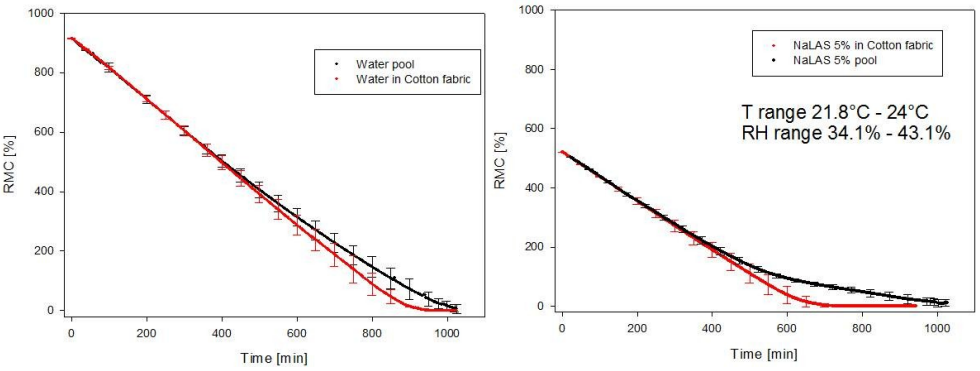

Figure 5.6 Mean drying curves of water in cotton fabrics (red) and in a Petri dish (black), on the left; same mean drying curves for NaLAS 5% in water (T and RH range for all the experiments), on the right.

As can be noticed observing Figure 5.6, the data scaling for the NaLAS 5% solution was not necessary, so the room condition ranges was reported. There, due to the consistent amount of surfactant used in the solution, the RMC formula (10) were slightly changed, considering the bone-dry weight w_i as a sum of the dry cotton weight with the NaLAS weight. Again the present data confirms the previous results that solutions in a cotton fabric dry faster than in a Petri dish.

5.4 Determination of the Critical Moisture Content

The drying process in cotton fabrics, as discussed in section 2.3.1, shows two main regimes identified by the change in drying rate of the drying curve, as can be seen in Figure 5.7.

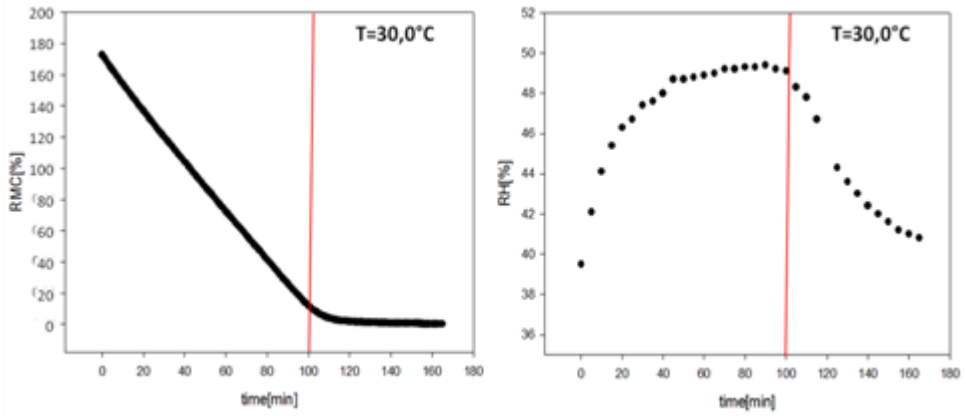

Figure 5.7 Drying curve, on the left, compared with the Relative Humidity changes in time, on the right.

The two periods of a fabric drying cycle has been identified, characterized by drying rate changes. After the preheating, there is a constant rate period followed by the falling drying period. The Critical Moisture Content θ_k at the beginning of the falling drying period will be the separating point between the two periods. A big issue in this work was to develop a method to identify the critical point that separates the Constant Drying Rate period by the Falling Drying Rate period. The first approach regards the observation of the RH variation near the sample in time; as can be seen in Figure 5.7, when the drying rate falls because of the sensible reduction of the water content, the RH value goes down. This evaluation method provides with θ_k equal to 10% wt and is not dependent by the boundary conditions of temperature and RH. It can be noticed that the RH decreasing is not instantaneous and so this evaluation can't give a precise value of the regime change. Thus the values of θ_k were identified by plotting the instantaneous drying rate versus RMC or versus time, as shown in Figure 5.8.

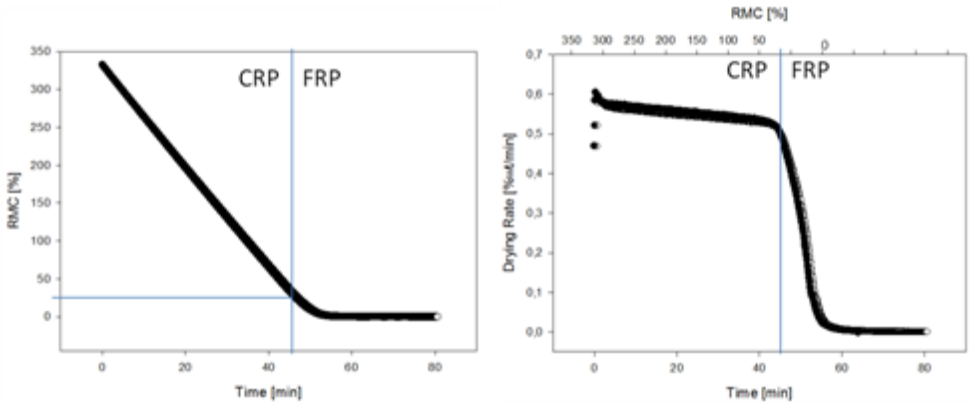

Figure 5.8 On the left: typical drying curve. On the right: plotting of punctual drying rate versus time and RMC double axis for cotton fabric.

The θ_k can be identified from the curve as shown in Figure 5.8 at the point of dramatic decrease of the drying rate. The determined value of θ_k for fabric samples is comprised between 24 and 40 % depending on the boundary conditions. In the mean drying curves of water and NaLAS 5% in cotton fabric are showed.

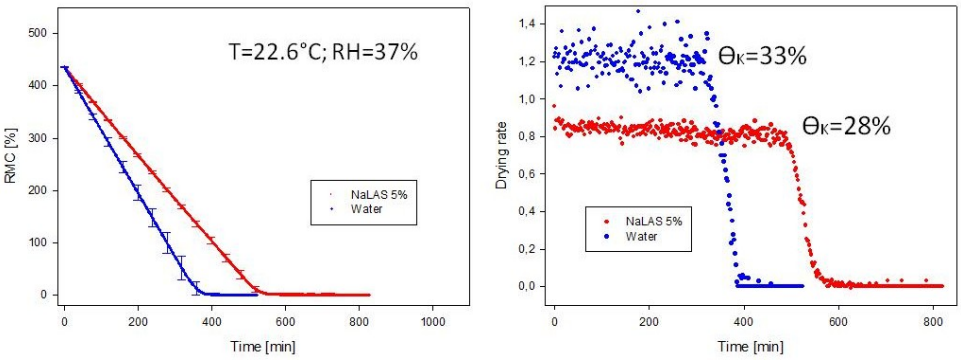

Figure 5.9 On the left: mean drying curves in cotton fabrics as reported in Figure 5.6. On the right: punctual drying rate versus time for the curves on the left.

The θ_k values were calculated for the mean curves and for the raw data curves at different environmental conditions. Plotting all experimental curves for water in a RMC range from the θ_k value to the end of drying, as reported in Figure 5.10, show that all data collapse on the same curve in the falling rate period. In the same figure, the falling rate phase of some surfactant solutions at different concentration is shown, highlighting that there is a collapse also for surfactant concentrations below the 1%, while the 5% concentrated solutions has a different curvature.

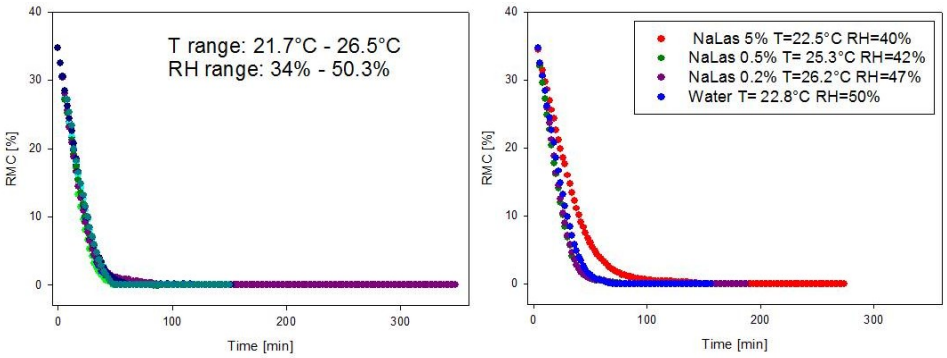

Figure 5.10 On the left: water drying curves in a cotton fabric at different boundary conditions in a RMC range from θ_k to 0. On the right: same drying curves for different surfactant solutions.

For better understand this change in curvature that happen in the cotton fabric sample, the drying curve of the lone 5% concentrated solution were compared with water, as shown in Figure 5.11.

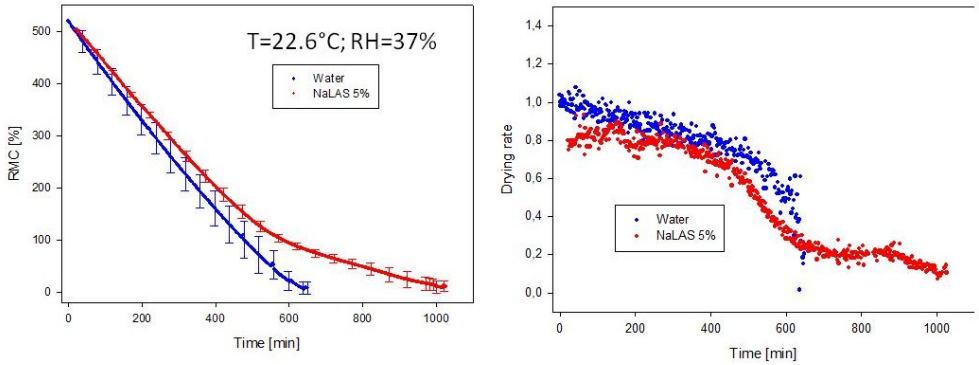

Figure 5.11 On the left: mean drying curves in Petri dishes as reported in Figure 5.6. On the right: punctual drying rate versus time for the curves on the left.

While drying proceeds, surfactant concentration increases. Effect of concentration on surfactant structures formations can be seen in Figure 3.2. A correlation between the drying rate and the surfactant concentration can be observed in Figure 5.12.

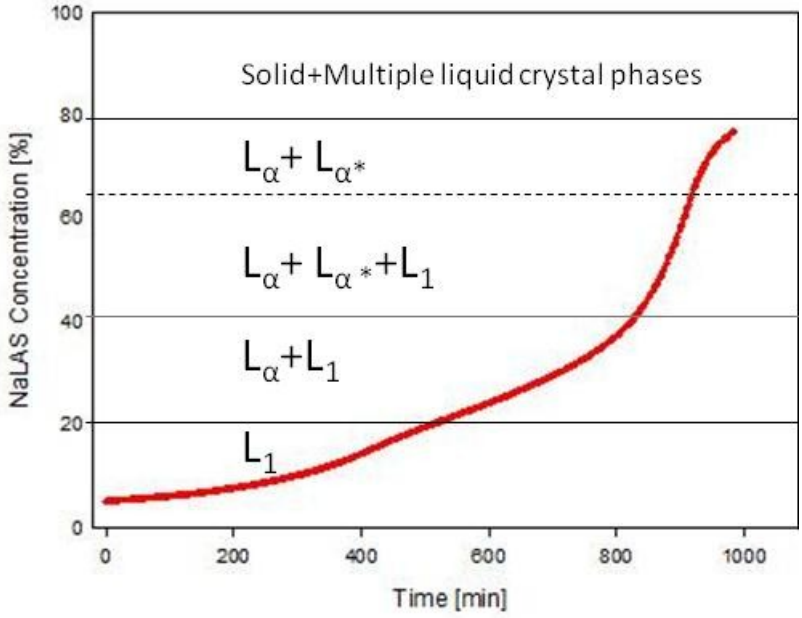

Figure 5.12 Na LAS concentration increases in time during drying.

Starting from a concentration of 5%, a first change in curvature can be seen near the 20% value, at which the first lamellar phase L_α appears; the next change can be noticed near the 40%, where probably multiple lamellar L_{α^*} and micellar L_1 phases organizes one with the others; near the 65% value only lamellar phases are present; finally, as expected, the drying ends near the 80% value, before the concentrated region, were the 20% of water present is trapped between the surfactant structures.

5.5 Correlation between capillary drying and cotton fabrics drying

The estimation of the drying rate of a liquid evaporating inside a capillary tube is made observing a time lapse of images and measuring the meniscus shifting over time; it gives back a drying rate value as a fraction between a length and a time. On the other hand, the drying rate of a liquid evaporating inside a cotton fabrics, placed in a Petri dish, was estimated by monitoring the weight loss of the sample over time. In order to connect these two values, a conversion parameter is needed. The capillary tube sample is taken in account, being the simplest of the two systems. The boundary conditions considered are a temperature value of 25°C and a relative humidity value of 40%. A capillary tube is basically a cylinder with defined radius *r*. Considering now a unitary length *h* along which the meniscus moves with a certain drying rate in a defined time, the cylinder volume can be determined

avoiding to mention the complex meniscus shape. The equation to calculate the cylinder volume is shown in Figure 5.13.

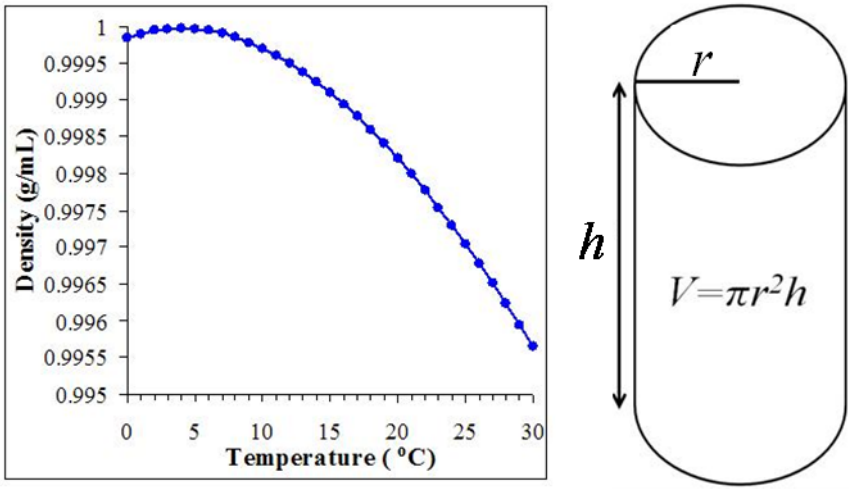

Figure 5.13 On the left: water density changes with temperature; on the right: cylinder geometrical parameters and volume formula.

So, in a capillary tube having the diameter of 100 μm (0.1 mm) the meniscus moves 1 mm. The volume of liquid evaporated is 0.00785 mm^3. If the evaporating liquid is water, which at room temperature (25°C) has a density of 997.05 kg/m^3 ($9.97x10^{-4}$ g/mm3), the water weight that corresponds to the volume of liquid evaporated is equal to $7.83x10^{-6}$ g; a change of ±5°C in temperature gives a change of $\pm 0.01x10^{-6}$ g; the value at 37°C is equal to $7.80x10^{-6}$ g, with a density value of 993.37 kg/m^3, as shown in Figure 5.13.[255] Taking into account the previous explanation, in a 0,1 mm diameter capillary filled by water, $7,88x10^{-6}$ g (1.006 mm) of water evaporates in 82,87 minutes, giving a drying rate of $9,51x10^{-8}$ g/min. The drying rate in a cotton fabrics sample having the apparent area of a 35 mm diameter disc (109,96 mm^2) is $2,65x10^{-3}$ g/min. The ratio C_{Dr} between the drying rate of the cotton fabrics sample and the drying rate of the capillary tube is $C_{Dr} = 27918$.

In order to confirm this value, the cotton fabrics in the Petri dish is imagined as it will be composed by a defined number of 0.1 mm diameter capillary tubes; the capillary tubes have a length of 3 millimeters, equal to the depth of the cotton fabrics, like if the tubes were placed vertically one near the other, as schematized in Figure 5.14.

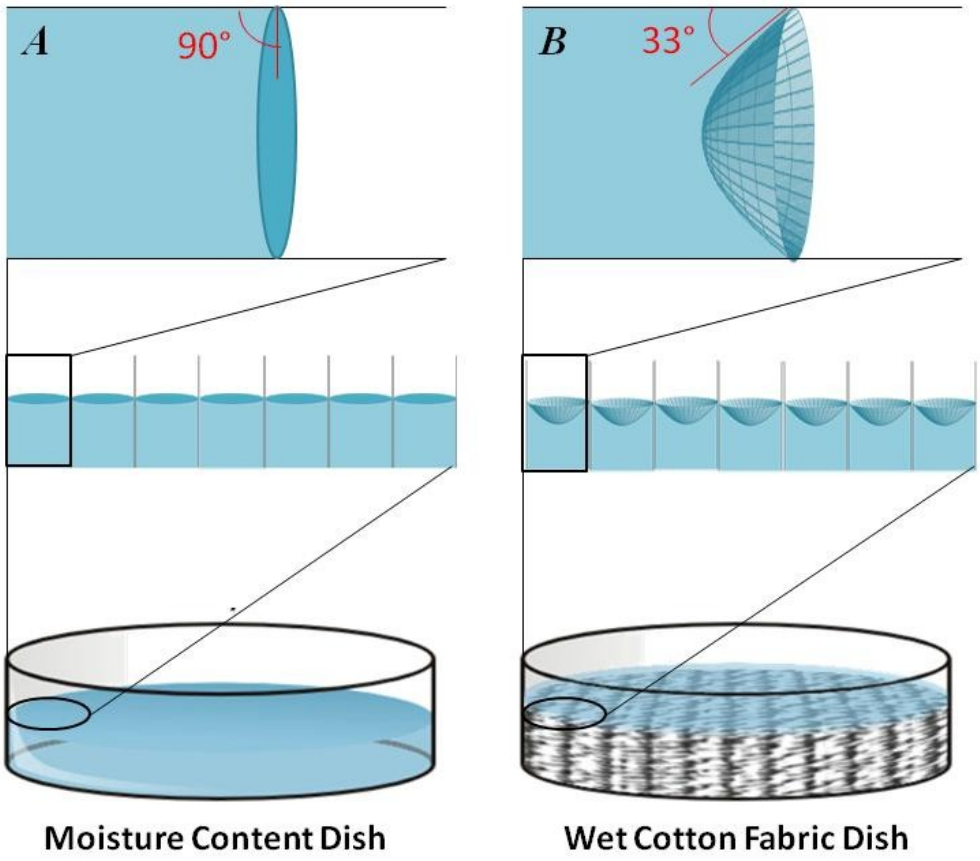

Figure 5.14 In A) a Petri dish filled with water is imagined as it will be composed by a defined number of micro-capillary tubes, each one having a meniscus with a contact angle equal to 90° to reproduce the flat surface; in the same way, in B) a wet cotton fabric is imagined to be composed by a number of micro-capillary tubes with a contact angle of 33°.

So the ratio between the cotton fabrics water content (0,66 g) and the water contained in a single capillary tube ($2{,}35 \times 10^{-5}$ g) would give back a value C_W, equal to the number of capillary tubes that compose the cotton fabrics: $C_W = 28169$. Finally, we can come out with a scaling parameter between the cotton fabrics and the capillary tube, equal to $C = C_{Dr} = C_W = 28000$.

5.6 The role of surface in drying process

5.6.1 Meniscus Surface Evaluation in a Capillary Tube

The meniscus of a liquid within a capillary tube may be approximated with a geometric surface called elliptic paraboloid. Once calculated the surface of that paraboloid, the main goal is to evaluate how this surface changes with the modification of the contact angle between the liquid and the capillary wall. The equation[256] to calculates the surface is as follows:

$$S = \int_0^{2\pi} \int_0^h dS = \frac{\pi}{6}\frac{r}{h}[(r^2 + 4h^2)^{3/2} - r^3] \quad (37)$$

In this formula, the area of the base (the upper disc closing the surface) is not included. Is important to notice that the surface area *S* is equal to the base area *B* for $h = 0$ or, in other words, when the contact angle is 90°. The variables in this equation are the radius ***r*** and height of the meniscus ***h***; these value can be calculated from the equation of the parabola with which the contour of the meniscus were approximated. The radius calculation is particularly simple since it's constant along the capillary; the height instead can be measured directly being the distance between the center of the paraboloid and the contact points of the meniscus with the capillary wall. These values can be easily calculated with the help of a computational software. Once the contact angles were calculated, the next step is calculate the meniscus surface for each angle, as shown in Figure 5.15.

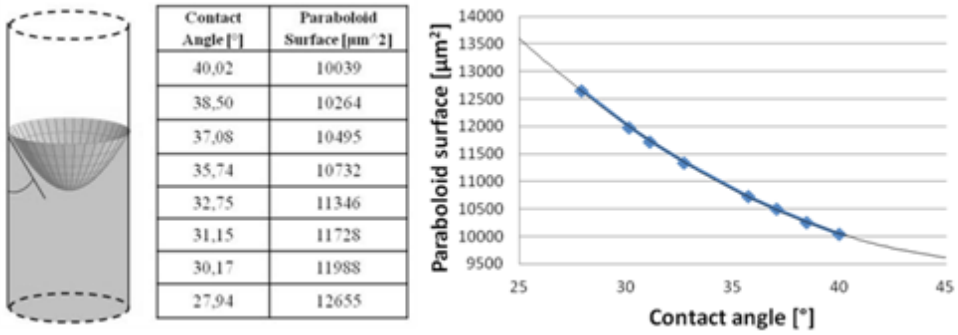

Contact Angle [°]	Paraboloid Surface [µm^2]
40,02	10039
38,50	10264
37,08	10495
35,74	10732
32,75	11346
31,15	11728
30,17	11988
27,94	12655

Figure 5.15 3D meniscus shape and surface changes with contact angle variations.

The paraboloid obtained with a contact angle of 30° have an area 42% larger than the base area corresponding to a contact angle of 90°. A decrease of the angle increases the surface of the paraboloid. Oscillations around 30° angle of 1° means a surface increase of 260 µm^2 (2-3%). The higher the contact angle, the lower the increase in terms of surfaces, as can be appreciated from the curve on the right in Figure 5.15.

5.6.2 Surfactant effect on Meniscus Surface

The present section illustrates the results of a set of experiments in order to evaluate the changes in drying rates of a solution inside a capillary tube modifying the solutions composition. In particular, three NaLAS solutions at different concentrations were tested. Using a time lapse microscope, the drying of the liquid meniscus inside a silica capillary tube (100 µm diameter) at a constant temperature

of 38 °C were observed; the drying rates were evaluated following the meniscus receding in time and the results are resumed in Figure 5.16.

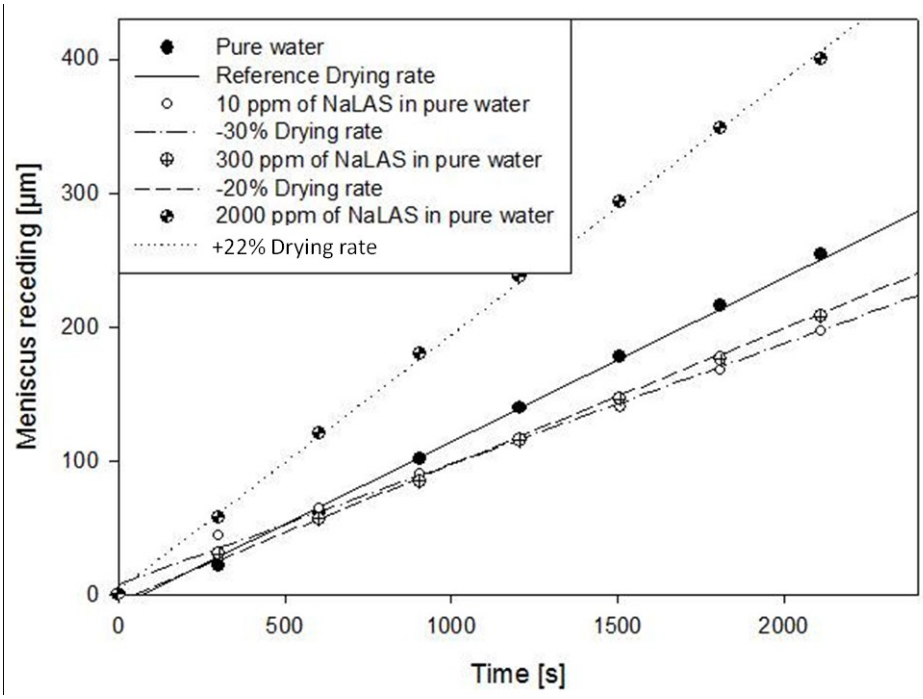

Figure 5.16 Drying rate changes in 100 µm capillary tubes depending on NaLAS surfactant concentration.

As a fact is necessary to consider that the Critic Micellar Concentration of the NaLAS is ~480 ppm. Taking the pure water test as a reference, it can be observed that a really low surfactant concentration gives a decreasing of the drying rate of the 30%. This decreasing effect fall off but persists at a higher concentration below the CMC value. In the solution having a concentration 4 times higher the CMC, the increase of the drying rate is about the 22%; So the micellar structures appears to be the cause of the drying rate increase. A typical experiment is shown in Figure 5.17.

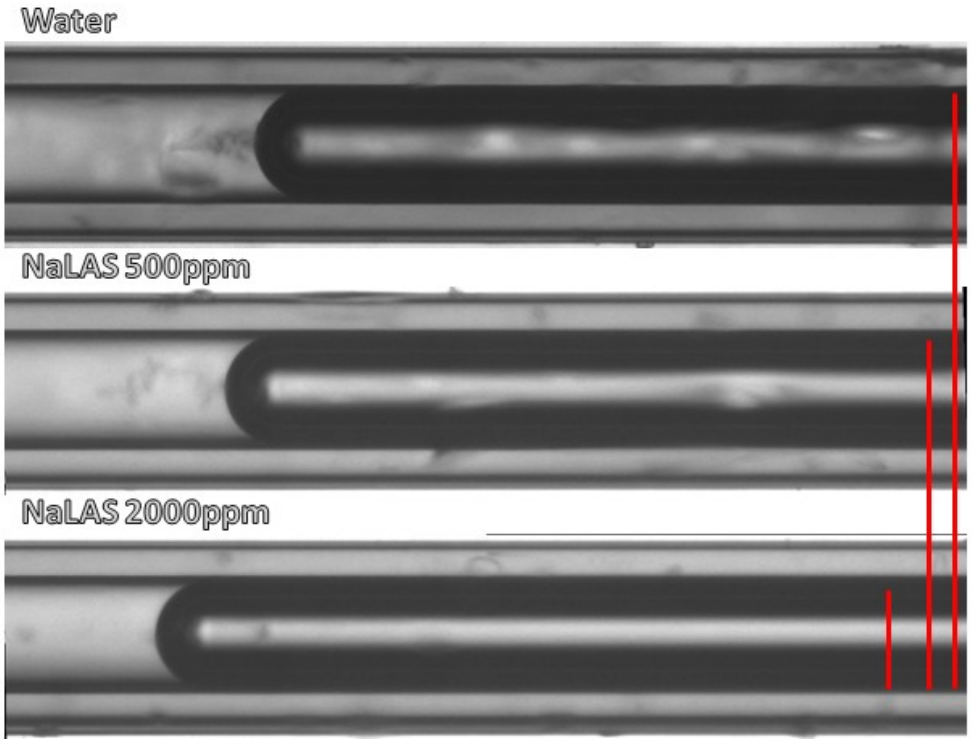

Figure 5.17 Time lapse microscopy observation: Drying rate changes in 100 µm capillary tubes depending on NaLAS surfactant concentrations. Red bars underline the final difference in drying rates.

For what has been told in the previous sections, a correlation between contact angle, meniscus surface and drying rate has been observed (Figure 5.18).

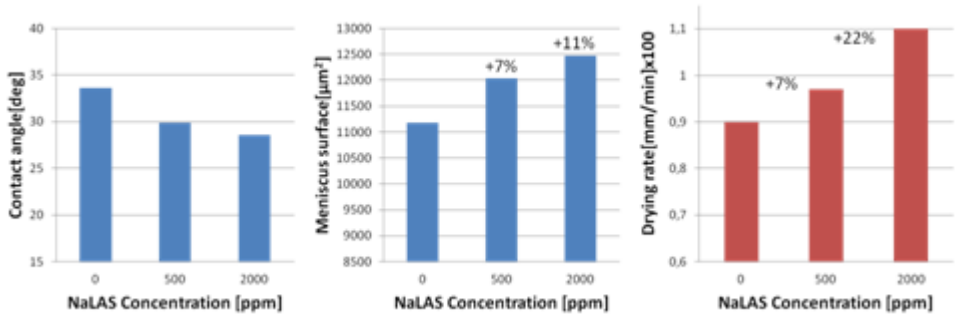

Figure 5.18 NaLAS concentration, contact angle, meniscus surface and drying rate correlation.

So, for small value of void degree, the increase of surfactant concentration generates a decrease in contact angle that means a larger meniscus surface; that provide a larger interfacial area that make the liquid drying faster. Evaporation rate decreases with the increase of the void degree. Evaporative regime turns in a pure

diffusive regime with the increase of the void degree because of the increase of vapor concentration near the meniscus; that explain also why surfactants has no effect on evaporation process, as can be seen in Figure 5.19.

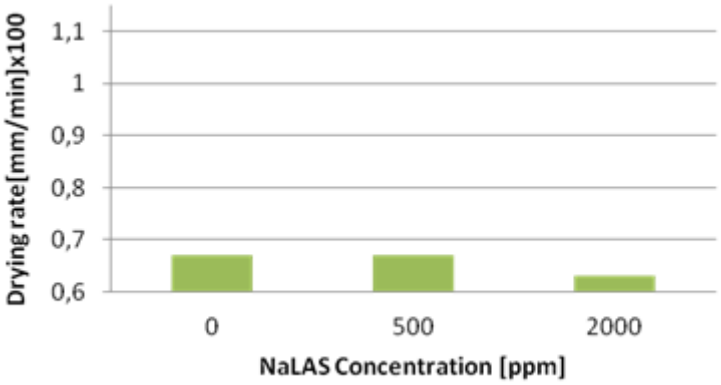

Figure 5.19 Drying rates for different NaLAS concentrations in the same conditions of Figure 5.18.

It proves that the drying rate for low void degree is related to the interfacial area. Results show that NaLAS affect the interface by lowering the contact angle; the gain in surface area that results, increase the evaporation rate. It should be specify that the considered system is in semi-equilibrium conditions, being the contact angle at a static value, not a dynamic value.

5.7 Marangoni Effect

Marangoni effect, as mentioned in section 2.3.2.1, has a role in the drying process, due to the concentration gradient that generates in presence of surfactants. Rhodamine-B in water acts like a tensioactive molecule; like any surfactant, has a Critical Micellar Concentration, equal to 3 ppm in water. The huge difference in CMC between Rhodamine-B and NaLAS is due to the molecule length: being Rhodamine-B a smaller molecule, it has less steric obstacles in organizing in structures.

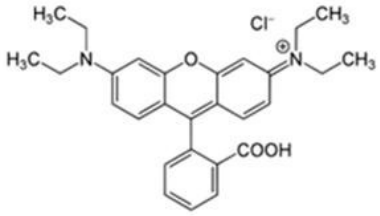

Figure 5.20 Rhodamine-B chemical structure.

Micro-fluidic visualization techniques were used to investigate the concentration gradient near an evaporating meniscus. Similar procedures can be find in literature.[257-259] A Rhodamine-B/water solution (0.1% wt.) were observed by Confocal microscopy in a 100 μm diameter capillary tube. Figure 5.21 shows a higher concentration of the tensioactive molecules in the meniscus region, due to the temperature gradient generated by the drying process, being the concentration directly proportional to the intensity of the fluorophore emission.

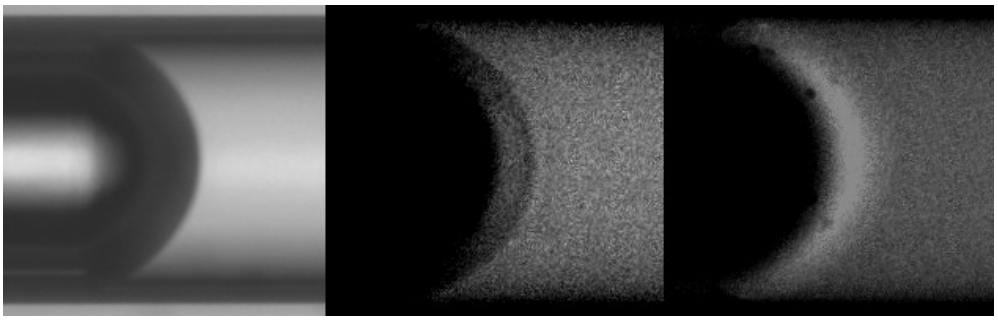

Figure 5.21 Concentration gradient visualization in a capillary tube.

6 CONCLUSIONS

"The greatest ideas are the simplest."
W. Golding

6.1 Summary

In conclusion this project is addressed to improve the current understanding of the cloth drying process with a potential impact on energy saving in home laundering. The results of this project could be also relevant for the commercial laundry industry and to clothing and fabric manufacturing. The project approach was to identify limiting steps in the drying process of cotton fabric. The rate limiting transformations of water removal were experimentally investigated by measuring the amount of residual moisture in a cotton swatch preliminarily soaked in water and by optical observations through confocal microscopy and reflected light imaging. Our results show that drying is faster in a cotton fabric as compared to a dish filled with water with the same area of the fabric during the constant rate phase (CRP). This somehow unexpected finding can be explained by the increased water-air interfacial area in the swatch due to the presence of the cotton fiber microstructure. Therefore, the area for mass transport is larger in the swatch than in a flat water surface, thus increasing the drying rate. CRP drying rate in fabrics is enhanced by surfactants in a concentration-dependent way. Both these effects can be explained by a decrease of the contact angle and an increase of the interfacial area induced by the surfactant as shown by a single capillary model. In the falling rate phase (FRP) all the drying curves overlap showing negligible effects of surfactants on drying rate. Both CRP and FRP can be qualitatively explained in terms of a porous medium description of fabric microstructure by considering the yarn as the base element. Moreover, evaporation in a porous media can be modeled, considering a single pore, with a capillary tube, void degree being a controlling parameter in the evaporation process. In evaporative regime, interface area is a controlling parameter of evaporation process and surfactants in diluted conditions can increase evaporation rate. In the near future the key role of temperature and RH will be investigated. This work provides an explanation of the limited increase of drying rate obtained by addition of surfactants; the main conclusion is that interfacial agents capable to increase the water surface area in the

fabric should be selected in order to speed up the drying process (rather than using surfactants in order to modify water-fibers interactions).

6.2 Future Work

Experiments with some instruments, like the TAM, were just at the beginning and much more can be done testing other textile. Time-lapse confocal microscopy can be used to map the water surface in a yarn in order to come up with a more quantitative description of the drying process. Other additives (salts, hydrogen bond breakers) can be tested to improve drying in the falling rate region. The fundamental understanding developed in this work can be applied to other relevant problems where a material exhibiting a porous microstructure interacts with a liquid phase. Examples of these applications include packaging and powder stability, interactions between detergents and (stained) fabrics, interactions between body parts (hair, skin) and commercial products.

7 BIBLIOGRAPHY

1. Might, M., The illustrated guide to a Ph. D. *Texte librement adapté, Images sous licence Creative Commons Attribution-NonCommercial* **2010**.

2. Golden, J. S.; Subramanian, V.; Irizarri, G. M. A. U.; White, P.; Meier, F., Energy and carbon impact from residential laundry in the United States. *Journal of Integrative Environmental Sciences* **2010,** 7, (1), 53-73.

3. Bendt, P. In *Are We Missing Energy Savings in Clothes Dryers?*, ACEEE Summer Study on Energy Efficiency in Buildings, 2010; 2010; pp 42-55.

4. Nipkow, J.; Bush, E. *Promotion of energy-efficient heat pump dryers*; Swiss Agency for Efficient Energy Use (S.A.F.E.), Topten International Group: 2009.

5. Ball, J., Six products, six carbon footprints. *Wall Street Journal, March 1* **2009**.

6. Werle, R.; Bush, E.; Josephy, B.; Nipkow, J.; Granda, C. *Energy-efficient heat pump driers – European experiences andefforts in the USA and Canada*; 2010.

7. Trigg, A., White Knight gas tumble dryer. In ***Whitegoodshelp***, 2008; Vol. 2014.

8. Trigg, A., The world's first A rated Condenser Dryer wins prestigious Environmental award. In *whitegoodshelp*, washerhelp, Ed. 2008; Vol. 2014.

9. Hustvedt, G.; Ahn, M.; Emmel, J., The adoption of sustainable laundry technologies by US consumers. *International Journal of Consumer Studies* **2012**.

10. Hustvedt, G., Review of laundry energy efficiency studies conducted by the US Department of Energy. *International Journal of Consumer Studies* **2011,** 35, (2), 228-236.

11. Coons, R., Soaps and detergents: Consumers remain cautious. In *chemweek's lab*, Chemical, I., Ed. IHS Chemical Week: 2014.

12. Richter, T. *Energy Efficient Laundry Process*; General Electric Company (US): 2005.

13. Mao, A.; Luo, J.; Li, Y.; Luo, X.; Wang, R., A multi-disciplinary strategy for computer-aided clothing thermal engineering design. *Comput. Aided Des.* **2011,** 43, (12), 1854-1869.

14. Strumillo, C.; Jones, P. L.; Zylla, R., Energy Aspects in Drying. In *Handbook of Industrial Drying, Third Edition*, CRC Press: 2006.

15. Prat, M., On the influence of pore shape, contact angle and film flows on drying of capillary porous media. *International Journal of Heat and Mass Transfer* **2007,** 50, (7-8), 1455-1468.

16. Chauvet, F.; Duru, P.; Geoffroy, S.; Prat, M., Three Periods of Drying of a Single Square Capillary Tube. *Physical Review Letters* **2009,** 103, (12).

17. Shaw, T. M., DRYING AS AN IMMISCIBLE DISPLACEMENT PROCESS WITH FLUID COUNTERFLOW. *Physical Review Letters* **1987,** 59, (15), 1671-1674.

18. Yiotis, A. G.; Stubos, A. K.; Boudouvis, A. G.; Tsimpanogiannis, I. N.; Yortsos, Y. C., Pore-network modeling of isothermal drying in porous media. *Transport in Porous Media* **2005,** 58, (1-2), 63-86.

19. Laurindo, J. B.; Prat, M., Numerical and experimental network study of evaporation in capillary porous media. Drying rates. *Chemical Engineering Science* **1998,** 53, (12), 2257-+.

20. Lee, H. S.; Carr, W. W.; Beckham, H. W.; Leisen, J., A model of through-air drying of tufted textile materials. *International Journal of Heat and Mass Transfer* **2002,** 45, (2), 357-366.

21. Dullien, F. A. L.; Batra, V. K., Determination of the Structure of Porous Media. *Industrial & Engineering Chemistry* **1970,** 62, (10), 25-53.

22. Dehghanpour, H.; Aminzadeh, B.; Mirzaei, M.; DiCarlo, D. A., Flow coupling during three-phase gravity drainage. *Physical Review E* **2011,** 83, (6).

23. Whitaker, S., Diffusion and dispersion in porous media. *AIChE Journal* **1967,** 13, (3), 420-427.

24. Everett, D., Definitions, Terminology, and Symbols in Colloid and Surface Chemistry. *Pure and Applied Chemistry* **1972,** 31, (4), 579-638.

25. Gonzalez-Borja, M. A.; Resasco, D. E., Anisole and Guaiacol Hydrodeoxygenation over Monolithic Pt-Sn Catalysts. *Energy & Fuels* **2011,** 25, (9), 4155-4162.

26. Zhang, J.; You, C., Water Holding Capacity and Absorption Properties of Wood Chars. *Energy & Fuels* **2013,** 27, (5), 2643-2648.

27. Dehghanpour, H.; Lan, Q.; Saeed, Y.; Fei, H.; Qi, Z., Spontaneous Imbibition of Brine and Oil in Gas Shales: Effect of Water Adsorption and Resulting Microfractures. *Energy & Fuels* **2013,** 27, (6), 3039-3049.

28. Li, K.; Horne, R. N., Modeling of oil production by gravity drainage. *Journal of Petroleum Science and Engineering* **2008,** 60, (3-4), 161-169.

29. Matthews, G. P.; Ridgway, C. J.; Spearing, M. C., Void Space Modeling of Mercury Intrusion Hysteresis in Sandstone, Paper Coating, and Other Porous Media. *Journal of Colloid and Interface Science* **1995,** 171, (1), 8-27.

30. Sahimi, M., *Flow and transport in porous media and fractured rock*. Wiley. com: 2012.

31. Dąbrowski, A., Adsorption — from theory to practice. *Advances in Colloid and Interface Science* **2001,** 93, (1–3), 135-224.

32. Radlinski, A. P., Small-angle neutron scattering and the microstructure of rocks. *Neutron Scattering in Earth Sciences* **2006,** 63, 363-397.

33. Sahimi, M., Flow phenomena in rocks: from continuum models to fractals, percolation, cellular automata, and simulated annealing. *Reviews of Modern Physics* **1993,** 65, (4), 1393-1534.

34. Strange, J. H.; Rahman, M.; Smith, E. G., Characterization of porous solids by NMR. *Physical Review Letters* **1993,** 71, (21), 3589-3591.

35. Liaw, H.-K.; Kulkarni, R.; Chen, S.; Watson, A. T., Characterization of fluid distributions in porous media by NMR techniques. *AIChE Journal* **1996,** 42, (2), 538-546.

36. Evren Özarslan and Noam Shemesh and Cheng Guan Koay and Yoram Cohen and Peter, J. B., Nuclear magnetic resonance characterization of general compartment size distributions. *New Journal of Physics* **2011,** 13, (1), 015010.

37. Westphal, H.; Surholt, I.; Kiesl, C.; Thern, H. F.; Kruspe, T., NMR Measurements in Carbonate Rocks: Problems and an Approach to a Solution. *pure and applied geophysics* **2005,** 162, (3), 549-570.

38. Vizika, O.; Rosenberg, E.; Kalaydjian, F., Study of wettability and spreading impact in three-phase gas injection by cryo-scanning electron microscopy. *Journal of Petroleum Science and Engineering* **1998,** 20, (3-4), 189-202.

39. Li, H.; Yang, D.; Li, X., Determination of Three-Phase Boundaries of Solvent(s)–CO2–Heavy Oil Systems under Reservoir Conditions. *Energy & Fuels* **2012,** 27, (1), 145-153.

40. Drummond, C.; Israelachvili, J., Surface forces and wettability. *Journal of Petroleum Science and Engineering* **2002,** 33, (1-3), 123-133.

41. Israelachvili, J. N., *Intermolecular And Surface Forces*. Academic Press: 2010.

42. Drummond, C.; Israelachvili, J., Fundamental studies of crude oil-surface water interactions and its relationship to reservoir wettability. *Journal of Petroleum Science and Engineering* **2004,** 45, (1-2), 61-81.

43. Dutschk, V., Surface Wetting: From a Phenomenon to an Important Analytical Tool. In *Without Bounds: A Scientific Canvas of Nonlinearity and Complex Dynamics*, Springer: 2013; pp 227-257.

44. Jerauld, G. R.; Rathmell, J. J., Wettability and relative permeability of Prudhoe Bay: A case study in mixed-wet reservoirs. *Spe Reservoir Engineering* **1997,** 12, (1), 58-65.

45. Gao, B.; Sharma, M. M., A family of alkyl sulfate gemini surfactants. 1. Characterization of surface properties. *Journal of Colloid and Interface Science* **2013,** 404, 80-84.

46. Varka, E.-M.; Ampatzidis, C.; Kostoglou, M.; Karapantsios, T.; Dutschk, V., On the use of electrical conductance measurements for the stability of oil-in-water Pickering emulsions. *Colloids and Surfaces A: Physicochemical and Engineering Aspects* **2010,** 365, (1), 181-188.

47. Yang, S. Y.; Hirasaki, G. J.; Basu, S.; Vaidya, R., Statistical analysis on parameters that affect wetting for the crude oil/brine/mica system. *Journal of Petroleum Science and Engineering* **2002,** 33, (1-3), 203-215.

48. Cahn, J. W., Critical point wetting. *The Journal of Chemical Physics* **1977,** 66, 3667.

49. Lee, K. S.; Ivanova, N.; Starov, V. M.; Hilal, N.; Dutschk, V., Kinetics of wetting and spreading by aqueous surfactant solutions. *Advances in Colloid and Interface Science* **2008,** 144, (1-2), 54-65.

50. Silenia Garcia-Cuello, V.; Giraldo, L.; Moreno-Pirajan, J. C., Textural Characterization and Energetics of Porous Solids by Adsorption Calorimetry. *Energies* **2011,** 4, (6), 928-947.

51. Nielsen, K. Evaluation of Surfactant Flooding for EOR on the Norne Field, C-segment. Norwegian University of Science and Technology, Institutt for petroleumsteknologi og anvendt geofysikk, 2012.

52. Grigoriev, D.; Krägel, J.; Dutschk, V.; Miller, R.; Möhwald, H., Contact angle determination of micro-and nanoparticles at fluid/fluid interfaces: the excluded area concept. *Physical Chemistry Chemical Physics* **2007,** 9, (48), 6447-6454.

53. Franco, C. A.; Nassar, N. N.; Ruiz, M. A.; Pereira-Almao, P.; Cortés, F. B., Nanoparticles for Inhibition of Asphaltenes Damage: Adsorption Study and Displacement Test on Porous Media. *Energy & Fuels* **2013,** 27, (6), 2899-2907.

54. Bruus, H., *Theoretical microfluidics*. Oxford University Press: 2008; Vol. 18.

55. Xie, X.; Morrow, N. R.; Buckley, J. S., Contact angle hysteresis and the stability of wetting changes induced by adsorption from crude oil. *Journal of Petroleum Science and Engineering* **2002,** 33, (1-3), 147-159.

56. Mirzaei-Paiaman, A.; Masihi, M.; Standnes, D. C., Study on Non-equilibrium Effects during Spontaneous Imbibition. *Energy & Fuels* **2011,** 25, (7), 3053-3059.

57. Mirzaei, M.; Das, D. B., Experimental investigation of hysteretic dynamic effect in capillary pressure–saturation relationship for two-phase flow in porous media. *AIChE Journal* **2013**, n/a-n/a.

58. Snoeijer, J. H.; Andreotti, B., Moving Contact Lines: Scales, Regimes, and Dynamical Transitions. *Annual Review of Fluid Mechanics, Vol 45* **2013,** 45, 269-292.

59. Grattoni, C. A.; Jing, X. D.; Dawe, R. A., Dimensionless groups for three-phase gravity drainage flow in porous media. *Journal of Petroleum Science and Engineering* **2001,** 29, (1), 53-65.

60. Lenormand, R., Flow Through Porous Media: Limits of Fractal Patterns. *Proceedings of the Royal Society of London. A. Mathematical and Physical Sciences* **1989,** 423, (1864), 159-168.

61. Paterson, L., Diffusion-Limited Aggregation and Two-Fluid Displacements in Porous Media. *Physical Review Letters* **1984,** 52, (18), 1621-1624.

62. Larson, R. G.; Scriven, L. E.; Davis, H. T., Percolation theory of residual phases in porous media. **1977**.

63. Larson, R. G.; Scriven, L. E.; Davis, H. T., Percolation theory of two phase flow in porous media. *Chemical Engineering Science* **1981,** 36, (1), 57-73.

64. Chandler, R.; Lerman, K.; Koplik, J.; Willemsen, J. F., Capillary displacement and percolation in porous media. *Journal of Fluid Mechanics* **1982,** 119, 249-67.

65. Broadbent, S. R.; Hammersley, J. M. In *Percolation processes I. Crystals and mazes*, 1957, pp 629-41.

66. De Gennes, Dynamic capillary pressure in porous media. *Europhysics Letters* **1988,** 5, (8), 689-691.

67. Chari, V. D.; Raju, B.; Prasad, P. S.; Rao, D. N., Methane Hydrates in Spherical Silica Matrix: Optimization of Capillary Water. *Energy & Fuels* **2013,** 27, (7), 3679-3684.

68. Melrose, J. C., THERMODYNAMIC ASPECTS OF CAPILLARITY. *Industrial & Engineering Chemistry* **1968,** 60, (3), 53-70.

69. Bradford, S. A.; Leij, F. J., Wettability Effects on Scaling 2-Fluid and 3-Fluid Capillary Pressure-Saturation Relations. *Environmental Science & Technology* **1995,** 29, (6), 1446-1455.

70. Pasandideh-Fard, M.; Chen, P.; Mostaghimi, J.; Neumann, A., The generalized Laplace equation of capillarity I. Thermodynamic and hydrostatic considerations of the fundamental equation for interfaces. *Advances in colloid and interface science* **1996,** 63, 151-177.

71. Miller, E.; Miller, R., Physical theory for capillary flow phenomena. *Journal of Applied Physics* **1956,** 27, (4), 324-332.

72. Or, D., Scaling of capillary, gravity and viscous forces affecting flow morphology in unsaturated porous media. *Advances in Water Resources* **2008,** 31, (9), 1129-1136.

73. Liu, T.; Choi, K. F.; Li, Y., Capillary rise between cylinders. *Journal of Physics D-Applied Physics* **2007,** 40, (16), 5006-5012.

74. Siebold, A.; Nardin, M.; Schultz, J.; Walliser, A.; Oppliger, M., Effect of dynamic contact angle on capillary rise phenomena. *Colloids and Surfaces a-Physicochemical and Engineering Aspects* **2000,** 161, (1), 81-87.

75. Lunati, I.; Or, D., Gravity-driven slug motion in capillary tubes. *Physics of Fluids* **2009,** 21, (5).

76. Ma, Y. D., Motion effect on the dynamic contact angles in a capillary tube. *Microfluidics and Nanofluidics* **2012,** 12, (1-4), 671-675.

77. Zhou, W.; Lu, Y.; Gao, C.; Li, W.; Zhang, Y.; Li, X.; Chen, C.; Dong, J., Effects of Flow Pattern and Pore Size on Immiscible Continuous Three-Phase Displacement. *Energy & Fuels* **2013,** 27, (2), 717-724.

78. Schwartz, A. M., Capillarity - Theory and Practice. *Industrial & Engineering Chemistry* **1969,** 61, (1), 10-21.

79. Chen, C.; Zhuang, L.; Li, X.; Dong, J.; Lu, J., A Many-Body Dissipative Particle Dynamics Study of Forced Water-Oil Displacement in Capillary. *Langmuir* **2012,** 28, (2), 1330-1336.

80. Chen, C.; Gao, C.; Zhuang, L.; Li, X.; Wu, P.; Dong, J.; Lu, J., A Many-Body Dissipative Particle Dynamics Study of Spontaneous Capillary Imbibition and Drainage. *Langmuir* **2010,** 26, (12), 9533-9538.

81. Taitel, Y.; Dukler, A., A model for predicting flow regime transitions in horizontal and near horizontal gas‐liquid flow. *AIChE Journal* **1976,** 22, (1), 47-55.

82. Zhmud, B. V.; Tiberg, F.; Hallstensson, K., Dynamics of Capillary Rise. *Journal of Colloid and Interface Science* **2000,** 228, (2), 263-269.

83. Washburn, E. W., The Dynamics of Capillary Flow. *Physical Review* **1921,** 17, (3), 273-283.

84. Wongwises, S.; Pipathattakul, M., Flow pattern, pressure drop and void fraction of two-phase gas–liquid flow in an inclined narrow annular channel. *Experimental Thermal and Fluid Science* **2006,** 30, (4), 345-354.

85. Yang, C.-Y.; Shieh, C.-C., Flow pattern of air–water and two-phase R-134a in small circular tubes. *International Journal of Multiphase Flow* **2001,** 27, (7), 1163-1177.

86. Triplett, K. A.; Ghiaasiaan, S. M.; Abdel-Khalik, S. I.; Sadowski, D. L., Gas–liquid two-phase flow in microchannels Part I: two-phase flow patterns. *International Journal of Multiphase Flow* **1999,** 25, (3), 377-394.

87. Lorber, N.; Sarrazin, F.; Guillot, P.; Panizza, P.; Colin, A.; Pavageau, B.; Hany, C.; Maestro, P.; Marre, S.; Delclos, T.; Aymonier, C.; Subra, P.; Prat, L.; Gourdon, C.; Mignard, E., Some recent advances in the design and the use of miniaturized droplet-based continuous process: Applications in chemistry and high-pressure microflows. *Lab on a Chip* **2011,** 11, (5), 779-787.

88. Hoffman, R. L., A study of the advancing interface. I. Interface shape in liquid—gas systems. *Journal of Colloid and Interface Science* **1975,** 50, (2), 228-241.

89. Jiang, T.-S.; Soo-Gun, O. H.; Slattery, J. C., Correlation for dynamic contact angle. *Journal of Colloid and Interface Science* **1979,** 69, (1), 74-77.

90. Bracke, M.; Voeght, F.; Joos, P., The kinetics of wetting: the dynamic contact angle. In *Trends in Colloid and Interface Science III*, Bothorel, P.; Dufourc, E. J., Eds. Steinkopff: 1989; Vol. 79, pp 142-149.

91. Legait, B.; Sourieau, P., Effect of geometry on advancing contact angles in fine capillaries. *Journal of Colloid and Interface Science* **1985,** 107, (1), 14-20.

92. Kemp, I. C., Fundamentals of Energy Analysis of Dryers. In *Modern Drying Technology*, Wiley-VCH Verlag GmbH & Co. KGaA: 2011; pp 1-45.

93. Kao, J. Y. In *Energy test results of a conventional clothes dryer and a condenser clothes dryer*, Proceedings of the 49th International Appliance Technical Conference, Columbus, OH, 1998; Columbus, OH, 1998; pp 11-21.

94. Denkenberger, D.; Mau, S.; Calwell, C.; Wanless, E. *Residential clothes dryers: a closer look at energy efficiency test procedures and savings opportunities*; Natural Resources Defense Council: 2011.

95. Wooding, R. A.; Morel-Seytoux, H. J., Multiphase Fluid Flow Through Porous Media. *Annual Review of Fluid Mechanics* **1976,** 8, (1), 233-274.

96. Adler, P. M.; Brenner, H., Multiphase Flow in Porous Media. *Annual Review of Fluid Mechanics* **1988,** 20, (1), 35-59.

97. Jia, C.; Shing, K.; Yortsos, Y. C., Advective mass transfer from stationary sources in porous media. *Water Resources Research* **1999,** 35, (11), 3239-3251.

98. Helmig, R.; Flemisch, B.; Wolff, M.; Ebigbo, A.; Class, H., Model coupling for multiphase flow in porous media. *Advances in Water Resources* **2013,** 51, 52-66.

99. Miller, C. T.; Christakos, G.; Imhoff, P. T.; McBride, J. F.; Pedit, J. A.; Trangenstein, J. A., Multiphase flow and transport modeling in heterogeneous porous media: challenges and approaches. *Advances in Water Resources* **1998,** 21, (2), 77-120.

100. G., G. M.; J., D. L., Modeling fluid flow in oil reservoirs. *Annual Reviews of Fluid Mechanics* **2005,** 37, 28.

101. Berkowitz, B.; Cortis, A.; Dentz, M.; Scher, H., Modeling non-Fickian transport in geological formations as a continuous time random walk. *Reviews of Geophysics* **2006,** 44, (2), RG2003.

102. Silliman, S. E.; Simpson, E. S., Laboratory evidence of the scale effect in dispersion of solutes in porous media. *Water Resources Research* **1987,** 23, (8), 1667-1673.

103. Scheven, U. M.; Verganelakis, D.; Harris, R.; Johns, M. L.; Gladden, L. F., Quantitative nuclear magnetic resonance measurements of preasymptotic dispersion in flow through porous media. *Physics of Fluids* **2005,** 17, (11), 117107-7.

104. Gouze, P.; Le Borgne, T.; Leprovost, R.; Lods, G.; Poidras, T.; Pezard, P., Non-Fickian dispersion in porous media: 1. Multiscale measurements using single-well injection withdrawal tracer tests. *Water Resources Research* **2008,** 44, (6), W06426.

105. Bijeljic, B.; Raeini, A.; Mostaghimi, P.; Blunt, M. J., Predictions of non-Fickian solute transport in different classes of porous media using direct simulation on pore-scale images. *Physical Review E* **2013,** 87, (1).

106. Parmigiani, A.; Huber, C.; Bachmann, O.; Chopard, B., Pore-scale mass and reactant transport in multiphase porous media flows. *Journal of Fluid Mechanics* **2011,** 686, 40-76.

107. Dentz, M.; Le Borgne, T.; Englert, A.; Bijeljic, B., Mixing, spreading and reaction in heterogeneous media: A brief review. *Journal of Contaminant Hydrology* **2011,** 120-21, 1-17.

108. Gaus, I.; Audigane, P.; Andre, L.; Lions, J.; Jacquemet, N.; Dutst, P.; Czernichowski-Lauriol, I.; Azaroual, M., Geochemical and solute transport modelling for CO2 storage, what to expect from it? *International Journal of Greenhouse Gas Control* **2008,** 2, (4), 605-625.

109. Arbogast, T., ANALYSIS OF THE SIMULATION OF SINGLE-PHASE FLOW THROUGH A NATURALLY FRACTURED RESERVOIR. *Siam Journal on Numerical Analysis* **1989,** 26, (1), 12-29.

110. Ramirez, B.; Kazemi, H.; Al-Kobaisi, M.; Ozkan, E.; Atan, S., A Critical Review for Proper Use of Water/Oil/Gas Transfer Functions in Dual-Porosity Naturally Fractured Reservoirs: Part I. *Spe Reservoir Evaluation & Engineering* **2009,** 12, (2), 200-210.

111. Ryzhik, V., Spreading of a NAPL lens in a double-porosity medium. *Computational Geosciences* **2007,** 11, (1), 1-8.

112. Das, S.; Misra, R. P.; Thundat, T.; Chakraborty, S.; Mitra, S. K., Modeling of Asphaltene Transport and Separation in the Presence of Finite Aggregation Effects in Pressure-Driven Microchannel Flow. *Energy & Fuels* **2012,** 26, (9), 5851-5857.

113. Nunn, J. A., Buoyancy-driven propagation of isolated fluid-filled fractures: Implications for fluid transport in Gulf of Mexico geopressured sediments. *Journal of Geophysical Research: Solid Earth* **1996,** 101, (B2), 2963-2970.

114. Chareyre, B.; Cortis, A.; Catalano, E.; Barthélemy, E., Pore-Scale Modeling of Viscous Flow and Induced Forces in Dense Sphere Packings. *Transport in Porous Media* **2012,** 92, (2), 473-493.

115. Jahanbakhshi, S.; Ghazanfari, M. H.; Masihi, M., Non-equilibrium model of three-phase flow in porous media in presence of capillary and gravity forces. *Journal of Hydrology* **2013,** 478, 119-131.

116. Saffman, P. G.; Taylor, G., The Penetration of a Fluid into a Porous Medium or Hele-Shaw Cell Containing a More Viscous Liquid. *Proceedings of the Royal Society of London. Series A. Mathematical and Physical Sciences* **1958,** 245, (1242), 312-329.

117. Homsy, G. M., VISCOUS FINGERING IN POROUS-MEDIA. *Annual Review of Fluid Mechanics* **1987,** 19, 271-311.

118. Loggia, D.; Rakotomalala, N.; Salin, D.; Yortsos, Y. C., The effect of mobility gradients on viscous instabilities in miscible flows in porous media. *Physics of Fluids* **1999,** 11, (3), 740-742.

119. Butts, M. B.; Jensen, K. H., Effective parameters for multiphase flow in layered soils. *Journal of Hydrology* **1996,** 183, (1-2), 101-116.

120. Stokes, J. P.; Weitz, D. A.; Gollub, J. P.; Dougherty, A.; Robbins, M. O.; Chaikin, P. M.; Lindsay, H. M., Interfacial Stability of Immiscible Displacement in a Porous Medium. *Physical Review Letters* **1986,** 57, (14), 1718-1721.

121. Lenormand, R.; Touboul, E.; Zarcone, C., NUMERICAL-MODELS AND EXPERIMENTS ON IMMISCIBLE DISPLACEMENTS IN POROUS-MEDIA. *Journal of Fluid Mechanics* **1988,** 189, 165-187.

122. Vicsek, H. V. K. a. F. F. a. T., Dynamic scaling of the interface in two-phase viscous flows in porous media. *Journal of Physics A: Mathematical and General* **1991,** 24, (1), L25.

123. Yu, B.; Li, J., Some fractal characters of porous media. *Fractals* **2001,** 9, (03), 365-372.

124. Yu, B.; Cheng, P., A fractal permeability model for bi-dispersed porous media. *International Journal of Heat and Mass Transfer* **2002,** 45, (14), 2983-2993.

125. Barlow, M.; Perkins, E., Brownian motion on the Sierpinski gasket. *Probability Theory and Related Fields* **1988,** 79, (4), 543-623.

126. Sierpinski, M., Sur une courbe dont tout point est un point de ramification. *Compte Rendus hebdomadaires des s\\'eance de l\'Acad\\'emie des Science de Paris* **1915,** 160, 302-305.

127. Schroeder, M. R., *Fractals, chaos, power laws: Minutes from an infinite paradise*. Courier Dover Publications: 2012.

128. Foroutan-pour, K.; Dutilleul, P.; Smith, D. L., Advances in the implementation of the box-counting method of fractal dimension estimation. *Applied Mathematics and Computation* **1999,** 105, (2–3), 195-210.

129. Glass, R. J.; Steenhuis, T. S.; Parlange, J. Y., WETTING FRONT INSTABILITY .2. EXPERIMENTAL-DETERMINATION OF RELATIONSHIPS BETWEEN SYSTEM PARAMETERS AND TWO-DIMENSIONAL UNSTABLE FLOW FIELD BEHAVIOR IN INITIALLY DRY POROUS-MEDIA. *Water Resources Research* **1989,** 25, (6), 1195-1207.

130. Fukushima, E., Nuclear magnetic resonance as a tool to study flow. *Annual Review of Fluid Mechanics* **1999,** 31, (1), 95-123.

131. Barrie, P. J., Characterization of porous media using NMR methods. In *Annual Reports on NMR Spectroscopy*, Academic Press: 2000; Vol. Volume 41, pp 265-316.

132. Er, V.; Babadagli, T.; Xu, Z., Pore-Scale Investigation of the Matrix−Fracture Interaction During CO2 Injection in Naturally Fractured Oil Reservoirs. *Energy & Fuels* **2009,** 24, (2), 1421-1430.

133. Whitesides, G. M., The origins and the future of microfluidics. *Nature* **2006,** 442, (7101), 368-73.

134. Tomaiuolo, G.; Barra, M.; Preziosi, V.; Cassinese, A.; Rotoli, B.; Guido, S., Microfluidics analysis of red blood cell membrane viscoelasticity. *Lab on a Chip* **2011,** 11, (3), 449-454.

135. Primiceri, E.; Chiriaco, M. S.; Rinaldi, R.; Maruccio, G., Cell chips as new tools for cell biology - results, perspectives and opportunities. *Lab on a Chip* **2013,** 13, (19), 3789-3802.

136. Pommella, A.; Tomaiuolo, G.; Chartoire, A.; Caserta, S.; Toscano, G.; Nolan, S. P.; Guido, S., Palladium-N-heterocyclic carbene (NHC) catalyzed C–N bond formation in a continuous flow microreactor. Effect of process parameters and comparison with batch operation. *Chemical Engineering Journal* **2013,** 223, (0), 578-583.

137. Delville, M. M. E.; Nieuwland, P. J.; Janssen, P.; Koch, K.; van Hest, J. C. M.; Rutjes, F. P. J. T., Continuous flow azide formation: Optimization and scale-up. *Chemical Engineering Journal* **2011,** 167, (2–3), 556-559.

138. Fadaei, H.; Shaw, J. M.; Sinton, D., Bitumen-Toluene Mutual Diffusion Coefficients Using Microfluidics. *Energy & Fuels* **2013,** 27, (4), 2042-2048.

139. Al-Housseiny, T. T.; Tsai, P. A.; Stone, H. A., Control of interfacial instabilities using flow geometry. *Nature Physics* **2012,** 8, (10), 747-750.

140. Al-Housseiny, T. T.; Christov, I. C.; Stone, H. A., Two-phase fluid displacement and interfacial instabilities under elastic membranes. *Physical review letters* **2013,** 111, (3), 034502.

141. Setu, S. A.; Zacharoudiou, I.; Davies, G. J.; Bartolo, D.; Moulinet, S.; Louis, A. A.; Yeomans, J. M.; Aarts, D. G., Viscous fingering at ultralow interfacial tension. *arXiv preprint arXiv:1309.2770* **2013**.

142. Dias, E. O.; Miranda, J. A., Taper-induced control of viscous fingering in variable-gap Hele-Shaw flows. *Physical Review E* **2013,** 87, (5), 053015.

143. Shou, D.; Fan, J.; Mei, M.; Ding, F., An analytical model for gas diffusion though nanoscale and microscale fibrous media. *Microfluidics and Nanofluidics* **2013**, 1-9.

144. Lanotte, L.; Bilotti, C.; Sabetta, L.; Tomaiuolo, G.; Guido, S., Dispersion of sepiolite rods in nanofibers by electrospinning. *Polymer* **2013,** 54, (4), 1295-1297.

145. Hoogerbrugge, P. J.; Koelman, J., SIMULATING MICROSCOPIC HYDRODYNAMIC PHENOMENA WITH DISSIPATIVE PARTICLE DYNAMICS. *Europhysics Letters* **1992,** 19, (3), 155-160.

146. Chen, S.; Doolen, G. D., Lattice Boltzmann method for fluid flows. *Annual Review of Fluid Mechanics* **1998,** 30, 329-364.

147. Ahrenholz, B.; Toelke, J.; Krafczyk, M., Lattice-Boltzmann simulations in reconstructed parametrized porous media. *International Journal of Computational Fluid Dynamics* **2006,** 20, (6), 369-377.

148. Narvaez, A.; Yazdchi, K.; Luding, S.; Harting, J., From creeping to inertial flow in porous media: a lattice Boltzmann-finite element study. *Journal of Statistical Mechanics-Theory and Experiment* **2013**.

149. Goldstein, R. J.; Ibele, W. E.; Patankar, S. V.; Simon, T. W.; Kuehn, T. H.; Strykowski, P. J.; Tamma, K. K.; Heberlein, J. V. R.; Davidson, J. H.; Bischof, J.; Kulacki, F. A.; Kortshagen, U.; Garrick, S.; Srinivasan, V.; Ghosh, K.; Mittal, R., Heat transfer—A review of 2005 literature. *International Journal of Heat and Mass Transfer* **2010,** 53, (21–22), 4397-4447.

150. Hassanizadeh, S. M.; Gray, W. G., MECHANICS AND THERMODYNAMICS OF MULTIPHASE FLOW IN POROUS-MEDIA INCLUDING INTERPHASE BOUNDARIES. *Advances in Water Resources* **1990,** 13, (4), 169-186.

151. Haghi, A. K., Transport phenomena in porous media: A review. *Theoretical Foundations of Chemical Engineering* **2006,** 40, (1), 14-26.

152. Amiri, A.; Vafai, K., Analysis of dispersion effects and non-thermal equilibrium, non-Darcian, variable porosity incompressible flow through porous media. *International Journal of Heat and Mass Transfer* **1994,** 37, (6), 939-954.

153. Vafai, K.; Tien, C. L., Boundary and inertia effects on flow and heat transfer in porous media. *International Journal of Heat and Mass Transfer* **1981,** 24, (2), 195-203.

154. Houshmand, F.; Peles, Y., Convective heat transfer to shear-driven liquid film flow in a microchannel. *International Journal of Heat and Mass Transfer* **2013,** 64, 42-52.

155. Amanifard, N.; Borji, M.; Haghi, A. K., Heat transfer in porous media. *Brazilian Journal of Chemical Engineering* **2007,** 24, (2), 223-232.

156. Hsieh, Y. L., LIQUID TRANSPORT IN FABRIC STRUCTURES. *Textile Research Journal* **1995,** 65, (5), 299-307.

157. Zhu, F.; Li, K., Numerical Modeling of Heat and Moisture Through Wet Cotton Fabric Using the Method of Chemical Thermodynamic Law Under Simulated Fire. *Fire Technology* **2011,** 47, (3), 801-819.

158. Kowalski, S.; Musielak, G.; Banaszak, J., Experimental validation of the heat and mass transfer model for convective drying. *Drying technology* **2007,** 25, (1), 107-121.

159. Kowalski, S. J.; Smoczkiewicz-Wojciechowska, A., Stresses in dried wood. Modelling and experimental identification. *Transport in porous media* **2007,** 66, (1-2), 145-158.

160. Luo, X. N.; Xu, Q. Z., A new numerical implementation on 2D heat and moisture transfer through fabric. *Applied Mathematics and Computation* **2006,** 174, (2), 1135-1150.

161. Kowalski, S. J.; Rybicki, A., The vapour-liquid interface and stresses in dried bodies. In *Drying of Porous Materials*, Springer: 2007; pp 43-58.

162. Lu, T.; Shen, S., Numerical and experimental investigation of paper drying: Heat and mass transfer with phase change in porous media. *Applied Thermal Engineering* **2007,** 27, (8), 1248-1258.

163. De Bonis, M.; Ruocco, G., Modelling local heat and mass transfer in food slabs due to air jet impingement. *Journal of Food Engineering* **2007,** 78, (1), 230-237.

164. Kakaç, S.; Yener, Y., *Convective Heat Transfer, Second Edition*. Taylor & Francis: 1994.

165. Cengel, Y. A., *Heat and Mass Transfer: A Practical Approach W/ Ees CD*. McGraw-Hill Science/Engineering/Math: 2006.

166. Kowalski, S. J., *Thermomechanics of drying processes*. Springer: 2003; Vol. 8.

167. Kondepudi, D., *Introduction to modern thermodynamics*. Wiley. com: 2008.

168. Welty, J. R.; Wicks, C. E.; Rorrer, G.; Wilson, R. E., *Fundamentals of momentum, heat, and mass transfer*. John Wiley & Sons: 2009.

169. Incropera, F. P.; Lavine, A. S.; DeWitt, D. P., *Fundamentals of heat and mass transfer*. John Wiley & Sons Incorporated: 2011.

170. Telljohann, U.; Junge, K.; Specht, E., Moisture diffusion coefficients for modeling the first and second drying sections of green bricks. *Drying Technology* **2008,** 26, (7), 855-863.

171. Reyes, A.; Eckholt, M.; Troncoso, F.; Efremov, G., Drying kinetics of sludge from a wastewater treatment plant. *Drying technology* **2004,** 22, (9), 2135-2150.

172. Moropoulou, A.; Karoglou, M.; Giakoumaki, A.; Krokida, M.; Maroulis, Z.; Saravacos, G., Drying kinetics of some building materials. *Brazilian Journal of Chemical Engineering* **2005,** 22, (2), 203-208.

173. Whitaker, S., *Toward a Diffusion Theory of Drying*. 1977; Vol. 4, p 408-414.

174. Prat, M., Recent advances in pore-scale models for drying of porous media. *Chemical Engineering Journal* **2002,** 86, (1-2), 153-164.

175. Prat, M., Discrete models of liquid-vapour phase change phenomena in porous media. *Revue Generale De Thermique* **1998,** 37, (11), 954-961.

176. Camassel, B.; Sghaier, N.; Prat, M.; Ben Nasrallah, S., Evaporation in a capillary tube of square cross-section: application to ion transport. *Chemical engineering science* **2005,** 60, (3), 815-826.

177. Debaste, F.; Dubois, F.; Halloin, V., *CHISA 2006 - 17th International Congress of Chemical and Process Engineering* **2006**.

178. Oron, A.; Davis, S. H.; Bankoff, S. G., Long-scale evolution of thin liquid films. *Reviews of modern physics* **1997,** 69, (3), 931.

179. Carey, V., Heat and fluid flow in microscale and nanoscale structures, volume 13 of Development in heat transfer, chapter DSMC modeling of near-interface transport in liquid-vapor phase-change processes with multiple microscale effects. In WIT Press: 2002.

180. Probstein, R. F., *Physicochemical hydrodynamics: an introduction*. Wiley. com: 2005.

181. Matsumoto, H.; Colgate, J. E. In *Preliminary investigation of micropumping based on electrical control of interfacial tension*, Micro Electro Mechanical Systems, 1990. Proceedings, An Investigation of Micro Structures, Sensors, Actuators, Machines and Robots. IEEE, 1990; IEEE: 1990; pp 105-110.

182. Lautrup, B., *Physics of Continuous Matter: Exotic and Everyday Phenomena in the Macroscopic World*. Taylor & Francis US: 2011.

183. Jensen, M. J., Bubbles in microchannels. *Master project, MIC–Technical University of Denmark* **2002**.

184. Gowdy, J. M.; McDaniel, C. N., One world, one experiment: addressing the biodiversity—economics conflict. *Ecological Economics* **1995,** 15, (3), 181-192.

185. Guida, V., Thermodynamics and kinetics of vesicles formation processes. *Advances in colloid and interface science* **2010,** 161, (1), 77-88.

186. Kaler, E. W.; Murthy, A. K.; Rodriguez, B. E.; Zasadzinski, J., Spontaneous vesicle formation in aqueous mixtures of single-tailed surfactants. *Science* **1989,** 245, (4924), 1371-1374.

187. Singer, S. J.; Nicolson, G. L., The fluid mosaic model of the structure of cell membranes. *Science* **1972,** 175, (23), 720-731.

188. Kessler, S.; Finken, R.; Seifert, U., Swinging and tumbling of elastic capsules in shear flow. *Journal of Fluid Mechanics* **2008,** 605, 207-226.

189. Vitkova, V.; Mader, M.; Podgorski, T., Deformation of vesicles flowing through capillaries. *EPL (Europhysics Letters)* **2004,** 68, (3), 398.

190. Coupier, G.; Farutin, A.; Minetti, C.; Podgorski, T.; Misbah, C., Shape diagram of vesicles in Poiseuille flow. *Physical Review Letters* **2012,** 108, (17), 178106.

191. Discher, D. E.; Eisenberg, A., Polymer vesicles. *Science* **2002,** 297, (5583), 967-973.

192. Noguchi, H.; Gompper, G., Shape transitions of fluid vesicles and red blood cells in capillary flows. *Proceedings of the National Academy of Sciences of the United States of America* **2005,** 102, (40), 14159-14164.

193. McWhirter, J. L.; Noguchi, H.; Gompper, G., Flow-induced clustering and alignment of vesicles and red blood cells in microcapillaries. *Proceedings of the National Academy of Sciences* **2009,** 106, (15), 6039-6043.

194. Vlahovska, P. M.; Loewenberg, M.; Blawzdziewicz, J., Deformation of a surfactant-covered drop in a linear flow. *Physics of Fluids* **2005,** 17, 103103.

195. Tomaiuolo, G.; Guido, S., Start-up shape dynamics of red blood cells in microcapillary flow. *Microvascular Research* **2011,** 82, (1), 35-41.

196. Lanotte, L.; Tomaiuolo, G.; Misbah, C.; Bureau, L.; Guido, S., Red blood cell dynamics in polymer brush-coated microcapillaries: A model of endothelial glycocalyx in vitro. *Biomicrofluidics* **2014,** 8, (1), 014104.

197. Guido, S.; Preziosi, V., Droplet deformation under confined Poiseuille flow. *Advances in Colloid and Interface Science* **2010,** 161, (1-2), 89-101.

198. Tomaiuolo, G.; Rossi, D.; Caserta, S.; Cesarelli, M.; Guido, S., Comparison of two flow ‐ based imaging methods to measure individual red blood cell area and volume. *Cytometry Part A* **2012,** 81, (12), 1040-1047.

199. Abreu, D.; Levant, M.; Steinberg, V.; Seifert, U., Fluid Vesicles in Flow. *arXiv preprint arXiv:1311.7341* **2013**.

200. Lan, H.; Khismatullin, D. B., A numerical study of the lateral migration and deformation of drops and leukocytes in a rectangular microchannel. *International Journal of Multiphase Flow* **2012**.

201. Tomaiuolo, G.; Lanotte, L.; Ghigliotti, G.; Misbah, C.; Guido, S., Red blood cell clustering in Poiseuille microcapillary flow. *Physics of Fluids (1994-present)* **2012,** 24, (5), 051903.

202. Vlahovska, P. M.; Barthes-Biesel, D.; Misbah, C., Flow dynamics of red blood cells and their biomimetic counterparts. *Comptes Rendus Physique* **2013,** 14, (6), 451-458.

203. Ghigliotti, G.; Selmi, H.; El Asmi, L.; Misbah, C., Why and how does collective red blood cells motion occur in the blood microcirculation? *Physics of Fluids (1994-present)* **2012,** 24, (10), 101901.

204. Pommella, A.; Caserta, S.; Guida, V.; Guido, S., Shear-induced deformation of surfactant multilamellar vesicles. *Physical review letters* **2012,** 108, (13), 138301.

205. Pommella, A.; Caserta, S.; Guido, S., Dynamic flow behaviour of surfactant vesicles under shear flow. Role of multilamellar microstructure. *Soft Matter* **2013**.

206. Guedda, M., Membrane compression in tumbling and vacillating-breathing regimes for quasispherical vesicles. *Physical Review E* **2014,** 89, (1), 012703.

207. Misbah, C., Vacillating breathing and tumbling of vesicles under shear flow. *Physical review letters* **2006,** 96, (2), 028104.

208. Caserta, S.; Reynaud, S.; Simeone, M.; Guido, S., Drop deformation in sheared polymer blends. *Journal of Rheology (1978-present)* **2007,** 51, (4), 761-774.

209. Aranberri, I.; Binks, B.; Clint, J.; Fletcher, P., Evaporation rates of water from concentrated oil-in-water emulsions. *Langmuir* **2004,** 20, (6), 2069-2074.

210. Alexandridis, P.; Munshi, S. Z.; Gu, Z., Evaporation of water from structured surfactant solutions. *Industrial & Engineering Chemistry Research* **2010,** 50, (2), 580-589.

211. Doganci, M. D.; Sesli, B. U.; Erbil, H. Y., Diffusion-controlled evaporation of sodium dodecyl sulfate solution drops placed on a hydrophobic substrate. *Journal of colloid and interface science* **2011,** 362, (2), 524-531.

212. Rodríguez, J. L.; Minardi, R. M.; Ciolino, A.; Pieroni, O.; Vuano, B.; Schulz, E. P.; Schulz, P. C., Effect of an amphiphilic polymer on the evaporation behavior of its solutions in toluene and in water. *Colloids and Surfaces A: Physicochemical and Engineering Aspects* **2009,** 352, (1), 74-78.

213. Richards, C.; Tiddy, G. J.; Casey, S., Liquid crystal and solution phases of sodium dodecyl-p-benzene sulphonate (NaLAS) and octa-oxyethylene glycol hexadecyl ether (C16E8): 1: 1 mixtures in water. *Colloid and Polymer Science* **2008,** 286, (1), 31-46.

214. Richards, C.; Tiddy, G. J.; Casey, S., Lateral Phase Separation Gives Multiple Lamellar Phases in a "Binary" Surfactant/Water System: The Phase Behavior of Sodium Alkyl Benzene Sulfonate/Water Mixtures. *Langmuir* **2007,** 23, (2), 467-474.

215. Ip, R. W. L.; Wan, E. I. C., The New Use of Diffusion Theories for the Design of Heat Setting Process in Fabric Drying. **2012**.

216. Yiotis, A.; Stubos, A.; Boudouvis, A.; Tsimpanogiannis, I.; Yortsos, Y., Pore-Network Modeling of Isothermal Drying in Porous Media. *Transport in Porous Media* **2005,** 58, (1-2), 63-86.

217. Laurindo, J. B.; Prat, M., Modeling of drying in capillary-porous media: A discrete approach. *Drying Technology* **1998,** 16, (9-10), 1769-1787.

218. Metzger, T.; Tsotsas, E., Network models for capillary porous media: application to drying technology. *Chemie Ingenieur Technik* **2010,** 82, (6), 869-879.

219. Adu, B.; Otten, L.; Afenya, E.; Groenevelt, P., Thermodynamics of microwave (polarized) heating systems. *Journal of microwave power and electromagnetic energy* **1995,** 30, 90-90.

220. Russel, M.; Yao, J.; Chen, H.; Wang, F.; Zhou, Y.; Choi, M. M.; Zaray, G.; Trebse, P., Different technique of microcalorimetry and their applications to environmental sciences: A review. *J. Amer. Sci* **2009,** 5, 194-208.

221. Wilson, T., *Confocal microscopy*. Academic Press London: 1990; Vol. 991.

222. Pawley, J., *Handbook of biological confocal microscopy*. Springer: 2010.

223. Kino, G. S.; Corle, T. R., *Confocal scanning optical microscopy and related imaging systems*. Academic Press: 1996.

224. Webb, R. H., Confocal optical microscopy. *Reports on Progress in Physics* **1996,** 59, (3), 427.

225. Hermansson, K.; Lindberg, U.; Hok, B.; Palmskog, G. In *Wetting properties of silicon surfaces*, Solid-State Sensors and Actuators, 1991. Digest of Technical Papers, TRANSDUCERS'91., 1991 International Conference on, 1991; IEEE: 1991; pp 193-196.

226. Fainerman, V. B.; Lylyk, S. V.; Aksenenko, E. V.; Kovalchuk, N. M.; Kovalchuk, V. I.; Petkov, J. T.; Miller, R., Effect of water hardness on surface tension and dilational visco-elasticity of sodium dodecyl sulphate solutions. *Journal of Colloid and Interface Science* **2012,** 377, (1), 1-6.

227. Hasan, M.; Calvimontes, A.; Synytska, A.; Dutschk, V., Effects of topographic structure on wettability of differently woven fabrics. *Textile research journal* **2008,** 78, (11), 996-1003.

228. Potluri, P.; Parlak, I.; Ramgulam, R.; Sagar, T. V., Analysis of tow deformations in textile preforms subjected to forming forces. *Composites Science and Technology* **2006,** 66, (2), 297-305.

229. Kumpikaite, E.; Olšauskiene, A., Influence of fabric structure on some technological and end-use properties. *Fibres & Textiles in Eastern Europe* **2003,** 11, (2), 41.

230. Kumpikaite, E., Analysis of dependencies of woven fabric's breaking force and elongation at break on its structure parameters. *FIBRES & TEXTILES IN EASTERN EUROPE* **2007,** 15, (1), 35-38.

231. Meredith, R., Measurements of orientation in cotton fibres using polarized light. *British Journal of Applied Physics* **1953,** 4, (12), 369.

232. Potikha, T. S.; Collins, C. C.; Johnson, D. I.; Delmer, D. P.; Levine, A., The involvement of hydrogen peroxide in the differentiation of secondary walls in cotton fibers. *Plant Physiology* **1999,** 119, (3), 849-858.

233. Jackson, G. W.; James, D. F., The permeability of fibrous porous media. *The Canadian Journal of Chemical Engineering* **1986,** 64, (3), 364-374.

234. Wakelyn, P. J.; Bertoniere, N. R.; French, A. D.; Thibodeaux, D. P.; Triplett, B. A.; Rousselle, M.-A.; Goynes Jr, W. R.; Edwards, J. V.; Hunter, L.; McAlister, D. D., *Cotton fiber chemistry and technology*. CRC Press: 2010.

235. Anderson, D. B.; Kerr, T., Growth and strcture of cotton fiber. *Industrial and Engineering Chemistry* **1938,** 30, (1), 48-54.

236. Das, B.; Das, A.; Kothari, V.; Fanguiero, R.; Araujo, M. D., Moisture Flow through Blended Fabrics - Effect of Hydrophilicity. *Journal of Engineered Fibers and Fabrics* **2009,** 4, (4), 20-28.

237. McGovern, J., Fibers, vegetable. In *Polymers: fibers and textiles: a compendium*, Wiley-Interscience: 1990; pp 412-430.

238. John, M. E.; Keller, G., Metabolic pathway engineering in cotton: biosynthesis of polyhydroxybutyrate in fiber cells. *Proceedings of the National Academy of Sciences* **1996,** 93, (23), 12768-12773.

239. Carvalho, V.; Vasconcelos, R. M.; Soares, F. O.; Belsley, M., Yarn Diameter and Linear Mass Correlation. *Journal of Nondestructive Evaluation* **2009,** 28, (2), 49-54.

240. Rollins, M. L.; Tripp, V. W., Optical and electron microscopic studies of cotton fiber structure. *Textile Research Journal* **1954,** 24, (4), 345-357.

241. Zhang, Y. X.; Xu, Z. J., ATOMIC RADII OF NOBLE-GAS ELEMENTS IN CONDENSED PHASES. *American Mineralogist* **1995,** 80, (7-8), 670-675.

242. Franks, F.; Chemistry, R. S. o., *Water: A Matrix of Life*. Royal Society of Chemistry: 2000.

243. Mark, H. F., *Encyclopedia of Polymer Science and Technology, Concise*. Wiley: 2013.

244. Mondal, S.; Hu, J. L., Water vapor permeability of cotton fabrics coated with shape memory polyurethane. *Carbohydrate Polymers* **2007,** 67, (3), 282-287.

245. Orgânico, A., 4.2. 2.1 FIBRAS NATURAIS DE ORIGEM VE-GETAL. *NOVAS BASES TÊXTEIS PARA NOVAS EXIGÊNCIAS SOCIAIS* **2011**, 38.

246. LIU, H.; GOH, W.-P.; NORSTEN, T. B., AQUEOUS-BASED FORMATION OF GOLD NANOPARTICLES ON SURFACE-MODIFIED COTTON TEXTILES. *Journal of Molecular and Engineering Materials* **2013,** 1, (01).

247. Lefèvre, C. *Ecodesign of Laundry Dryers,Preparatory studies for Ecodesign requirementsof Energy-using-Products (EuP) – Lot 16*; Ecobilan, PricewaterhouseCoopers: 2009.

248. Mangat, M. M. A., Structure and properties of cotton fiber: A literature review **2009**.

249. Ogiwara, Y.; Kubota, H.; Hayashi, S.; Mitomo, N., Temperature dependency of bound water of cellulose studied by a high‐resolution NMR spectrometer. *Journal of Applied Polymer Science* **1970,** 14, (2), 303-309.

250. Caurie, M., Bound water: its definition, estimation and characteristics. *International Journal of Food Science and Technology* **2011,** 46, (5), 930-934.

251. Caurie, M., The unimolecular character of the classical Brunauer, Emmett and Teller adsorption equation and moisture adsorption. *International Journal of Food Science and Technology* **2005,** 40, (3), 283-293.

252. Princi, E.; Vicini, S.; Pedemonte, E.; Arrighi, V.; McEwen, I., Thermal characterisation of cellulose based materials. *Journal of thermal analysis and calorimetry* **2005,** 80, (2), 369-373.

253. Ibbett, R. N.; Hsieh, Y. L., Effect of fiber swelling on the structure of lyocell fabrics. *Textile Research Journal* **2001,** 71, (2), 164-173.

254. Schott, H., Adsorption of a nonionic surfactant by cotton. *Journal of Colloid and Interface Science* **1967,** 23, (1), 46-51.

255. Patterson, J.; Morris, E., Measurement of absolute water density, 1 C to 40 C. *Metrologia* **1994,** 31, (4), 277.

256. Steinhaus, H., *Mathematical snapshots*. Courier Dover Publications: 1999.

257. Chamarthy, P.; Dhavaleswarapu, H.; Garimella, S. V.; Murthy, J. Y.; Wereley, S., Visualization of Convection Patterns Near an Evaporating Meniscus using micro-PIV. In Purdue University: 2008.

258. Panchamgam, S. S.; Chatterjee, A.; Plawsky, J. L.; Wayner, P. C., Jr., Comprehensive experimental and theoretical study of fluid flow and heat transfer in a microscopic evaporating meniscus in a miniature heat exchanger. *International Journal of Heat and Mass Transfer* **2008,** 51, (21-22), 5368-5379.

259. Panchamgam, S. S.; Plawsky, J. L.; Wayner, P. C., Jr., Microscale heat transfer in an evaporating moving extended meniscus. *Experimental Thermal and Fluid Science* **2006,** 30, (8), 745-754.

8 APPENDIX

"Be content with what you have, rejoice in the way things are.
When you realize there is nothing lacking, the whole world belongs to you."
Lao Tsu

8.1 Conferences

- D. Donnarumma, G. Tomaiuolo, S. Caserta, S. Guido, *"Essiccamento in mezzi porosi"*, Convegno GRICU 2012, September 16-19, 2012, Montesilvano (Italy).
- D. Donnarumma, S. Caserta, G. Tomaiuolo, S. Guido, "*Drying in porous media*" COST MP1106 WORKSHOP 21-22 March 2013, Prague (Czech Republic).
- D. Donnarumma, G. Tomaiuolo, S. Caserta, S. Guido, "*Gas-liquid multiphase flow through porous media*" 14th international conference on petroleum phase behavior and fouling 10-13 June 2013, Rueil Malmaison (France).
- D. Donnarumma, G. Tomaiuolo, S. Caserta, S. Guido, "*Multiphase flow through porous media*" DICMAPI WORKSHOP 9 July 2013, Naples (Italy).
- D. Donnarumma, G. Tomaiuolo, S. Caserta, A. Perazzo, S. Guido, "*Flow through porous media at the gas-liquid interface*" 27th ECIS Conference 1-6 September 2013 Sofia (Bulgary).
- D. Donnarumma, G. Tomaiuolo, S. Caserta, S. Guido, "*Liquid flow in porous media*" COST MP1106 WORKSHOP 13-14 November 2013, Cargese (France).

8.2 Experience in other laboratories

- "TA Instruments TAM Perfusion Training", at the Thermal Laboratory, Pomezia Plant, Procter & Gamble Italia S.p.a. – P&G supervisor: Vincenzo Guida. 18-19 october 2012.
- Experimental measures at the Thermal Laboratory, Pomezia Plant, Procter & Gamble Italia – P&G supervisor: Vincenzo Guida. 4-7, 11-14, 24-28 october, 20-25 november, 5-7 december 2011
- "TA Instruments DVS Training", at the Thermal Laboratory, Pomezia Plant, Procter & Gamble Italia S.p.a. – P&G supervisor: Vincenzo Guida. 7 july 2011

8.3 Workshops and Training Schools

- "*A way to smart Europe*" COST MP1106 TRAINING SCHOOL 23-25 April 2013, University of Twente, Enschede (the Netherlands).
- "*Multifuncional textiles based on hybrid coatings and nanoparticles*" COST MP1105 WORKSHOP 17 September 2013, Naples (Italy).